

NAG-1-623

11 37  
p. 160

# **DYNAMIC CONTROL MODIFICATION TECHNIQUES IN TELEOPERATION OF A FLEXIBLE MANIPULATOR**

**A THESIS  
Presented to  
The Academic Faculty**

**by**

**David Patrick Magee**

**In Partial Fulfillment  
of the Requirements for the Degree  
Master of Science in Mechanical Engineering**

**Georgia Institute of Technology  
November 1991**

N93-12904

Unclass

G3/37 0127261

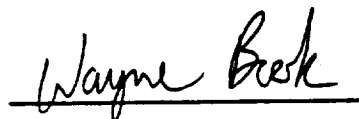
(NASA-CR-190984) DYNAMIC CONTROL  
MODIFICATION TECHNIQUES IN  
TELEOPERATION OF A FLEXIBLE  
MANIPULATOR M.S. Thesis (Georgia  
Inst. of Tech.) 160 p

— —

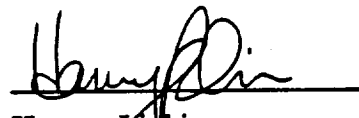
1

# **DYNAMIC CONTROL MODIFICATION TECHNIQUES IN TELEOPERATION OF A FLEXIBLE MANIPULATOR**

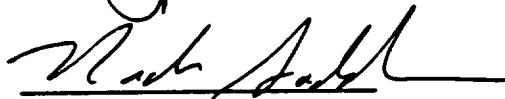
**APPROVED:**



Wayne Book, Chairman



Harvey Lipkin



Nader Sadegh

Date Approved by Chairperson 11/18/91



*Dedicated to*  
*my loving wife, Carolyn, and to my family,*  
*who provided unconditional support in this endeavor*



## **ACKNOWLEDGEMENTS**

I would like to thank Dr. Wayne Book for his friendship, his guidance and, most importantly, his patience during this project. I also would like to thank the members of my committee for their advice and suggestions that aided the preparation of this document.

The members of my research group, Jonathan Cameron, Doug Girvin, J.D. Huggins, Dr. Dong-Soo Kwon, Soo Han Lee, Jae Lew, Lonnie Love and J.J. Wang, provided friendship and useful discussions. I would like to extend special thanks to J.D. for his assistance in the photo sessions that took place late at night and to Lonnie for his many suggestions to improve this document. Finally, I must recognize Scott Coleman for his support and friendship for the last six years.





## TABLE OF CONTENTS

	Page
DEDICATION . . . . .	iii
ACKNOWLEDGEMENTS . . . . .	iv
TABLE OF CONTENTS . . . . .	v
LIST OF TABLES . . . . .	viii
LIST OF ILLUSTRATIONS . . . . .	ix
SUMMARY . . . . .	xiii
CHAPTER	
I. INTRODUCTION . . . . .	1
1.1 Motivation for this Research . . . . .	1
1.2 Previous Methods for Reducing Vibration . . . . .	2
1.3 Characteristics of a Flexible System . . . . .	5
1.4 Method of Approach . . . . .	6
II. EXPERIMENTAL TEST BED . . . . .	7
2.1 Description of the Robotic Manipulator . . . . .	7
2.2 Design of an Input Device . . . . .	12
2.3 Interfacing the Telerobotic System . . . . .	13
2.4 System Hardware . . . . .	15

III. MODIFIED COMMAND SHAPING . . . . .	17
3.1 Historical Perspective . . . . .	17
3.2 Derivation of Constraint Equations . . . . .	18
3.3 Calculation of Impulse Amplitudes . . . . .	24
3.4 Robustness of Constraint Equations . . . . .	31
3.5 Position Dependent System Parameters . . . . .	38
IV. DYNAMIC ANALYSIS OF RALF . . . . .	47
4.1 Previous Frequency Analysis . . . . .	47
4.2 Experimental Setup and Procedures . . . . .	47
4.3 Modal Analysis Results . . . . .	49
4.4 Curve Fitting of Experimental Data . . . . .	51
V. CONTROL IMPLEMENTATION AND RESULTS . . . . .	55
5.1 Control Structure . . . . .	55
5.2 Input Trajectories . . . . .	56
5.2.1 Trajectory One - Circle With No Perturbation . . . . .	58
5.2.2 Trajectory Two - Circle With 1 Hz Perturbation . . . . .	62
5.2.3 Trajectory Three - Circle With 4.8 Hz Perturbation . . . . .	63
5.2.4 Trajectory Four - Circle With 10 Hz Perturbation . . . . .	66
5.2.5 Trajectory Five - Pseudo-Step . . . . .	67
VI. CONCLUSIONS . . . . .	71
6.1 Summary . . . . .	71
6.2 Contributions . . . . .	72

6.3 Future Work . . . . .	73
APPENDIX	
A. RIGID BODY TRANSFORMATIONS FOR RALF . . . . .	74
B. DIMENSIONS OF MASTER ARM . . . . .	82
C. EQUIPMENT LIST . . . . .	84
D. IMPULSE RESPONSE OF A SECOND-ORDER SYSTEM . . . . .	87
E. SUMMATION OF TWO SINUSOIDS . . . . .	93
F. CALCULATIONS FOR TWO IMPULSES . . . . .	98
G. CALCULATIONS FOR THREE IMPULSES . . . . .	102
H. CALCULATIONS FOR FOUR IMPULSES . . . . .	109
I. CALCULATIONS FOR DEVIATIONS IN NATURAL FREQUENCY . . . . .	119
J. CALCULATIONS FOR DEVIATIONS IN DAMPING RATIO . . . . .	127
K. CIRCUIT FOR ACQUIRING FREQUENCY DATA . . . . .	135
L. LEAST-SQUARES REGRESSION OF EXPERIMENTAL DATA . . . . .	137
BIBLIOGRAPHY . . . . .	142



## LIST OF TABLES

Table	Page
4.1 Fundamental Damped Natural Frequencies vs. Joint Coordinates . . . . .	50
4.2 Fundamental Natural Frequencies vs. Joint Coordinates . . . . .	50
4.3 Damping Ratios vs. Joint Coordinates . . . . .	51
4.4 Normalized Frequencies vs. Joint Coordinates . . . . .	53
4.5 Normalized Damping Ratios vs. Joint Coordinates . . . . .	53



## LIST OF ILLUSTRATIONS

Figure	Page
2.1 Two-Link Flexible Manipulator . . . . .	8
2.2 The Workspace of RALF . . . . .	9
2.3 Coordinate Frames for RALF . . . . .	10
2.4 Teleoperated System . . . . .	14
3.1 Second-Order System . . . . .	18
3.2 Two Impulse Input . . . . .	25
3.3 System Response to Each Impulse . . . . .	26
3.4 Overall System Response to Two Impulse Input . . . . .	27
3.5 Single Impulse Response vs. Two Impulse Response . . . . .	27
3.6 Three Impulse Input . . . . .	29
3.7 Four Impulse Input . . . . .	30
3.8 Vibration Error vs. Normalized Frequency	
Singer's Definition for Two Impulse Input . . . . .	33
3.9 Vibration Error vs. Normalized Frequency	
Two Impulse Input . . . . .	34
3.10 Single Impulse Response vs. Two Impulse Response . . . . .	35

3.11	Vibration Error vs. Normalized Frequency	
	Three Impulse Input . . . . .	36
3.12	Vibration Error vs. Normalized Frequency	
	Four Impulse Input . . . . .	36
3.13	Vibration Error vs. Normalized Damping Ratio . . . . .	37
3.14	Input Shaping Block Diagram . . . . .	38
3.15	Steady-State Output for an Increase in Discrete-Time	
	Period Using Input Shaping . . . . .	43
3.16	Steady-State Output for a Decrease in Discrete-Time	
	Period Using Input Shaping . . . . .	44
3.17	Steady-State Output for an Increase in Discrete-Time	
	Period Using Modified Command Shaping . . . . .	45
3.18	Steady-State Output for a Decrease in Discrete-Time	
	Period Using Modified Command Shaping . . . . .	46
5.1	Block Diagram of Control System . . . . .	56
5.2	Principal Circle Trajectory . . . . .	57
5.3	Frequency Response of RALF	
	P.D. vs. Input Shaping	
	No Perturbation . . . . .	58
5.4	Frequency Response of RALF	
	P.D. vs. Modified Command Shaping	
	No Perturbation . . . . .	60



5.5	Picture of Tip Motion Using P.D. Control	
	No Perturbation . . . . .	60
5.6	Picture of Tip Motion Using Input Shaping	
	No Perturbation . . . . .	61
5.7	Picture of Tip Motion Using Modified Command Shaping	
	No Perturbation . . . . .	61
5.8	Circle Trajectory with 1 Hz Perturbation . . . . .	62
5.9	Frequency Response of RALF	
	P.D. vs. Modified Command Shaping	
	1 Hz Perturbation . . . . .	63
5.10	Circle Trajectory with 4.8 Hz Perturbation . . . . .	64
5.11	Frequency Response of RALF	
	P.D. vs. Modified Command Shaping	
	4.8 Hz Perturbation . . . . .	64
5.12	Picture of Tip Motion Using P.D. Control	
	4.8 Hz Perturbation . . . . .	65
5.13	Picture of Tip Motion Using Modified Command Shaping	
	4.8 Hz Perturbation . . . . .	65
5.14	Circle Trajectory with 10 Hz Perturbation . . . . .	66
5.15	Frequency Response of RALF	
	P.D. vs. Modified Command Shaping	
	10 Hz Perturbation . . . . .	67

5.16	Pseudo-Step Trajectory . . . . .	68
5.17	Pseudo-Step Response of RALF	
	P.D. vs. Modified Command Shaping . . . . .	68
5.18	Picture of Tip Motion Using P.D. Control	
	Pseudo-Step Input . . . . .	70
5.19	Picture of Tip Motion Using Modified Command Shaping	
	Pseudo-Step Input . . . . .	70
A.1	Rigid Body Coordinate Systems for RALF . . . . .	75
B.1	Dimensions of Master Arm . . . . .	83
D.1	Spring-Mass-Damper System . . . . .	87
D.2	Dirac Delta Function . . . . .	90
K.1	Circuit Used to Combine Random Noise with Control Signal . . . . .	136

## SUMMARY

The objective of this research is to reduce the end-point vibration of a large, teleoperated manipulator while preserving the usefulness of the system motion. A master arm is designed to measure desired joint angles as the user specifies a desired tip motion. The desired joint angles from the master arm are the inputs to an adaptive P.D. control algorithm that positions the end-point of the manipulator. As the user moves the tip of the master, the robot will vibrate at its natural frequencies which makes it difficult to position the end-point. To eliminate the tip vibration during teleoperated motions, an input shaping method developed by Singer and Seering from MIT is presented.

The input shaping method transforms each sample of the desired input into a new set of impulses that do not excite the system resonances. The method is explained using the equation of motion for a simple, second-order system. The impulse response of such a system is derived and the constraint equations for vibrationless motion are presented. To evaluate the robustness of the method, a different residual vibration equation from Singer's is derived that more accurately represents the input shaping technique. The input shaping method will be shown to actually increase the residual vibration in certain situations when the system parameters are not accurately specified. Finally, the implementation of the input shaping method to a system with varying parameters is shown to induce a vibration into the system. To eliminate this vibration, a modified

command shaping technique is developed. The ability of the modified command shaping method to reduce vibration at the system resonances is tested by varying input perturbations to trajectories in a range of possible user inputs. By comparing the frequency responses of the transverse acceleration at the end-point of the manipulator, the modified method is compared to the original P.D. routine. The control scheme that produces the smaller magnitude of resonant vibration at the first natural frequency is considered the more effective control method.

# **CHAPTER I**

## **INTRODUCTION**

### **1.1 Motivation for this Research**

The industrial applications for robots with a relatively large workspace has increased significantly over the past few years. Most of the attention has been focused on the assembly of large space structures, the welding of airplanes and automobiles, the weaving of new composite structures such as submarines and, more recently, the inspection and removal of hazardous waste [9,22,23,48]. With an expanded workspace, the robot is often required to move large distances in a relatively short amount of time. The demand for a high speed robot with a large workspace usually requires long, lightweight links which are inherently flexible. This flexibility allows the link to store potential energy which is often returned to the system in the form of kinetic energy. Therefore, the end-point vibration of the manipulator, as well as uncertainty in the end-point position, can be directly related to the inherent flexibility of the links.

For space and hazardous waste environments, a remote operator is needed to perform most of the required tasks. The user often dictates the motion of the robot through the workspace and then precisely positions the end-point of the manipulator to perform a task. A teleoperated system is ideal for the user interaction requirements. Through the use of a joystick or other input device, the operator can specify the desired

trajectory in either end-point coordinates or joint coordinates. Therefore, the user's desired motion can be transformed into actual robot motion.

This research addresses the end-point vibration of a large, teleoperated manipulator. Present methods for reducing end-point vibration are discussed to determine the appropriate strategy to reduce tip vibration of the manipulator.

## **1.2 Previous Methods for Reducing Vibration**

The problem of reducing end-point vibration is not a new one. Many different methods, both passive and active, have been investigated to eliminate unwanted oscillations. The most crude passive approach to eliminate vibration is to simply wait for the vibrations to stop after a desired motion. NASA originally used this method on their Space Shuttle Remote Manipulator System but found it to be costly in completion time requirements. Alberts and Book [1,2] experimented with a thin film of visco-elastic material that is applied to the structure surface and then covered with a very stiff constraining layer. When the beam is deformed, the visco-elastic material is sheared and thus energy is dissipated. The major drawback is that the vibrations are not eliminated but just reduced in amplitude.

The majority of the strategies to eliminate end-point vibration involve active control structures. Different states of the system are measured and control efforts are based upon them. As with many effective control schemes, an accurate model of the system is required. Book [6] used distributed and lumped parameter models for each arm segment. The models are combined using homogeneous transformations and then

numerical techniques are used to derive frequency domain information. Book [7] later derived the recursive dynamic equations for a flexible manipulator. However, the recursive method must be evaluated symbolically to obtain the dynamic equations in closed form. Finally, Book [8] reviews the mathematical representations commonly used in modeling flexible systems.

Hastings and Book [17] extended active control methods by including strain feedback in the control structure. Their experiments showed that strain feedback can reduce the residual vibration during settling time. However, they concluded that the vibrations are inevitable with a feedback control scheme because the feedback control signal contains high frequency components, which excite the system resonances.

Montgomery, Ghosh and Kenny [33] propose torque-wheel actuators to reduce overshoot in the Space Shuttle Remote Manipulator. Their method uses an inertial device to assist in reducing end-point vibration when following telerobotic commands. The results from their experiments indicate that the torque-wheel can produce a vibration of significant amplitude to diminish the original vibration while under teleoperated control. However, this procedure requires external devices to be mounted on the robot and is shown to work only for an abrupt stop command.

Tewani, Walcott and Rouch [45] suggest using a dynamic absorber as a viable means for suppressing vibrations of a system. The method involves the combination of passive elements, active elements and an absorber mass to apply a controlling force to the system. Using a disturbance rejection control strategy, the amplitude of vibration was significantly reduced. However, this method would be difficult to implement on a

teleoperated system because the disturbances are never known exactly. By implementing a Linear Quadratic Regulator (LQR) controller, a reduction in amplitude of vibration was still observed.

Presently, Lee and Book [28,29] are studying the effects of inertial forces to suppress the vibration of a large, flexible robot. By mounting a small robot at the tip of the large robot, damping forces are generated to accommodate the inertial forces generated when the tip vibrates. Simulation results have shown the effectiveness of the damping forces and the controller designed. Using deflection rate control, vibrations are damped in half the time required with passive control. Currently, Lee is conducting experiments using the prescribed robot configuration to verify simulation results.

Singer and Seering [39,40] presented a method of generating shaped command inputs to reduce end-point vibration. Unlike the previous methods which measure system states to reduce vibration, Singer's method utilizes system information to alter input commands to the actuators. Each commanded impulse is appropriately distributed into a multiple impulse input whose characteristics are based on the system's natural frequencies and damping ratio. This procedure, in effect, filters out frequency components near the system's resonances to avoid exciting the system. Later, Singer and Seering [38,42] show that the input shaping idea is effective with teleoperator inputs. However, their system was limited to a beam operating in the horizontal plane so that the natural frequency was constant for a given experiment.



### 1.3 Characteristics of a Flexible System

The equations of motion of a flexible system can be quite complex when compared to the rigid body counterpart. Lagrange's equations of motion produce an infinite number of vibrational modes and frequencies for just a simple Euler beam [14,31,32]. The ability to regulate these modes is limited by the bandwidth of the control system. Therefore, only a finite number of modes of a flexible system can be controlled.

Nonlinear effects due to large tip velocities may also need consideration. The centrifugal and Coriolis accelerations may generate additional tip vibration that is not controllable with conventional feedback schemes. The deflection of the manipulator due to vibration may also exhibit nonlinear properties if the amplitude of vibration is large relative to the link length.

The nonminimum phase characteristic of flexible systems must also be considered for tracking teleoperated inputs. Kwon and Book [24,25] show that the transfer function between the input at a joint and the end-point position has zeros with positive real parts. These right-half complex plane zeros cannot be canceled using conventional feedback control algorithms. This prevents the feedback controller from having asymptotic tracking stability.

Finally, the issue of noncollocated control must be mentioned. Noncollocated control occurs when the control effort and the sensing of the system states do not occur at the same point in the system. An example is when a robot is actuated at the joints but the end-point position is sensed at the tip. Often, nonminimum phase characteristics arise

when a system is noncollocated. Therefore, a noncollocated, state feedback control scheme must be designed with some consideration for system instability.

#### **1.4 Method of Approach**

The main focus of this research is the alleviation of end-point vibration in a telerobotic system. To avoid the complex derivation of dynamic equations, an adaptive control strategy derived by Yuan is used [49,50]. His controller was based on the error between the desired joint angles and the actual joint angles. By devising an operator input device that commands desired joint angles, Yuan's controller was easily transformed to work as a teleoperated control system.

This control structure is then compared to a control scheme that performs input shaping to the joint error signal. First, the original input shaping method developed by Singer is implemented and shown to produce a vibration in the system. To prevent this vibration, a modified command shaping technique is developed.

The advantages of using this new modified method over the original adaptive control scheme are then examined. By giving the two control methods identical input trajectories, the frequency responses of the transverse acceleration at the end-point of the manipulator are compared. The control scheme that produces the smaller magnitude of resonant vibration at the first natural frequency of the system is considered the more effective control method.

## **CHAPTER II**

### **EXPERIMENTAL TEST BED**

#### **2.1 Description of the Robotic Manipulator**

The flexible manipulator used in the Flexible Automation Laboratory at Georgia Tech was designed by a Master's student in 1986. Wilson [47] designed the robot to carry a payload of around 100 pounds, to reach second story windows and to be lightweight. To meet the design specifications, a two degree-of-freedom manipulator was built using 10 feet long, aluminum links. By choosing aluminum, the structure remains lightweight with good strength properties.

The manipulator, named RALF (Robotic Arm, Large and Flexible), is shown in Figure 2.1. Both links are maneuvered using single ended hydraulic actuators. Actuator one is attached directly to a collar on link one while actuator two positions link two using a four-bar parallel mechanism. This parallel mechanism gives much needed support to allow the robot to lift the 100 pound payload requirement. The mechanism also stiffens the overall structure which raises the system natural frequencies. However, this parallel linkage produces nonlinear effects (e.g. dead bands) and couples the dynamics of the two links together.

The nonlinear dynamic equations of motion were derived by Lee [26] using Lagrange's equation. These nonlinear equations were evaluated in symbolic form and

then, using single value decomposition, the constrained dynamic system was solved.

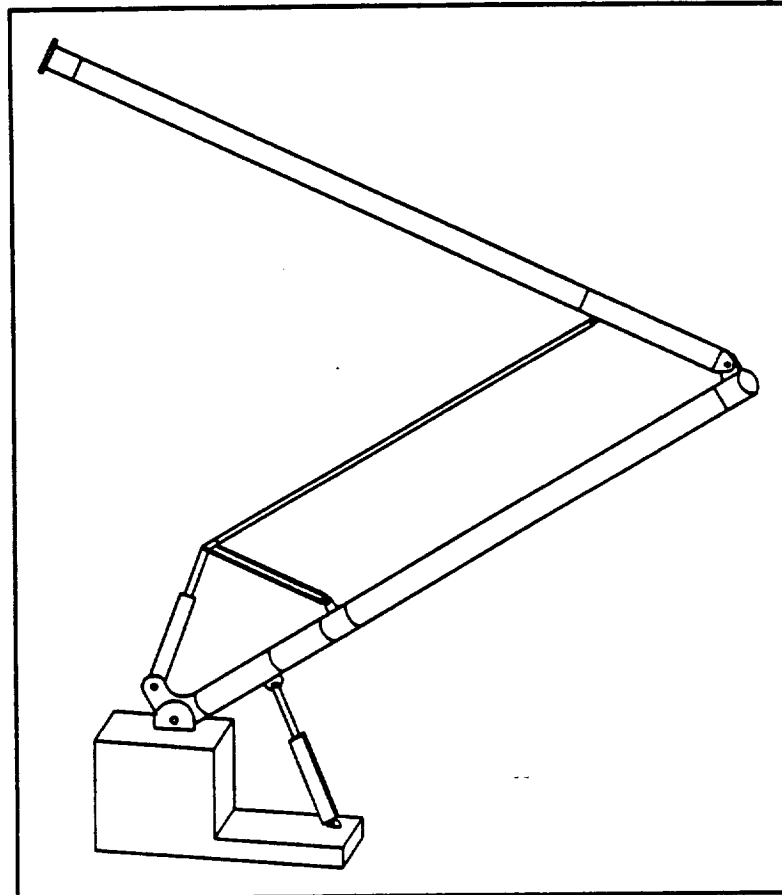


Figure 2.1 Two-Link Flexible Manipulator

Since hydraulic actuators are used, the joint motions are limited. Joint one has a range from  $35^\circ$  to  $110^\circ$ , which is measured from the horizontal plane. Joint two is limited to angles of  $55^\circ$  to  $108^\circ$  when measured relative to link one. Even with limited joint motion, the workspace, shown in Figure 2.2, is still quite large. Notice how the first link of RALF is able to pass through the vertical axis,  $y_0$ , that intersects joint one. This allows the center of gravity of the manipulator to move from one side of the axis

to another which can create unusual dynamics for the actuator connected to link one. Since the forces required for a given motion are different in each region, the actuator dynamics play an important role in the frequency analysis conducted in Chapter IV.

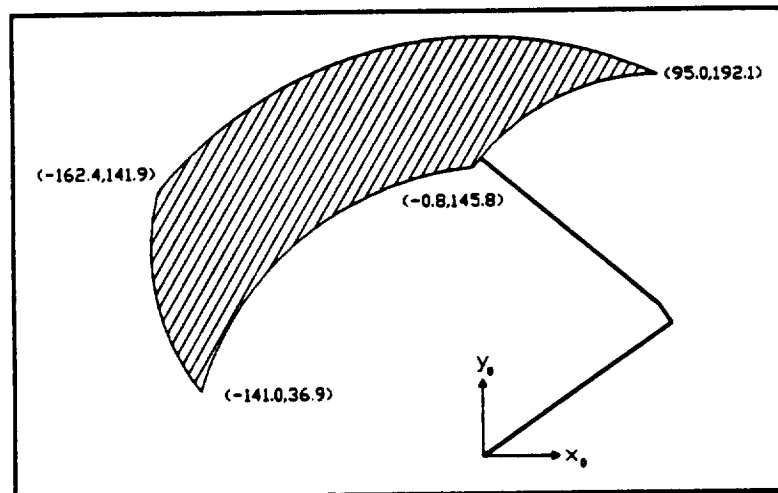


Figure 2.2 The Workspace of RALF

Now that the physical structure of RALF has been discussed, the forward and inverse kinematics are presented. The derivation of the kinematic equations is best handled using matrix transformations. By representing each degree of freedom of the manipulator with an individual coordinate frame, a matrix transformation is created [11,44]. Each matrix transformation relates the current coordinate system to the previous one. The overall transformation, relating the end-point to the base of the robot, is obtained by multiplying the individual matrix transformations together. For a flexible system, Book [7] demonstrated that the overall matrix transformation is actually the superposition of a rigid body transformation and a flexible transformation. This stems

from the fact that the position of a point in a flexible system can be described using rigid body coordinates along with the modes of vibration. The rigid body coordinate frames used for RALF are shown in Figure 2.3.

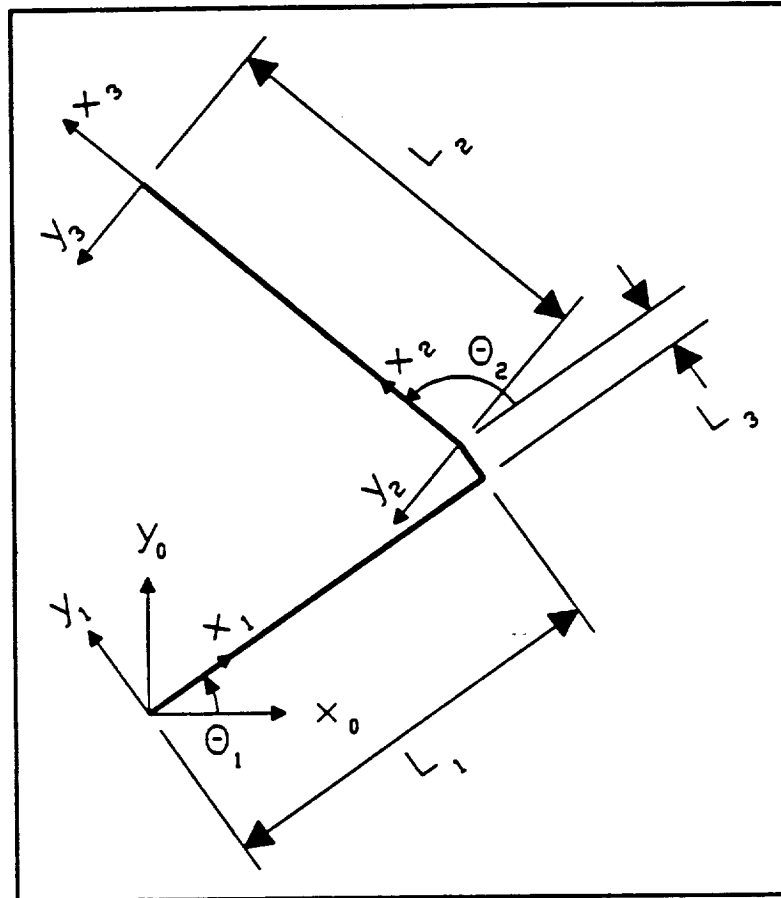


Figure 2.3 Coordinate Frames for RALF

For slow motions, the flexible modes of vibration may not be excited. In this situation, the rigid body transformations give a reasonable approximation of the tip position. Since modeling of the flexible dynamics is not the main emphasis of this research, only the rigid body transformations are considered. The rigid body

transformations for RALF are given in Appendix A.

The forward kinematics problem can be stated as follows: given the joint variables of the robot, determine the position and orientation of the end-effector. For RALF, only the (x,y) coordinates of the end-point are important. From the overall matrix transformation given in Appendix A, the last column yields the desired kinematic equations. The forward kinematic equations are

$$x = L_2 \cos(\theta_1 + \theta_2) + L_1 \cos(\theta_1) - L_3 \sin(\theta_1) \quad (2.1)$$

$$y = L_2 \sin(\theta_1 + \theta_2) + L_1 \sin(\theta_1) + L_3 \cos(\theta_1) . \quad (2.2)$$

The inverse kinematics problem is more difficult than the forward kinematics solution. The inverse situation simply stated is: given a desired position and orientation for the end-effector, determine all the possible joint configurations that achieve the desired position and orientation. Since the resulting kinematic equations are nonlinear, there is no guarantee of finding a unique solution or even finding a real solution at all.

The existence of a solution defines the workspace of the manipulator. The lack of a solution indicates that the desired position and orientation are not within the robot's workspace.

From Appendix A, the inverse kinematic equations are

$$\theta_2 = \text{atan2} \left( \frac{KL_3 + L_1 \sqrt{4L_2^2(L_1^2 + L_3^2) - K^2}}{KL_1 - L_3 \sqrt{4L_2^2(L_1^2 + L_3^2) - K^2}} \right) \quad (2.3)$$

$$\theta_1 = \text{atan2} \left( \frac{-x(L_2 \sin(\theta_2) + L_3) + y(L_2 \cos(\theta_2) + L_1)}{x(L_2 \cos(\theta_2) + L_1) + y(L_2 \sin(\theta_2) + L_3)} \right) \quad (2.4)$$

where

$$K = x^2 + y^2 - L_1^2 - L_2^2 - L_3^2. \quad (2.5)$$

## 2.2 Design of an Input Device

The main function of the input device in teleoperation is to assist the operator in accurately maneuvering the end-point of the manipulator. By sensing the user's desired motions, the device should convert these motion commands to movements of the end-point. The design of such an input device should be functional and suitable for the specific application.

Fischer, Daniel and Siva [13] discuss many guidelines for the design of input devices for use in teleoperation. The engineering group emphasized the necessity of the feedback of key information such as position and forces to avoid damage to the robot.



Since bracing of the manipulator is not considered and the workspace of RALF is unobstructed, only the relative position of the tip in the workspace is necessary.

Since RALF has only two degrees of freedom, the design of the input device was quite simple. A two link scaled model of RALF was designed with linear potentiometers placed at each joint to record the user joint commands. By moving the master arm, the operator can think of positioning the end-point of the manipulator in Cartesian coordinates while the input device functions in joint coordinates. This strategy of measuring joint commands directly works well with the adaptive control routine developed by Yuan discussed in Chapter I.

The overall teleoperated system designed to position the end-point of RALF is shown in Figure 2.4. The workspace of RALF is mounted as a backdrop to give the operator a scaled picture of the allowable workspace. This arrangement makes it easier for the user to make relative maneuvers within the workspace.

### **2.3 Interfacing the Telerobotic System**

The coordination of the master arm with the slave arm in a telerobotic system is important to produce desired results. Fiala [12] describes a logical architecture for connecting teleoperation input devices to the telerobotic control hierarchy. A method of handling control information is presented which allows many system components to access the information simultaneously. He also explains the two main classes of teleoperation input devices, joint-space devices and Cartesian devices.

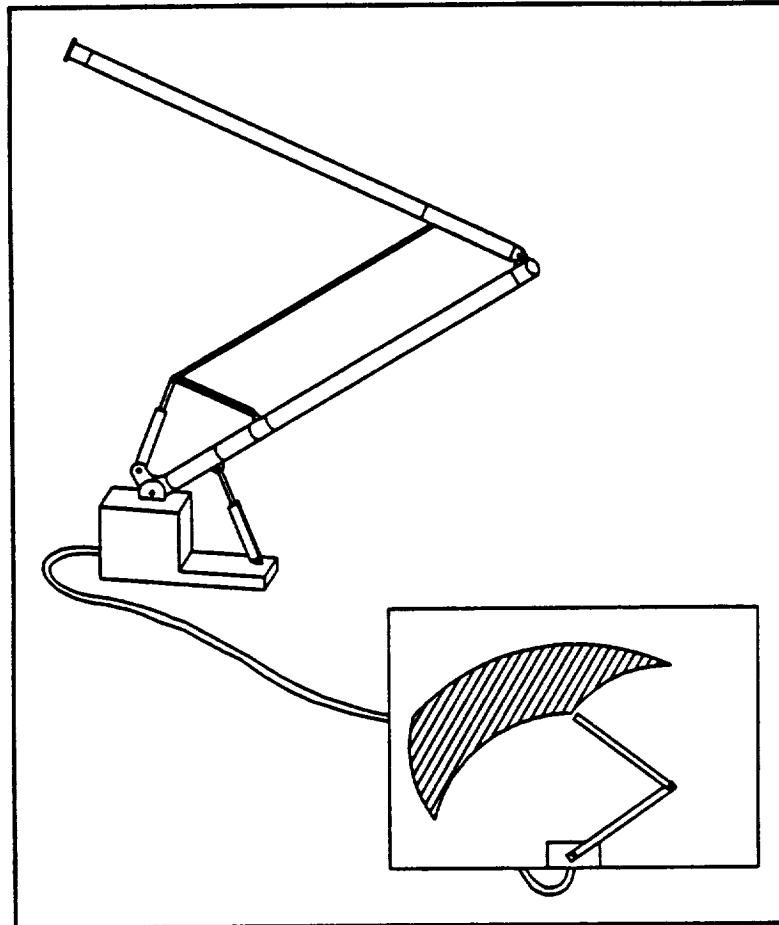


Figure 2.4 Teleoperated System

The effects of varying system parameters on the ability of the operator to position the end-point of the manipulator should be understood. Hannema and Book [15] discuss moving the end-point of a manipulator from one point to within a certain tolerance band surrounding a desired point. They examined the effects of backlash, Coulomb friction and bandwidth on the ability of an operator to position the end-point of a manipulator. They showed that a linear model, relating the task parameters of distance and width to performance in task completion time, could be made. Their experimental results

revealed an improvement in task completion time as the joint bandwidths were increased from 1 to 3.5 Hz.

Uebel, Ali and Minis [46] also investigated the effects of bandwidth on operator performance using a Robotics Research Corporation slave arm with a Kraft Telerobotics master arm. Varying the joint bandwidths from 0.5 to 2 Hz, experienced operators performed five repetitions of a peg-in-a-hole task for three different bandwidths. Their results also show a decline in operator performance as the bandwidth is decreased.

The final issue that must be considered when interfacing telerobots is the effects of time-delay. Niemeyer and Slotine [34] address the problem of time-delays in telerobotics by using an adaptive control strategy. By using an adaptive controller, the manipulator bandwidth is not limited to the bandwidth imposed by the transmission delays. However, the type of data that is transmitted (e.g. forces, torques) can alter the behavior and stability of the overall system.

## 2.4 System Hardware

The telerobotic system used for experiments at Georgia Tech consists of the input device discussed in Section 2.2 functioning as the master, and RALF as the slave. The main control unit is a MicroVAX II made by Digital Equipment Corporation. The necessary connections to the sensors, hydraulic valves, amplifiers and master arm are made using an analog/digital (A/D) board made by Data Translation (see Appendix C for equipment list). The A/D boards can sample a single channel at 6000 Hz. However, eight channels sample at only 300 Hz. A second A/D board is available but a one

millisecond delay is required to switch from one board to the next board.

After the computation time for the control routines is considered, the sampling frequency is reduced to 50 Hz. The frequencies of RALF to be controlled range from 3.7 to 5.5 Hz. From Nyquist criterion, the A/D sampling rate is still sufficient to control these system frequencies.

The adaptive control algorithms, the modified command shaping routines and the A/D routines were written in VAX C. Previous control routines were written in FORTRAN (FORmula TRANslation) and had sampling rates of around 150 Hz. Obviously, the FORTRAN code runs almost three times faster than the C code. Test programs verify that the MicroVAX II machine is optimized to run Fortran code. The VAX C language was chosen for portability to personal computers (PC) where future control will be implemented.

## **CHAPTER III**

### **MODIFIED COMMAND SHAPING**

#### **3.1 Historical Perspective**

The original command shaping technique to reduce system vibration was introduced by Singer and Seering in 1988 [39]. The procedure involved modifying desired system inputs so that a system completes the requested motion without vibration. The method was tested on a computer model of the Space Shuttle Remote Manipulator System (RMS) developed by Draper Laboratories. Simulation results from a variety of commanded moves suggested that significant vibration reduction can be obtained using the method. Subsequent documents [40,41] verified the ability of the method to reduce end-point vibrations.

By 1989, Singer showed that the procedure worked with multiple mode systems and was effective on telerobotic systems as well [38,42]. Singhose, Seering and Singer expanded the method using a vector diagram approach to determine the appropriate shaping strategy given some allowable residual vibration amplitude [43]. Hyde and Seering [21] extended these results to the solution of a group of simultaneous non-linear impulse constraint equations.

Recently, the input shaping method was implemented on an overhead crane to reduce oscillatory motion of the object being moved. Noakes and Jansen [35]

generalized the theory associated with oscillation-damped trajectories to a system with simply suspended loads. Previously, a crane operator moved the suspended object slowly and allocated time for pendulum oscillations to damp out. After implementing the oscillation-damping algorithms, they were able to position 55-gallon drums in a U-shaped path with insignificant oscillations.

### 3.2 Derivation of Constraint Equations

The original input shaping method involves the manipulation of a desired input command. Each sample of the input command is replaced by a sequence of impulses that do not excite the system natural frequencies. Knowing the impulse response of the system, constraint equations can be derived that yield the appropriate amplitudes and starting times of the impulse sequence.

The constraint equations can be derived from the impulse response of a simple linear, time-invariant second-order system. Consider the spring-mass-damper system

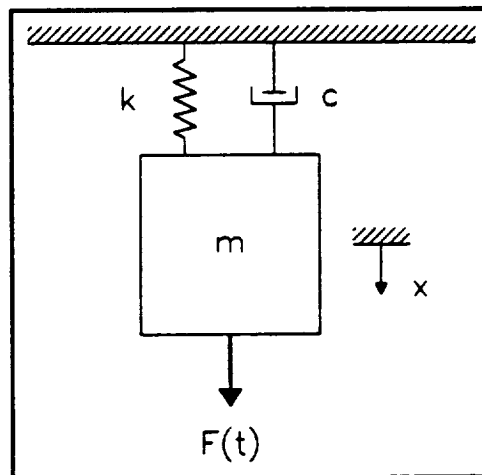


Figure 3.1 Second-Order System

shown in Figure 3.1. The vibratory response of this system to an impulse input is

$$x(t) = \frac{A \omega_n e^{-\zeta \omega_n (t-t_0)}}{\sqrt{1-\zeta^2}} \sin(\omega_n \sqrt{1-\zeta^2} (t-t_0)) \quad (3.1)$$

where  $A$  is the amplitude of the impulse,  $\omega_n$  is the natural frequency of the system,  $\zeta$  is the damping ratio of the system,  $t$  is the time and  $t_0$  is the time when the impulse occurs. This result is derived in Appendix D. Using Equation (3.1), the position response,  $x(t)$ , for the second-order system is specified for time,  $t \geq t_0$ .

If the system is given a two impulse input, the vibratory response is

$$x(t) = B_1 \sin(\alpha t + \phi_1) + B_2 \sin(\alpha t + \phi_2) \quad (3.2)$$

where

$$B_k = \frac{A_k \omega_n}{\sqrt{1-\zeta^2}} e^{-\zeta \omega_n (t-t_{0k})} \quad (3.3)$$

$$\alpha = \omega_n \sqrt{1-\zeta^2} \quad (3.4)$$

$$\phi_k = -\omega_n t_{0k} \sqrt{1-\zeta^2}. \quad (3.5)$$

The two impulse response given in Equation (3.2) can be simplified to yield

$$x(t) = B_{amp} \sin(\alpha t + \psi) \quad (3.6)$$

where

$$B_{amp} = \sqrt{[B_1 \cos(\phi_1) + B_2 \cos(\phi_2)]^2 + [B_1 \sin(\phi_1) + B_2 \sin(\phi_2)]^2} \quad (3.7)$$

$$\psi = \tan^{-1} \left( \frac{B_1 \sin(\phi_1) + B_2 \sin(\phi_2)}{B_1 \cos(\phi_1) + B_2 \cos(\phi_2)} \right). \quad (3.8)$$

The summation of two sinusoids is proven in Appendix E.

Since the system is linear and time-invariant, the results from Equations (3.7) and (3.8) can be generalized to the  $N$  impulse input case. The amplitude and phase of vibration for the  $N$  impulse input case are

$$B_{amp} = \sqrt{\left[ \sum_{k=1}^N B_k \cos(\phi_k) \right]^2 + \left[ \sum_{k=1}^N B_k \sin(\phi_k) \right]^2} \quad (3.9)$$

$$\psi = \tan^{-1} \left( \frac{\sum_{k=1}^N B_k \sin(\phi_k)}{\sum_{k=1}^N B_k \cos(\phi_k)} \right). \quad (3.10)$$



Since the purpose of the input shaping method is to eliminate vibration, the amplitude of vibration, Equation (3.9), must equal zero after the last impulse occurs. This only happens if both the squared terms are independently zero since the sine and cosine functions are linearly independent. The resulting equations are

$$B_1 \cos(\phi_1) + B_2 \cos(\phi_2) + \dots + B_N \cos(\phi_N) = 0 \quad (3.11)$$

$$B_1 \sin(\phi_1) + B_2 \sin(\phi_2) + \dots + B_N \sin(\phi_N) = 0 \quad (3.12)$$

including

$$B_k = \frac{A_k \omega_n}{\sqrt{1 - \zeta^2}} e^{-\zeta \omega_n (t_N - t_{0k})} \quad (3.13)$$

and

$$\phi_k = -\omega_n t_{0k} \sqrt{1 - \zeta^2}, \quad (3.14)$$

where  $A_k$  is the amplitude of the  $k^{\text{th}}$  impulse,  $t_N$  is the time when the final impulse occurs and  $t_{0k}$  is the time when the  $k^{\text{th}}$  impulse occurs.

Substituting the equations for  $B_k$  and  $\phi_k$  into Equations (3.11) and (3.12), the constraint equations become

$$\sum_{k=1}^N A_k e^{-\zeta \omega_n (t_N - t_{0k})} \cos(\omega_n \sqrt{1 - \zeta^2} t_{0k}) = 0 \quad (3.15)$$

$$\sum_{k=1}^N A_k e^{-\zeta \omega_n (t_N - t_{0k})} \sin(\omega_n \sqrt{1 - \zeta^2} t_{0k}) = 0. \quad (3.16)$$

For the constraint equations to produce the correct impulse sequence to eliminate vibration, the natural frequency and damping ratio of the system must be known exactly. Since these system characteristics are not precisely known, their robustness is included as a constraint. The robustness constraint with respect to natural frequency is found by taking the partial derivative of Equations (3.15) and (3.16) with respect to  $\omega_n$  and setting the result equal to zero. Likewise, the robustness constraint with respect to damping ratio is found by taking the partial derivative with respect to  $\zeta$  and setting this result equal to zero. After performing the described differentiation, the resulting constraint equations are the same. Therefore, setting the partial derivative with respect to  $\omega_n$  equal to zero is equivalent to setting the partial derivative with respect to  $\zeta$  equal to zero [38]. These new constraint equations form the first-derivative robustness criterion.

Mathematically, the equations for the first-derivative robustness criterion are

$$\sum_{k=1}^N A_k t_{0k} e^{-\zeta \omega_n (t_N - t_{0k})} \cos(\omega_n \sqrt{1 - \zeta^2} t_{0k}) = 0 \quad (3.17)$$

$$\sum_{k=1}^N A_k t_{0k} e^{-\zeta \omega_n (t_N - t_{0k})} \sin(\omega_n \sqrt{1 - \zeta^2} t_{0k}) = 0. \quad (3.18)$$

Higher derivative constraints are obtained by differentiating Equations (3.15) and (3.16) to the desired order. The  $m^{\text{th}}$ -derivative robustness constraint equations are

$$\sum_{k=1}^N A_k (t_{0k})^m e^{-\zeta \omega_n (t_N - t_{0k})} \cos(\omega_n \sqrt{1 - \zeta^2} t_{0k}) = 0 \quad (3.19)$$

$$\sum_{k=1}^N A_k (t_{0k})^m e^{-\zeta \omega_n (t_N - t_{0k})} \sin(\omega_n \sqrt{1 - \zeta^2} t_{0k}) = 0. \quad (3.20)$$

The length of the impulse sequence is now determined by the number of unknowns in a given set of constraint equations. For any given set, there will always be two more unknowns than equations. To alleviate this dilemma, the starting time of the first impulse is arbitrarily chosen to be time zero and the amplitudes are normalized so that they sum to one. This particular normalization ensures that the overall amplitude of the new impulse sequence is the same as the amplitude of the desired input command.

### 3.3 Calculation of Impulse Amplitudes

Now that the robustness constraint equations have been determined, the impulse amplitudes and starting times can be solved. For the two impulse input, the zero<sup>th</sup>-derivative constraint equations are utilized, which are

$$B_1 \cos(\phi_1) + B_2 \cos(\phi_2) = 0 \quad (3.21)$$

$$B_1 \sin(\phi_1) + B_2 \sin(\phi_2) = 0 \quad (3.22)$$

and

$$B_k = \frac{A_k \omega_n}{\sqrt{1 - \zeta^2}} e^{-\zeta \omega_n (t_N - t_{0k})}, \quad (3.23)$$

where  $A_k$  is the amplitude of the  $k^{\text{th}}$  impulse,  $t_N$  is the time when the final impulse occurs (i.e.  $t_{02}$ ) and  $t_{01}$  is the time when the first impulse occurs.

Since any equation involving sines and cosines is transcendental, there are an infinite number of possible solutions to Equations (3.21) and (3.22). Therefore, only the solution that yields the shortest time duration and a positive amplitude for all the impulses is chosen. For the two impulse input case, a complete derivation of the solution process is furnished in Appendix F.

The resulting solution for the two impulse case is

$$A_1 = \frac{1}{1+M} \quad (3.24)$$

$$t_{01} = 0 \quad (3.25)$$

$$A_2 = \frac{M}{1+M} \quad (3.26)$$

$$t_{02} = \frac{\pi}{\omega_n \sqrt{1-\zeta^2}} \quad (3.27)$$

where

$$M = e^{-\frac{\zeta \pi}{\sqrt{1-\zeta^2}}} \quad (3.28)$$

The ability of the input shaping method to eliminate vibration can be demonstrated graphically. Consider the input in Figure 3.2 whose characteristics are given in Equations (3.24) through (3.27).

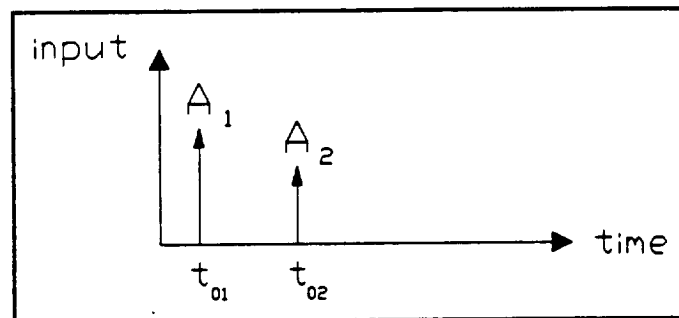


Figure 3.2 Two Impulse Input

The second-order system response to each of the individual impulses in Figure 3.2 is shown in Figure 3.3.

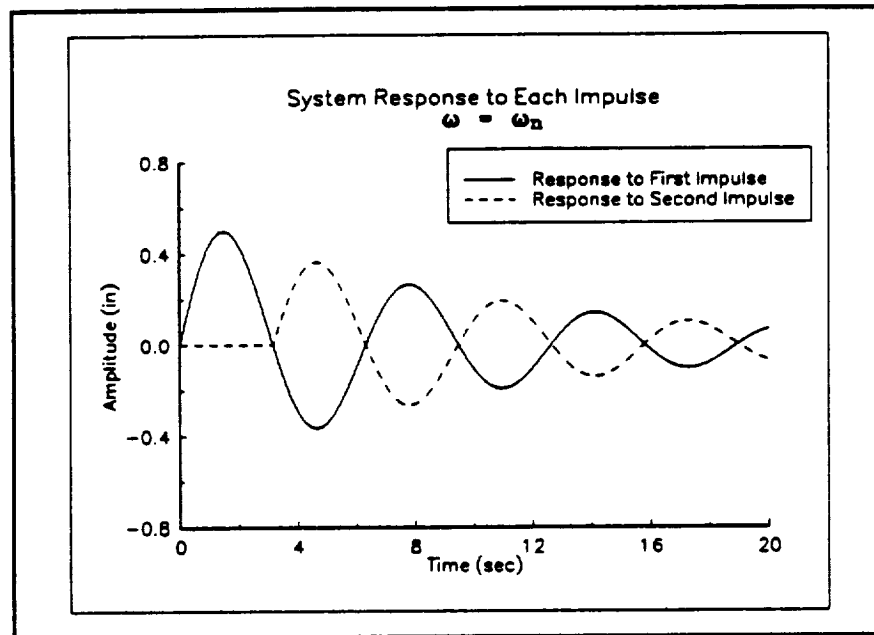


Figure 3.3 System Response to Each Impulse

Since the system is linear and time-invariant, a linear combination of two inputs results in a response that is a linear combination of the two responses. Therefore, the net system response to the two impulse input is shown in Figure 3.4. Since the natural frequency and damping ratio of the system are exact, there is no vibration of the system after the second impulse. The effects of parameter uncertainty on the amount of residual vibration is discussed in Section 3.4.

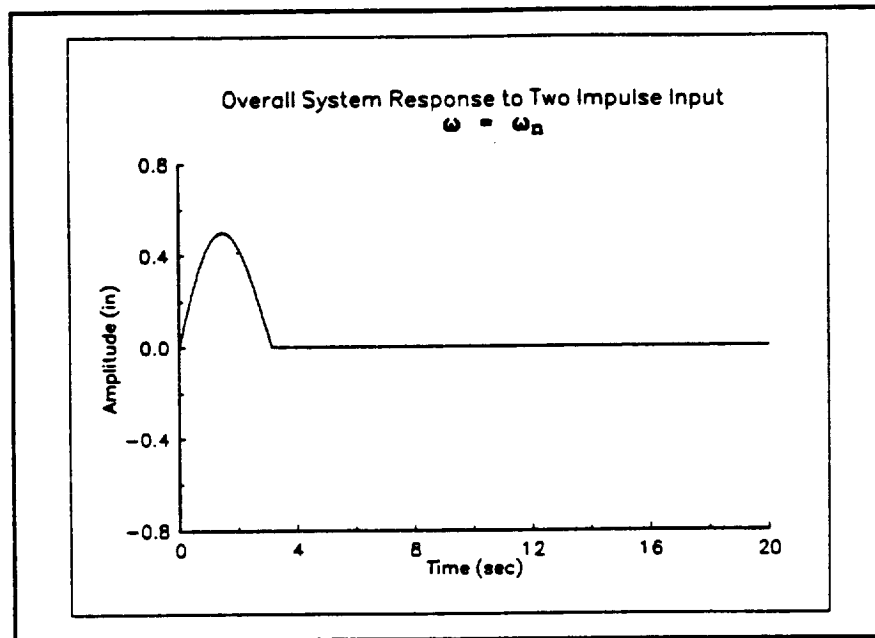


Figure 3.4 Overall System Response to Two Impulse Input

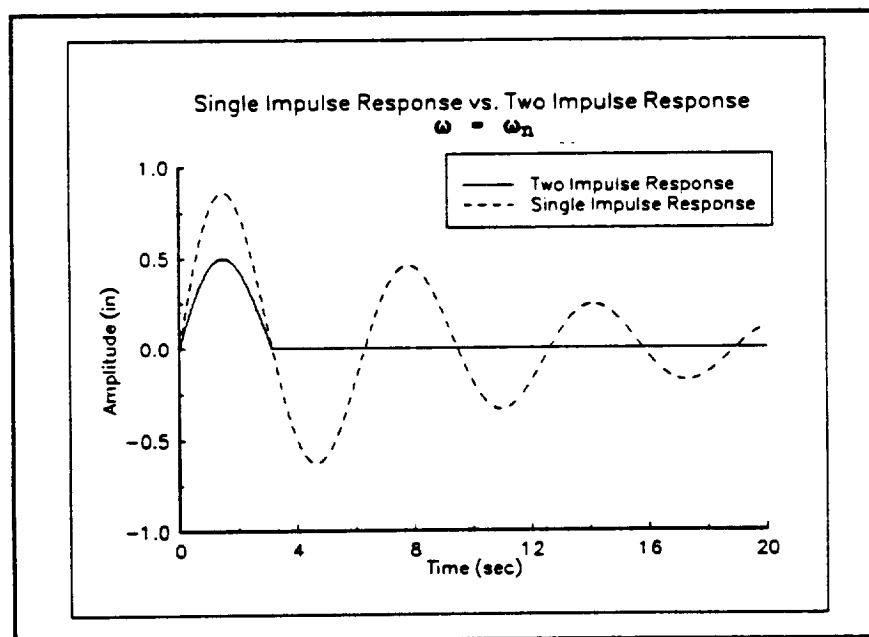


Figure 3.5 Single Impulse Response vs. Two Impulse Response

Figure 3.5 shows a comparison of the impulse response of a second-order system to the two impulse input response. Since the inputs have the same amplitude, i.e. they sum to one, the responses can be compared to determine which is more desirable. For this simple case, the two impulse input is preferred since it eliminates the vibration after the second impulse occurs. The ability to completely eliminate the vibration is attributed to an ideal second-order system model which provides exact system parameters.

To solve the three impulse input case, the zero<sup>th</sup> and first derivative constraint equations are evaluated. The complete derivation for the three impulse case is in Appendix G. The solution for this case is

$$A_1 = \frac{1}{1 + 2M + M^2} \quad (3.29)$$

$$t_{01} = 0 \quad (3.30)$$

$$A_2 = \frac{2M}{1 + 2M + M^2} \quad (3.31)$$

$$t_{02} = \frac{\pi}{\omega_n \sqrt{1 - \zeta^2}} \quad (3.32)$$

$$A_3 = \frac{M^2}{1 + 2M + M^2} \quad (3.33)$$

$$t_{03} = \frac{2\pi}{\omega_n \sqrt{1 - \zeta^2}} \quad (3.34)$$



Figure 3.6 shows the three impulse input case whose characteristics are given in Equations (3.29) through (3.34).

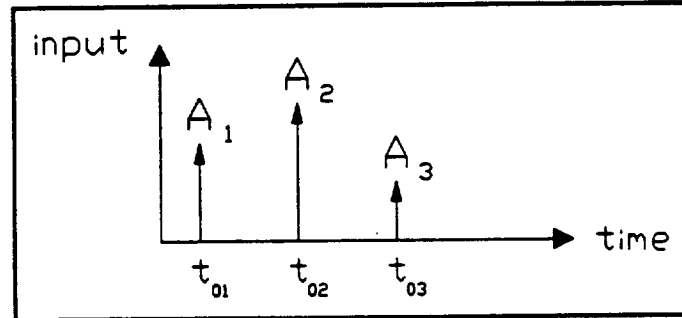


Figure 3.6 Three Impulse Input

Finally, the four impulse input case is solved. To obtain the amplitudes and starting times of the four impulses, the zero<sup>th</sup>, first and second derivative constraint equations must be solved. Appendix H contains the complete derivation for this case. The results from this appendix are

$$A_1 = \frac{1}{1 + 3M + 3M^2 + M^3} \quad (3.35)$$

$$t_{01} = 0 \quad (3.36)$$

$$A_2 = \frac{3M}{1 + 3M + 3M^2 + M^3} \quad (3.37)$$

$$t_{02} = \frac{\pi}{\omega_n \sqrt{1 - \zeta^2}} \quad (3.38)$$

$$A_3 = \frac{3M^2}{1 + 3M + 3M^2 + M^3} \quad (3.39)$$

$$t_{03} = \frac{2\pi}{\omega_n \sqrt{1 - \zeta^2}} \quad (3.40)$$

$$A_4 = \frac{M^3}{1 + 3M + 3M^2 + M^3} \quad (3.41)$$

$$t_{04} = \frac{3\pi}{\omega_n \sqrt{1 - \zeta^2}} \quad (3.42)$$

Figure 3.7 shows the four impulse input whose characteristics are given in Equations (3.35) through (3.42).

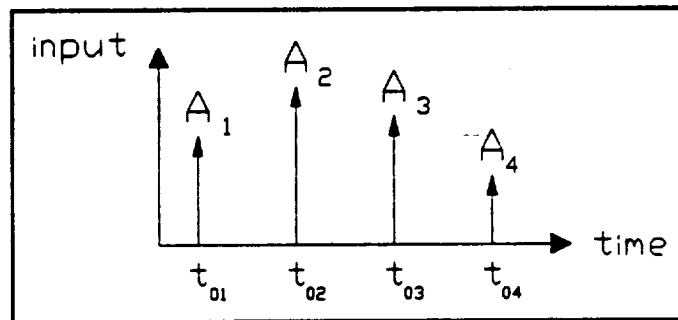


Figure 3.7 Four Impulse Input

### 3.4 Robustness of Constraint Equations

In Section 3.3, the two impulse input completely eliminated the vibration when the natural frequency and damping ratio of the system were known exactly. For most physical systems, the exact parameters are seldom known. Thus, there is some residual vibration after the last impulse has occurred.

To determine the amount of residual vibration, a vibration error expression must be defined. The error, denoted  $err$ , is written as the ratio of the actual multiple impulse response magnitude to the actual impulse response magnitude of the second-order system. The error expression is defined only for time after the multiple impulse input has occurred to ensure that the system has received identical amplitude inputs. Mathematically, the vibration error is written as

$$err = \frac{|x_{ka}(t)|}{|x_a(t)|}, \quad \text{for } t \geq t_{0k} \quad (3.43)$$

where  $k$  is the number of impulses. The residual vibration is just the vibration error expressed as a percentage.

The deviation in the actual system parameters from the design parameters can now be quantified using Equation (3.43). The actual system response to a multiple impulse input can be computed and related to the actual impulse response of the second-order system. By studying the deviations in the natural frequency and damping ratio from the

design parameters, their effects on the vibration error can be better understood.

This new definition of the vibration error expression is much different than the one originally stated by Singer. He defined the vibration error expression as "the maximum amplitude of the residual vibration during a move as a percentage of the amplitude of the rigid body motion." This definition is expressed mathematically with Equation (3.9) divided by the sum of all the  $A_k$  [39], which is always unity. The main problem with Singer's definition is that it does not accurately represent the ability of the input shaping method to reduce vibration. In some instances, the input shaping method can actually increase the residual vibration of a system.

To prove this point, the deviation in actual natural frequency,  $\omega_a$ , from the design natural frequency,  $\omega_n$ , is analyzed. The vibration error defined by Singer for the two impulse input case is shown in Figure 3.8. Singer states that an acceptable vibration error level is less than 5% residual vibration for a second-order system. Therefore, the two impulse input is robust for a frequency variation of less than 5%. From Figure 3.8, the residual vibration curves decrease in magnitude for an increase in the value of damping ratio,  $\zeta$ . The graph also shows that the magnitude never exceeds 100% and therefore the input shaping method can never increase the residual vibration of a system. This implies that the input shaping method reduces residual vibration for any variation in natural frequency. However, the new definition of residual vibration clearly shows this is not the case.

The vibration error from Equation (3.43) for the two impulse input case is

$$\frac{|x_{2e}(t)|}{|x_e(t)|} = \left| \frac{1}{M+1} \sqrt{1 + 2M \left(1 - \frac{\omega_a}{\omega_n}\right) \cos\left(\frac{\omega_a}{\omega_n} \pi\right) + M^2 \left(1 - \frac{\omega_a}{\omega_n}\right)^2} \right| \quad (3.44)$$

where  $\omega_a$  is the actual natural frequency of the system and  $\omega_n$  is the design natural frequency of the system. Equation (3.44) is derived in Appendix I. Figure 3.9 shows the new vibration error as a function of normalized frequency,  $\omega_a/\omega_n$ .

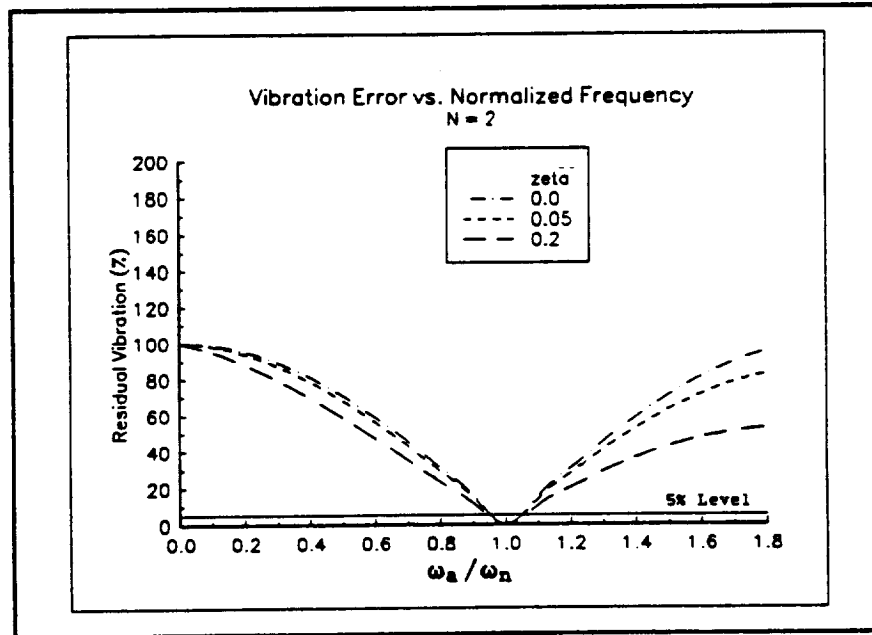


Figure 3.8 Vibration Error vs. Normalized Frequency  
Singer's Definition for Two Impulse Input

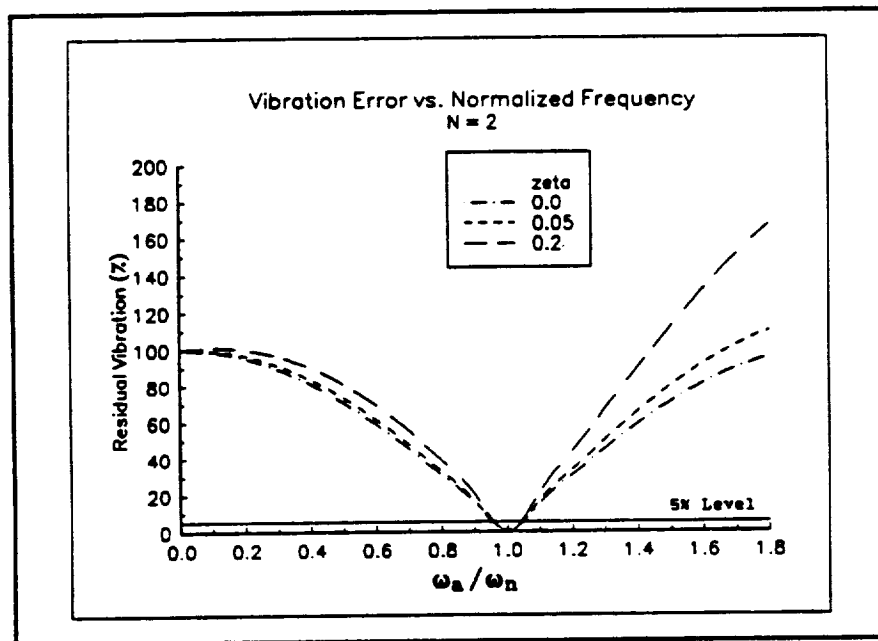


Figure 3.9 Vibration Error vs. Normalized Frequency  
Two Impulse Input

The residual vibration now increases for an increase in damping ratio,  $\zeta$ . This fact may seem incorrect since the overshoot of a second-order system increases with a decrease in damping ratio for a step input. However, analysis of the impulse response, given in Equation (3.1), verifies the results displayed in Figure 3.9.

Figure 3.9 also shows that replacing the original impulse by a sequence of impulses can actually have a negative effect if the actual natural frequency is over 1.5 times the design frequency. Figure 3.10 shows a second-order system response to a single impulse input compared to a two impulse input when the actual natural frequency is twice the design frequency. The residual vibration after the second impulse is actually worse than if the system had only been given the single impulse. Therefore, input shaping can have a detrimental effect when large errors in natural frequency are present.

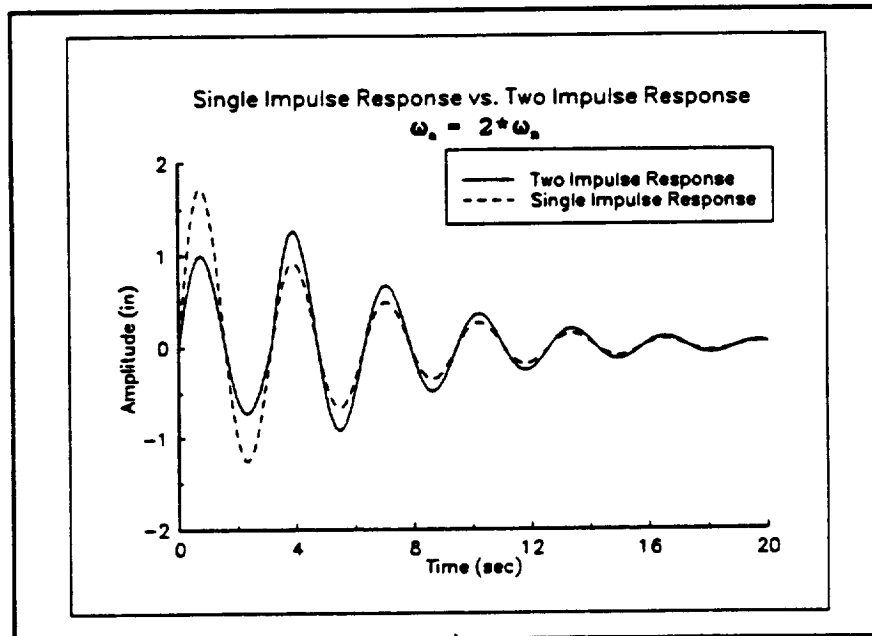


Figure 3.10 Single Impulse Response vs. Two Impulse Response

Since the two impulse input case is only robust for deviations in natural frequency of less than  $\pm 5\%$ , the robustness of the three and four impulse cases is of interest. Figure 3.11 shows the vibration error versus normalized frequency for the three impulse input. For this case, the input is robust for deviations in natural frequency near  $\pm 10\%$ . However, the ability of the input shaping method to produce detrimental effects is much more pronounced.

By separating the input into four new impulses, Figure 3.12 shows that the method is robust for deviations in natural frequency close to  $\pm 20\%$ . Nevertheless, the possible adverse effects are even more noticeable. If the actual frequency is more than 40% larger than the design frequency (for  $\zeta = 0.2$ ), then the input shaping method is of no practical use.

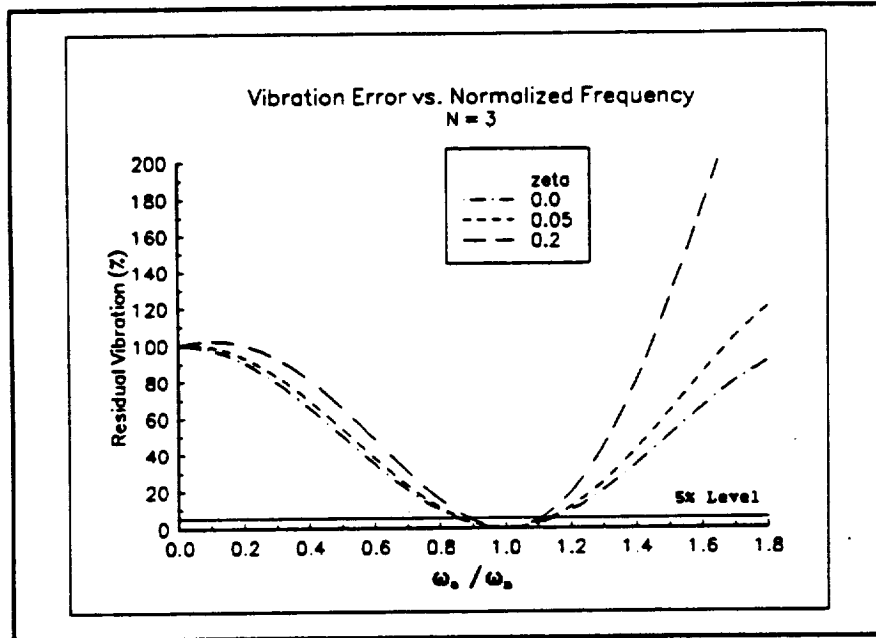


Figure 3.11 Vibration Error vs. Normalized Frequency  
Three Impulse Input

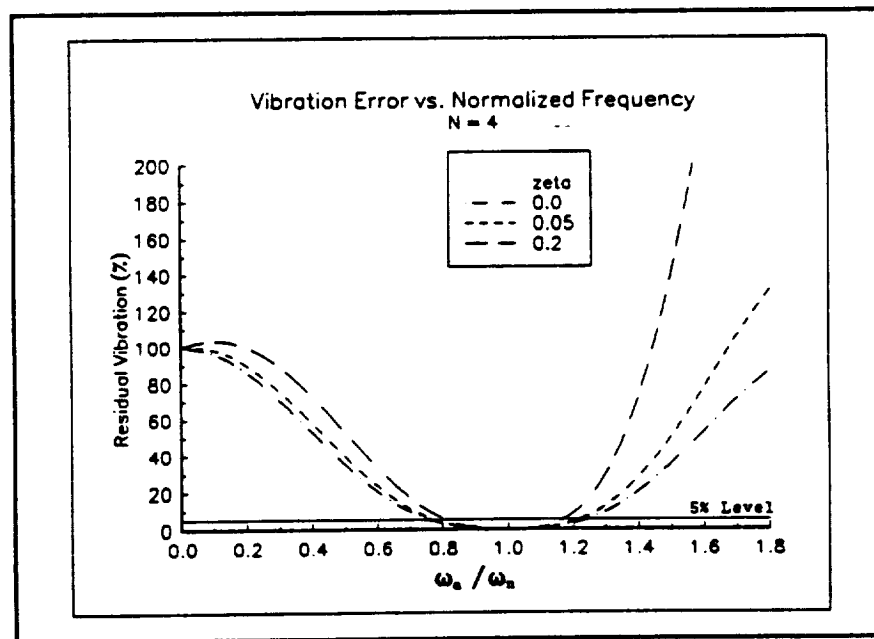


Figure 3.12 Vibration Error vs. Normalized Frequency  
Four Impulse Input



The input shaping method must also be robust for deviations in damping ratio. Section 3.2 stated that the derivative of the constraint equations with respect to damping ratio yields the same constraint equations as the derivative with respect to natural frequency. Therefore, robustness in damping ratio is already accomplished when robustness in natural frequency has been considered. Figure 3.13 shows the vibration error versus normalized damping ratio for the multiple impulse cases.

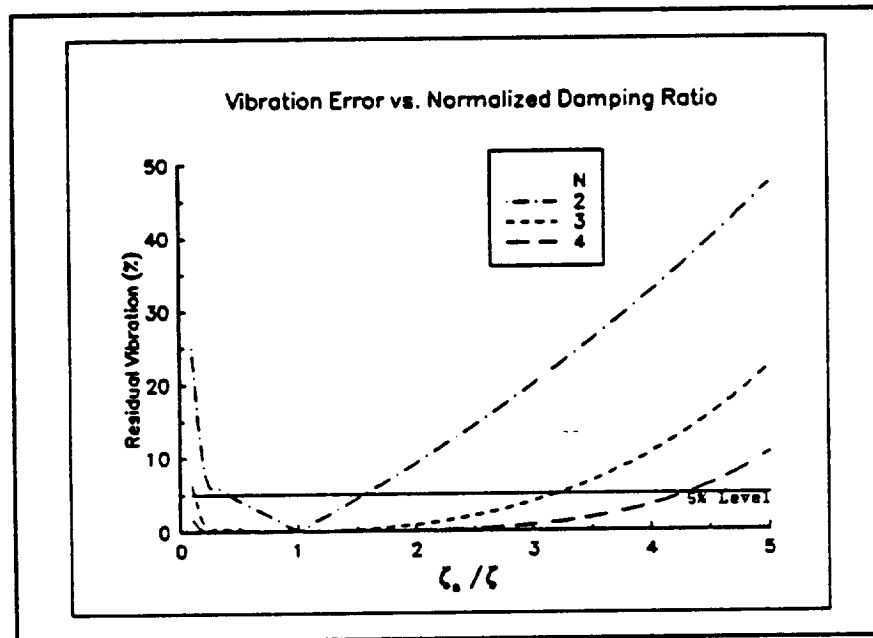


Figure 3.13 Vibration Error vs. Normalized Damping Ratio

To evaluate the error expressions for the deviation in damping ratio of a second-order system (see Appendix J), a specific value of damping ratio is required. For this example, the design damping ratio is 0.05. For all three input cases, large deviations in damping ratio do not have a significant effect on the residual vibration. This fact is comforting since the damping ratio for a complex system may be hard to measure.

### 3.5 Position Dependent System Parameters

The robustness of the constraint equations, discussed in Section 3.4, demonstrated the ability of the input shaping method to reduce vibrations even with deviations from the design system parameters. However, Singer's original input shaping technique does not address the issue of changing system parameters. For RALF, the natural frequency and damping ratio are functions of position, i.e. joint angles. Therefore, a modified command shaping technique was developed to accommodate varying system parameters.

First, the implementation of the input shaping technique to a discrete-time system is presented. Figure 3.14 shows a simple block diagram of the input shaping method. For each sample of the input,  $N$  output impulses are generated. From Section 3.3, the

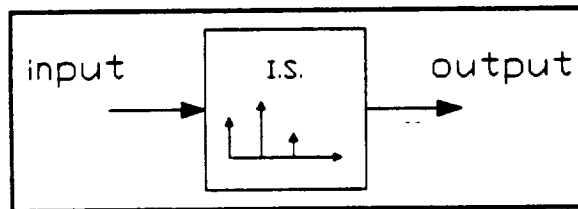


Figure 3.14 Input Shaping Block Diagram

time period between output impulses is the same. This time period, denoted  $\text{del}T$ , is

$$\text{del}T = \frac{\pi}{\omega_n \sqrt{1 - \zeta^2}} \quad (3.45)$$

which is a function of both the natural frequency,  $\omega_n$ , and the damping ratio,  $\zeta$ .

To utilize this time period information in a discrete-time system, the continuous-time data must be represented in discrete-time. From discrete-time signal processing, a continuous-time signal,  $x(t)$ , is represented mathematically as a sequence of numbers,  $x[n]$ , where  $n$  is strictly an integer. To transform the continuous-time period  $delT$  into a discrete-time period  $deln$ , the sampling rate of the discrete-time system,  $f_s$ , is used. The equation to perform this transformation is

$$deln = int ( delT * f_s ) \quad (3.46)$$

where the *int* function truncates the argument to an integer.

For the input shaping method, the discrete-time period,  $deln$ , never changes because the system parameters are assumed constant. But when the input shaping method is applied to a system that has time varying parameters, the continuous-time period,  $delT$ , becomes time varying as well. A significant change in  $delT$  will result in a change in the discrete-time period,  $deln$ , which produces an undesirable vibration in the system. The amount of change in the continuous period that causes this change in the discrete period is a function of sampling rate since  $deln$  is strictly an integer.

For example, a four impulse output, shaping scheme is applied to a system that causes a change in  $deln$  from four to five. When each input sample is shaped into four output impulses, the method would produce a steady-state impulse output shown in Figure 3.15. Each output impulse is designated  $\{a,b\}$  where  $a$  indicates the discrete-time location of the input sample responsible for the four output impulses and  $b$  indexes the

four resulting output impulses. After examining Figure 3.15, it is obvious that the change in  $deln$  has caused gaps in the output for discrete values of  $n$ . At  $n=4$ , for example, only three impulses are contributing to the overall output. To make matters worse, this problem is repeated five more times at a discrete-time period near the system's natural period. This phenomenon induces a vibration into the system that is caused solely by the application of the input shaping method to a system with time varying parameters.

This induced vibration is also present when the value of  $deln$  decreases. Consider a four impulse output, shaping scheme that is applied to a system that causes a change in  $deln$  from five to four. The resulting steady-state impulse output is shown in Figure 3.16. For this situation, a surplus of output impulses is generated at a discrete-time period near the system's natural period. These extra impulses also cause a vibration that is produced by the input shaping method.

To eliminate the induced vibration, a modified command shaping method is proposed to make the impulse output more uniform when a change in  $deln$  is encountered. To compensate for a change in the discrete-time period, extra impulses are added for an increase in  $deln$  and impulses are removed for a decrease in  $deln$ . The choice of which impulses are affected is based on the number of output impulses from the shaping algorithm and the old and new values of the discrete-time period.

The modified command shaping method can be explained by designating the discrete-time value when the discrete period increases as  $n=0$ . For the next  $N-1$  samples of the input, i.e.  $0 \leq n \leq N-2$ , the modified command shaping technique shapes each

sample using both the old and new values of  $deln$  to create a smooth steady-state impulse output. Using the new value of  $deln$ , the input sample is shaped to create  $N$  output impulses that are added to the overall output at their respective discrete-time values. Using the old value of  $deln$ , the same input sample is also shaped to create  $N$  output impulses. However, only the last  $N-(n+1)$  output impulses are added to the steady-state output at their respective discrete-time values. For discrete-time values of  $n \geq N-1$ , each sample of the input is shaped normally using the new value of  $deln$  to generate the  $N$  output impulses.

The modified command shaping method also works for a decrease in the discrete-time period,  $deln$ . For this situation, the input sample is shaped only once using the new value of  $deln$  to produce the four output impulses. Instead of adding all four of the output impulses, only the first  $(n+1)$  output impulses are added to the steady-state output at their respective discrete-time values. By manipulating the overall output in this way, the extra impulses that are added for the case when  $deln$  increases are the same impulses that are removed when  $deln$  decreases.

One final case to consider is when the value of  $deln$  changes more than once within one discrete-time period. For this situation, a new modified technique must be devised. For instance, if the discrete-time period length changes from one value to another and back again, the best method to smooth the steady-state output may be to ignore the change in discrete period if it is relatively short.

To understand the modified command shaping procedure, consider the example given in Figure 3.15. The value of  $deln$  increases from four to five for this input

shaping scheme that produces four output impulses. Since  $N=4$  for this case, the next three (i.e.  $N-1$ ) input samples will be shaped twice. At discrete-time  $n=0$ , the input sample is shaped using the new value of  $deln$  (i.e. 5) to create four (i.e.  $N$ ) output impulses that are added to the overall output. At the same discrete-time value, the input sample is shaped using the old value of  $deln$  (i.e. 4) to create four (i.e.  $N$ ) output impulses. However, only the last three (i.e.  $N-(n+1)$ ) impulses are added to the overall output at their respective discrete-time values. For the next discrete-time value, i.e.  $n=1$ , the input sample is shaped using the new value of  $deln$  to create the usual four output impulses that are added to the overall output. When the input sample is shaped using the old value of  $deln$ , only the last two (i.e.  $N-(n+1)$ ) output impulses are added to the general output. This process of shaping the input samples twice is repeated until the discrete-time value,  $n$ , is greater than  $N-2$ . After  $n > N-2$ , the shaping continues normally using only the new value of  $deln$  to produce the output impulses.

This modified command shaping technique is demonstrated on the two examples discussed previously when the number of output impulses is four. Figure 3.17 shows the modified shaping technique implemented for the case when the discrete-time period increases from four to five. The impulses due to the modified command shaping technique are darkened to show emphasis only. Figure 3.18 shows the modified shaping technique applied to the case when the period decreases from five to four. The impulses that are created but not added are drawn in the figure without tails to distinguish them from the normal impulses. The success of this modified input shaping technique is discussed in Chapter V.

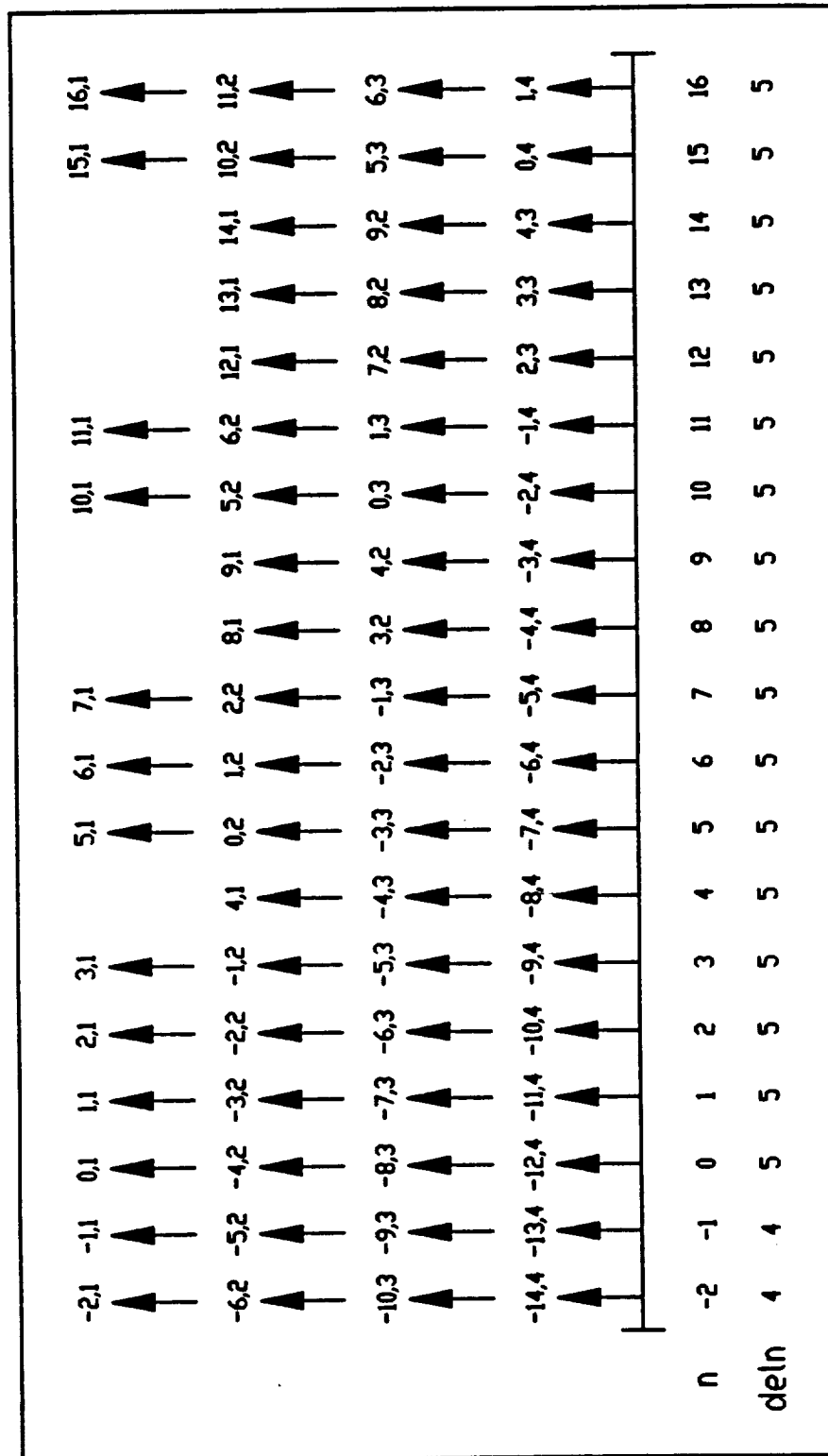
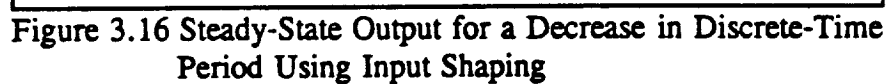


Figure 3.15 Steady-State Output for an Increase in Discrete-Time Period Using Input Shaping





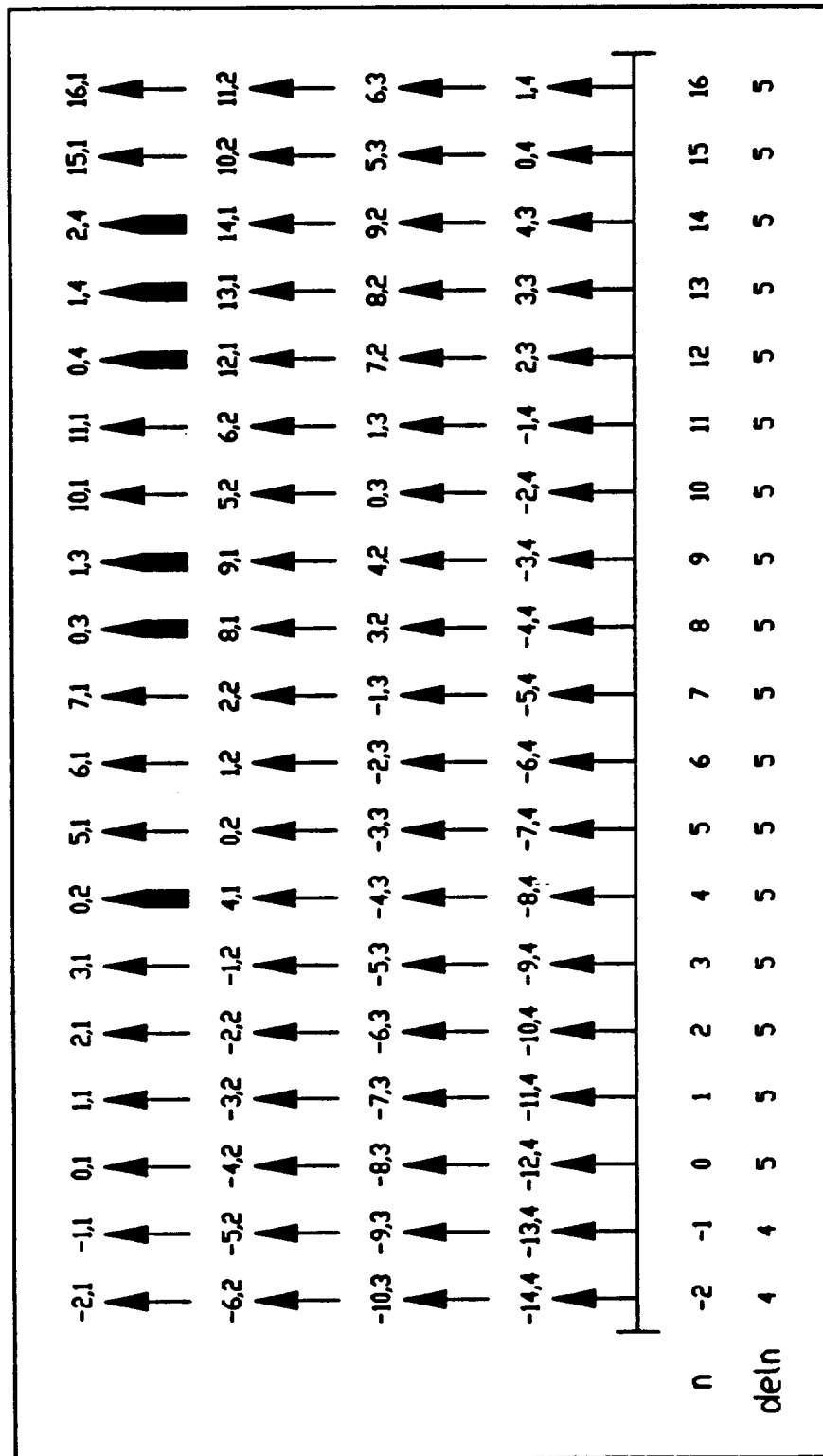
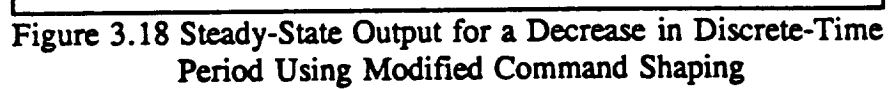


Figure 3.17 Steady-State Output for an Increase in Discrete-Time Period Using Modified Command Shaping



## **CHAPTER IV**

### **DYNAMIC ANALYSIS OF RALF**

#### **4.1 Previous Frequency Analysis**

The vibration analysis of RALF has been described by several investigators in the last five years. Huggins and Lee have performed the most research on verification of modeling methods and control algorithms for RALF. Huggins [19,20] conducted extensive finite element analysis to verify mathematical and experimental models used to determine the system modes and natural frequencies. Lee [26,27] derived a nonlinear model of RALF and then verified it through simulations using TREETOPS, a computer software package. However, these investigators only conducted research on a limited workspace of RALF. For a teleoperated system, the frequency data for the whole workspace is needed to implement the modified command shaping technique.

#### **4.2 Experimental Setup and Procedures**

The experimental determination of system resonances and damping ratios using digital Fourier analyzers is well published. Ramsey [36,37] discusses the importance of understanding the dynamic behavior of vibrating systems. Using Fourier analyzers, he explains many effective measurement techniques for modal analysis of different vibrating systems. The frequency response of a second-order system determined from several

different test inputs is also presented and the trade-offs for each method is discussed.

Hewlett-Packard has published many application notes about using their Digital Signal Analyzer (HP3562A) for modal analysis [3,4,5]. After reviewing these documents, random noise was chosen as the input to determine the desired system properties. Using the P.D. feedback control algorithm running on a MicroVAX to hold RALF in a desired joint configuration, the random noise signal from the analyzer was added to the control signal to stimulate the system. The system was excited at the control level instead of using an external shaker to include actuator dynamics that might influence the results. The circuit that combined the two signals is shown in Appendix K for reference. An accelerometer, mounted at the tip of RALF, measured the transverse acceleration of the second link which was then recorded by the analyzer.

For a given joint configuration, the power spectrum of the acceleration signal was averaged ten times to minimize noise effects. For the power spectrum, the analyzer can generate a second-order approximation for the pair of poles that correspond to the mode of vibration of the system. The poles are presented in the form

$$s = D \pm j f \quad \text{Hz.} \quad (4.1)$$

From control theory, a pair of complex poles can be expressed as

$$s = -\zeta f_n \pm j f_n \sqrt{1 - \zeta^2} \quad \text{Hz} \quad (4.2)$$

when  $0 \leq \zeta \leq 1$ .

Comparing Equations (4.1) and (4.2), the natural frequency,  $f_n$ , and damping ratio,  $\zeta$ , can be solved from the analyzer output by

$$f_n = \sqrt{f^2 + D^2} \quad (4.3)$$

$$\zeta = \sqrt{\frac{D^2}{f^2 + D^2}}. \quad (4.4)$$

Notice that the analyzer output value  $f$  is the damped natural frequency. This value is actually of more use in this form when the modified command shaping technique is implemented in the controller.

To obtain the desired frequency data, the workspace of RALF was divided up into ten degree joint increments and the power spectrum of the acceleration was taken at each location. Using Equations (4.3) and (4.4), the natural frequency and damping ratio of the first mode of vibration were calculated from the power spectrum output of the analyzer.

### 4.3 Modal Analysis Results

The fundamental damped natural frequencies calculated from the analyzer as a function of RALF's joint coordinates are presented in Table 4.1. The fundamental natural frequencies of RALF were also calculated and are given in Table 4.2. Finally, the damping ratios were calculated from the analyzer output and are in Table 4.3.

Table 4.1 Fundamental Damped Natural Frequencies vs. Joint Coordinates

$f_d$ (Hz)	$\theta_2$ (deg)						
$\theta_1$ (deg)		60	70	80	90	100	107
	40	5.17	5.2	5.17	5.19	5.46	5.15
	50	4.92	4.99	4.98	4.87	5.37	5.24
	60	4.75	4.77	4.84	4.86	4.99	5.27
	70	4.27	4.26	4.32	4.28	4.33	4.4
	80	3.79	4.12	4.11	4.39	4.37	4.27
	90	4.23	4.29	4.4	4.45	4.51	4.44
	100	3.98	4.07	4.14	4.25	4.28	4.33
	109	3.7	3.8	3.92	3.97	4.11	4.07

Table 4.2 Fundamental Natural Frequencies vs. Joint Coordinates

$f_n$ (Hz)	$\theta_2$ (deg)						
$\theta_1$ (deg)		60	70	80	90	100	107
	40	5.19	5.21	5.18	5.21	5.47	5.18
	50	4.94	5.01	5.01	4.9	5.37	5.24
	60	4.76	4.78	4.85	4.88	5.01	5.34
	70	4.29	4.29	4.34	4.30	4.35	4.42
	80	3.8	4.13	4.12	4.4	4.38	4.28
	90	4.25	4.3	4.41	4.47	4.52	4.45
	100	4.0	4.09	4.16	4.27	4.3	4.35
	109	3.73	3.83	3.95	3.99	4.13	4.12

Table 4.3 Damping Ratios vs. Joint Coordinates

$\zeta$	$\theta_2$ (deg)						
$\theta_1$ (deg)		60	70	80	90	100	107
	40	0.083	0.071	0.061	0.085	0.049	0.107
	50	0.084	0.086	0.116	0.116	0.026	0.027
	60	0.076	0.076	0.072	0.079	0.084	0.166
	70	0.105	0.110	0.093	0.102	0.091	0.099
	80	0.085	0.083	0.082	0.076	0.071	0.065
	90	0.093	0.084	0.078	0.083	0.062	0.063
	100	0.108	0.098	0.094	0.086	0.087	0.092
	109	0.121	0.129	0.113	0.109	0.102	0.149

#### 4.4 Curve Fitting of Experimental Data

The damped natural frequency and damping ratio data is not useful for control purposes in tabular form. A look-up table to find needed values in a control algorithm can demand lots of precious computation time which slows down the sampling rate of the control system. Therefore, the data was curve fitted to shorten the computation time and permit a faster sampling rate. Appendix L discusses the least-squares curve fit of the experimental data.

The polynomial regressions that were derived for the damped natural frequency and damping ratio are

$$f_d(\theta_1, \theta_2) = -0.4212\theta_2^3 + 1.8086\theta_2^2 - 2.1441\theta_2 - 0.2229\theta_1^3 + 1.4540\theta_1^2 - 3.6392\theta_1 + 7.7830 \quad (4.5)$$

$$\zeta(\theta_1, \theta_2) = -0.4269\theta_2^3 + 1.8918\theta_2^2 - 2.7159\theta_2 - 0.0533\theta_1^3 + 0.3410\theta_1^2 - 0.6148\theta_1 + 1.6762. \quad (4.6)$$

To determine how well the equations approximated the experimental data, Equations (4.5) and (4.6) were evaluated at all of the joint positions. Each calculated value of the damped natural frequency,  $f_c$ , was then divided by the experimental value of the damped natural frequency,  $f_d$ , at the corresponding joint angles to create a normalized frequency,  $f_c/f_d$ . The normalized frequencies as a function of joint coordinates is shown in Table 4.4. Using this normalized frequency, the correct number of impulses can be chosen based on the robustness criteria in Chapter III.

However, the damping ratio normalization generates the most error and is actually the determining factor for the number of impulses. Table 4.5 displays the normalized damping ratios,  $\zeta_c/\zeta$ , versus joint coordinates. This normalized data is very random in appearance which is a direct result of the way the analyzer linearly approximates the damping ratio. Using the largest normalized ratio of 4.5, Figure 3.13 suggests that the modified command shaping method should output four impulses to reduce vibration.



Table 4.4 Normalized Frequencies vs. Joint Coordinates

$f_c/f_d$	$\theta_2$ (deg)						
$\theta_1$ (deg)		60	70	80	90	100	107
	40	0.992	0.998	1.02	1.03	0.990	1.06
	50	0.980	0.980	0.994	1.03	0.949	0.978
	60	0.961	0.969	0.970	0.982	0.970	0.924
	70	1.02	1.04	1.04	1.07	1.07	1.06
	80	1.10	1.03	1.05	1.00	1.02	1.05
	90	0.956	0.956	0.949	0.956	0.958	0.978
	100	0.988	0.980	0.981	0.974	0.982	0.978
	109	1.04	1.03	1.01	1.02	1.00	1.02

Table 4.5 Normalized Damping Ratios vs. Joint Coordinates

$\zeta_c/\zeta$	$\theta_2$ (deg)						
$\theta_1$ (deg)		60	70	80	90	100	107
	40	1.63	1.73	2.12	1.68	0.30	1.32
	50	1.24	1.06	0.846	0.959	4.49	4.13
	60	1.12	0.948	1.10	1.164	1.16	0.547
	70	0.734	0.582	0.764	0.825	1.00	0.831
	80	0.917	0.783	0.870	1.12	1.28	1.29
	90	0.921	0.865	1.01	1.11	1.58	1.45
	100	0.913	0.875	0.980	1.23	1.29	1.13
	109	0.940	0.781	0.952	1.11	1.24	0.800

Now that the number of output impulses has been determined, the modified command shaping technique can be implemented to reduce vibration. The modified shaping method takes each input sample and replaces it with four output impulses that do not excite the first natural frequency of RALF. The required values of damped natural frequency and damping ratio needed to calculate the impulse amplitudes and their starting times are found from Equations (4.5) and (4.6).

## **CHAPTER V**

### **CONTROL IMPLEMENTATION AND RESULTS**

#### **5.1 Control Structure**

The original input shaping method devised by Singer was entirely feedforward in design [38]. The desired (x,y) coordinate positions were transformed into desired joint angles using a Jacobian before applying the input shaping algorithm. This feedforward scheme provides little robustness to noise disturbances or to model uncertainty. To overcome these problems, Hillsley and Yurkovich [18] applied a composite control strategy which utilizes input shaping with a feedback scheme.

The control design for RALF uses an adaptive; proportional plus derivative (P.D.) feedback strategy derived by Yuan [49] with the addition of modified command shaping. Yuan's control algorithm was chosen because it compensates for unmodeled modes and nonlinearities of the system. The modified command shaping technique is designed to eliminate the first natural frequency of RALF discussed in Chapter IV. The block diagram of the comprehensive control system is shown in Figure 5.1. Since the input to the control system is desired angles, it is easily implemented with the master arm which allows the user to specify a desired end-position while it records desired joint angles. This control implementation also allows other pre-computed trajectories to be input into the system for means of comparison.

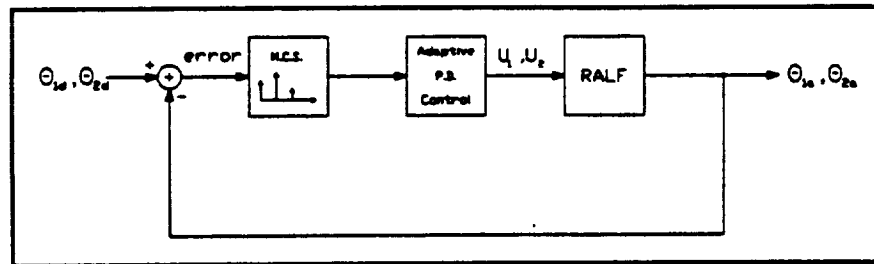


Figure 5.1 Block Diagram of Control System

## 5.2 Input Trajectories

To demonstrate the reduction in tip vibration, the modified command shaping technique is compared to the original P.D. controller for different input trajectories. For these comparisons, the trajectories are pre-computed to ensure an equivalent basis for comparing vibration reduction. The principal trajectory is a three-foot diameter circle located above the first axis with a completion time of nine seconds. Figure 5.2 shows the location of the circle relative to the workspace of RALF. This location was chosen because there is a large enough variation in system natural frequency to change the discrete-time period,  $deln$ . A sinusoidal perturbation signal with variable frequency is then added to the radius parameter of the circle to induce vibration into the system.

The vibration of the tip is recorded using two different methods. The first method is very similar to the way the frequency data was obtained in Chapter IV. The robot is commanded to follow the desired circle trajectory eight times which eliminates noise effects and allows reliable averaging of the data. The analyzer records the transverse acceleration response at the tip and computes the power spectrum of the data. The magnitude of the frequency response is the root-mean-square of the acceleration and

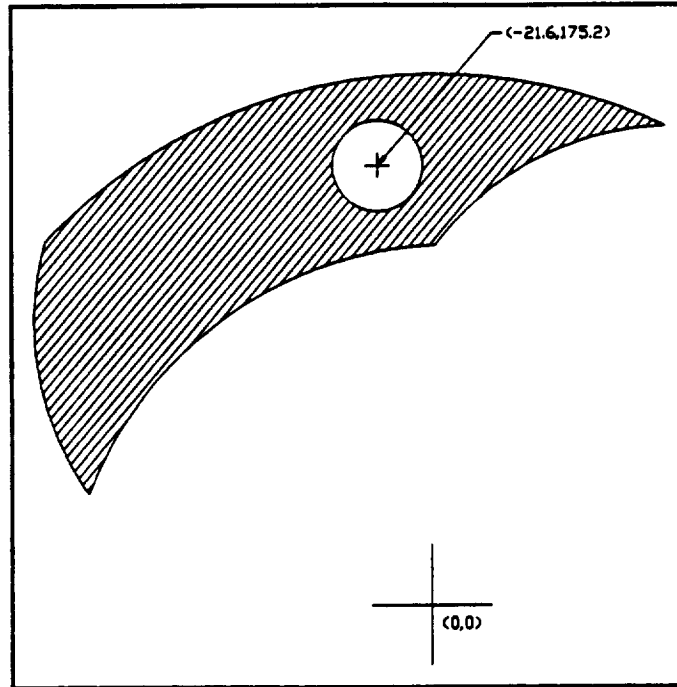


Figure 5.2 Principal Circle Trajectory

is displayed in units of decibels (dB). Recall the definition of decibels is

$$\text{number of decibels} = 10 \log_{10} A \quad (5.1)$$

where  $A$  is the amplitude in question. The frequency response for each control strategy is then compared to determine which controller has the smaller amplitude of vibration.

The second method is a visual approach to examine the tip vibration of the robot. A light-emitting diode (LED) is attached to the end-point of RALF and then one revolution of the desired circle trajectory is commanded. By leaving the aperture on a 35 mm camera open, the actual end-point path is recorded. Of course, special measures

are made to ensure that the LED is the only light source imprinted on the negative. At the end of the trajectory, the flash is triggered to reveal the robot configuration.

### 5.2.1 Trajectory One - Circle With No Perturbation

The first trajectory is the principal circle with no perturbation added. Figure 5.3 shows a comparison of the frequency response between the P.D. control and Singer's original input shaping substituted for the modified command shaping. The magnitude of the frequency response for the input shaping method is greater than that for the P.D. routine.

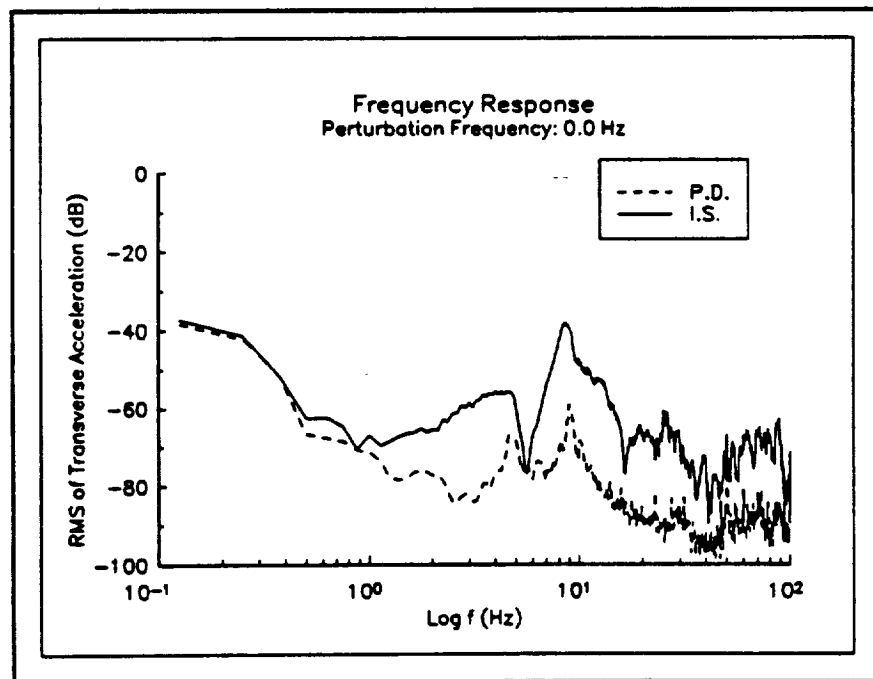


Figure 5.3 Frequency Response of RALF  
P.D. vs. Input Shaping  
No Perturbation

The increase in magnitude of the frequency response for the input shaping method at the 4.8 Hz frequency value denotes a vibration of the system at the first natural frequency. This vibration is provoked by the inability of the input shaping to handle varying system parameters. The sharp peak in the frequency response at the 10 Hz frequency value is the second natural frequency. However, the modified command shaping technique is only designed to reduce the vibration at the first natural frequency.

The induced vibration caused by the input shaping method can be seen visually in Figure 5.6. The path followed by the end-point using the ordinary P.D. controller is shown in Figure 5.5. The actual path followed by the end-point of RALF is not a precise circle because the P.D. controller does not drive the steady state joint error to zero.

By implementing the modified command shaping technique, the induced vibration is eliminated. This result is evident in the frequency response of Figure 5.4 and the picture given in Figure 5.7. From Figure 5.4, the magnitude is reduced by 20 dB at the system natural frequency of 4.8 Hz. This results in a vibration that is only 1% of the amplitude of the original P.D. vibration for this specific frequency. Comparing Figure 5.5 and Figure 5.7, the modified command shaping technique generates almost the same tip motion as the P.D. controller even though the 4.8 Hz frequency component is missing.

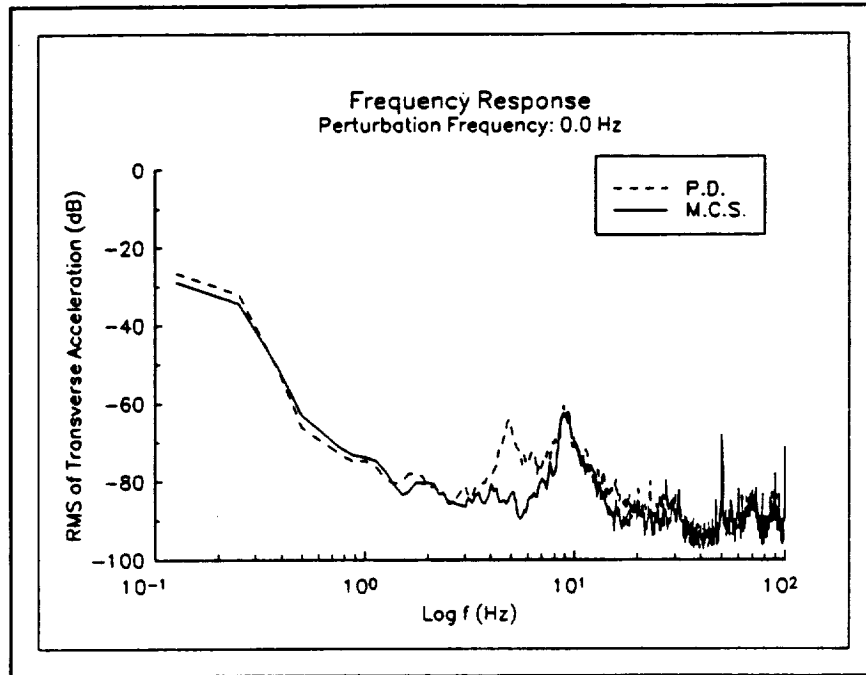


Figure 5.4 Frequency Response of RALF  
P.D. vs. Modified Command Shaping  
No Perturbation

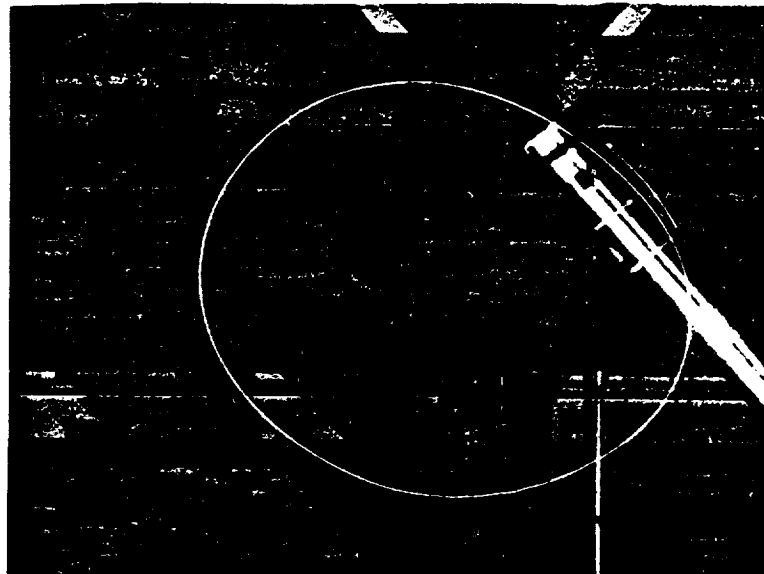


Figure 5.5 Picture of Tip Motion Using P.D. Control  
No Perturbation



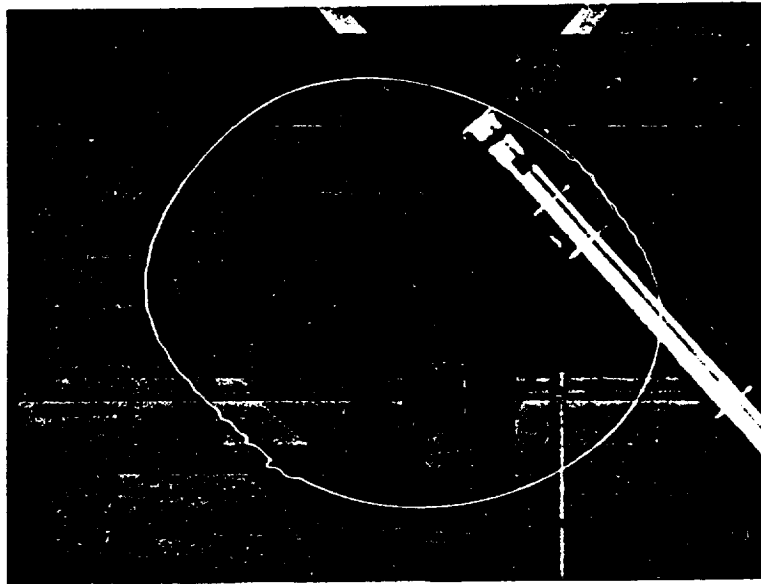


Figure 5.6 Picture of Tip Motion Using Input Shaping  
No Perturbation

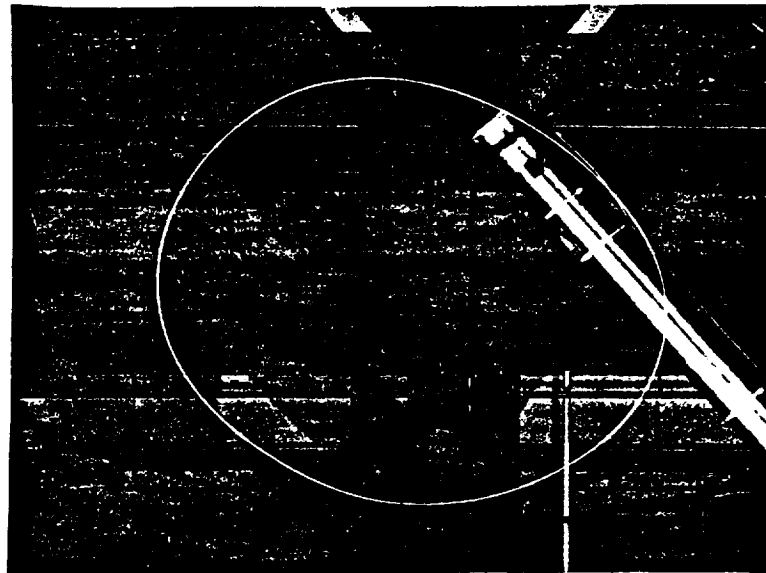


Figure 5.7 Picture of Tip Motion Using Modified  
Command Shaping - No Perturbation

### 5.2.2 Trajectory Two - Circle With 1 Hz Perturbation

This trajectory, shown in Figure 5.8, is the principal circle with a 1 Hz sine wave with an amplitude of 1.5" riding on the radial component of the circle. This trajectory

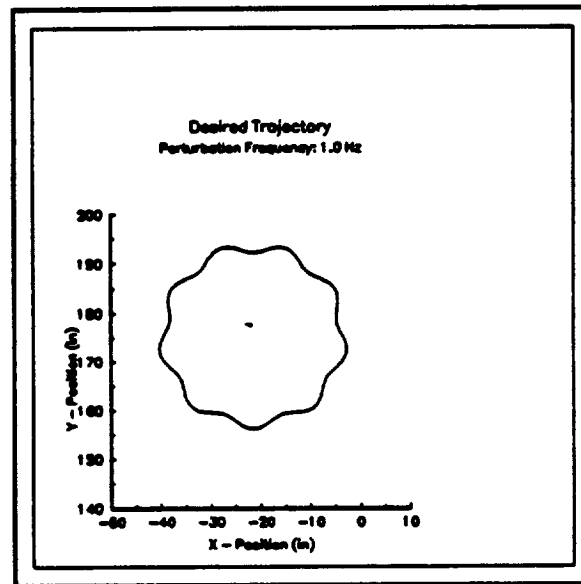


Figure 5.8 Circle Trajectory with 1 Hz Perturbation

should contain nine "bumps" around the circle since the period is nine seconds. The frequency response of the modified command shaping versus the P.D. control is shown in Figure 5.9. Since the command shaping technique was not designed to eliminate 1 Hz vibration, the two control schemes show comparable results for this frequency range. However, the modified command shaping reduced the magnitude of vibration by 18 dB at the system natural frequency value of 4.8 Hz. This results in a vibration that is 1.6% of the amplitude of the original P.D. vibration at this particular frequency.

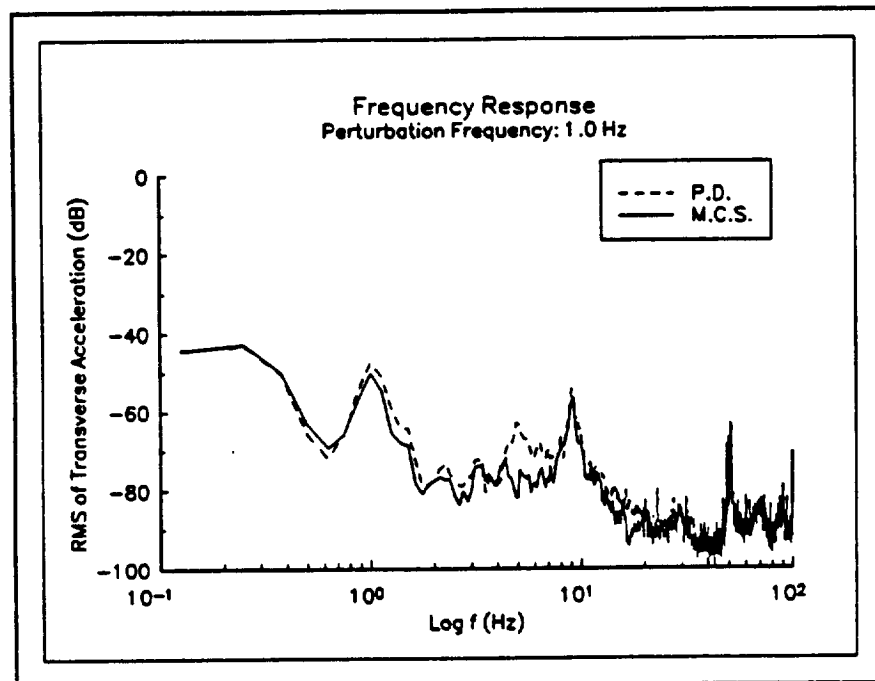


Figure 5.9 Frequency Response of RALF  
P.D. vs. Modified Command Shaping  
1 Hz Perturbation

### 5.2.3 Trajectory Three - Circle With 4.8 Hz Perturbation

The purpose of this trajectory, given in Figure 5.10, is to excite the first natural frequency of the system. Figure 5.11 displays the frequency response comparison for this trajectory. The difference in magnitude is 32 dB at the system natural frequency of 4.8 Hz which corresponds to 0.06% of the original P.D. vibration amplitude for this particular frequency. The visual effects are even more impressive. Figure 5.12 shows the tip motion for the P.D. control effort while Figure 5.13 displays the tip motion for the modified command shaping. At least visually, the modified command shaping method appears to completely eliminate the vibration.

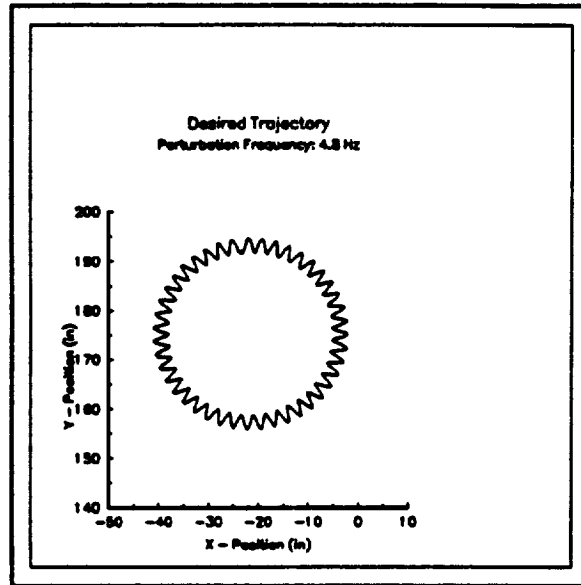


Figure 5.10 Circle Trajectory with 4.8 Hz Perturbation

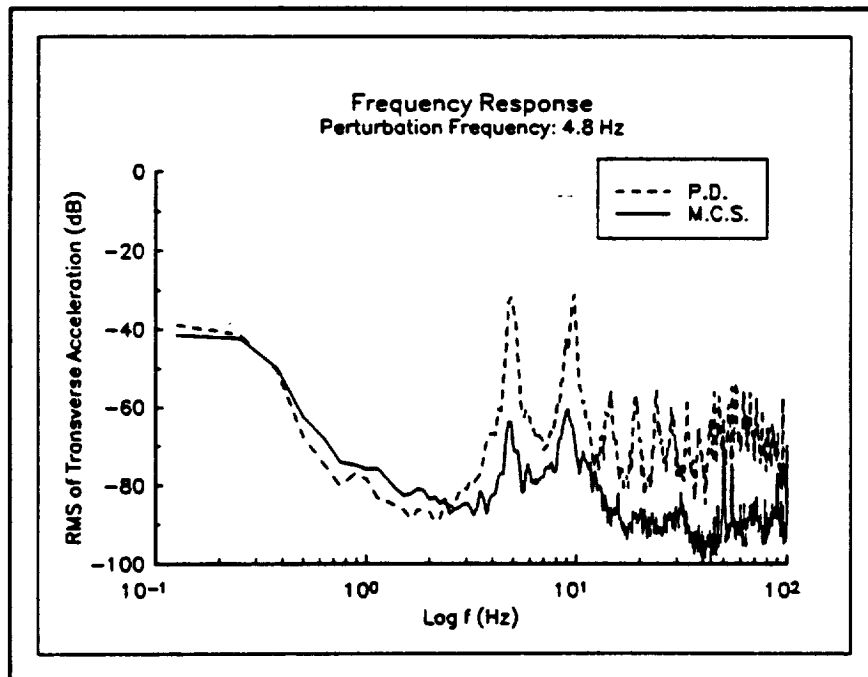


Figure 5.11 Frequency Response of RALF  
P.D. vs. Modified Command Shaping  
4.8 Hz Perturbation

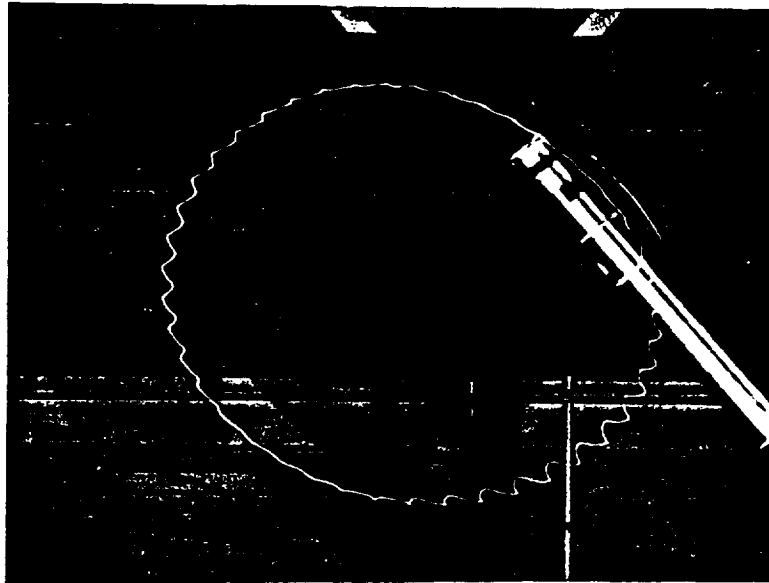


Figure 5.12 Picture of Tip Motion Using P.D. Control  
4.8 Hz Perturbation

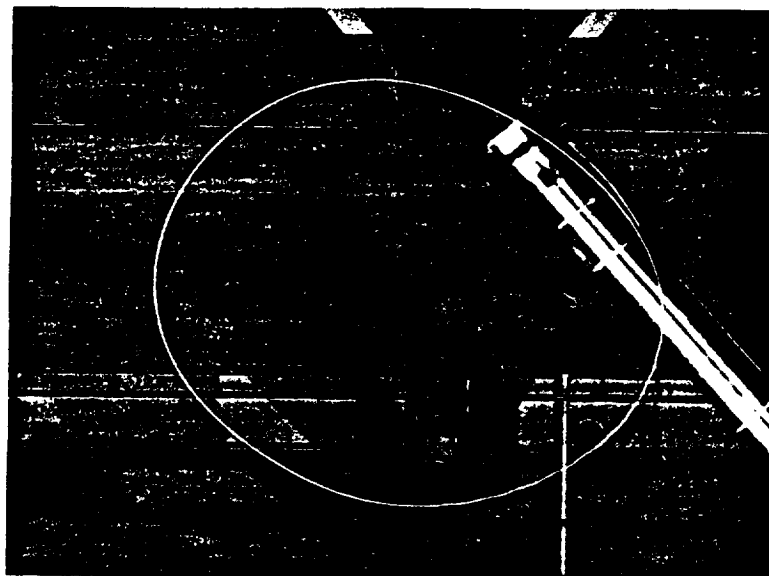


Figure 5.13 Picture of Tip Motion Using Modified  
Command Shaping - 4.8 Hz Perturbation

#### 5.2.4 Trajectory Four - Circle with 10 Hz Perturbation

The final circle trajectory, displayed in Figure 5.14, demonstrates the ability of the modified method to reduce system frequency vibration for input signals that contain higher frequency components. Figure 5.15 shows a reduction in magnitude at the

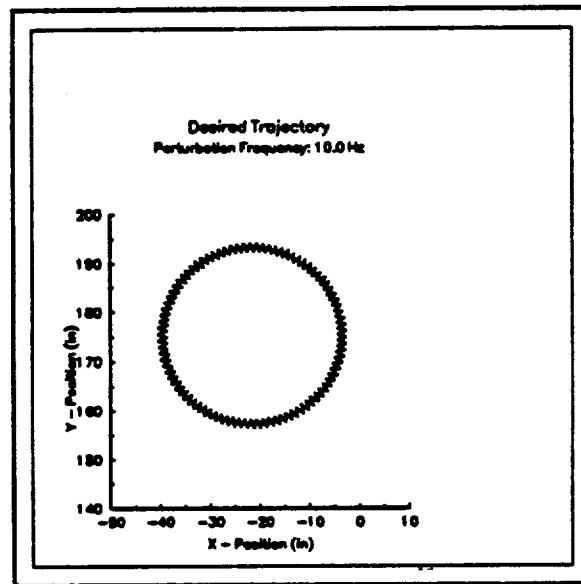


Figure 5.14 Circle Trajectory with 10 Hz Perturbation

4.8 Hz frequency location of 9 dB. This results in a vibration that is 12.6% of the amplitude of the original P.D. vibration for this particular frequency.

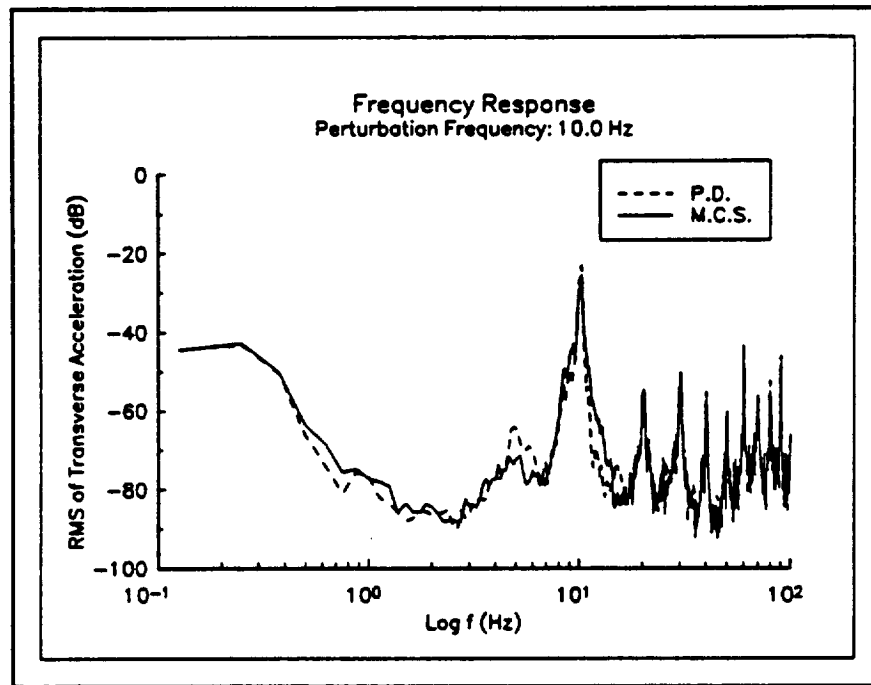


Figure 5.15 Frequency Response of RALF  
P.D. vs. Modified Command Shaping  
10 Hz Perturbation

### 5.2.5 Trajectory Five - Pseudo-Step

A step input is often given as a test input because it theoretically contains all the frequency components. To simulate a step, a cycloidal motion in joint space was created with a duration time of 0.2 seconds [30]. Using this pseudo-step input, a ten degree step was simultaneously given to each joint and a time record was taken of the transverse acceleration response at the tip. Figure 5.16 shows the desired tip motion with the starting position at (-4.7,142.9) and Figure 5.17 displays the transverse acceleration response. Clearly, the amplitude of the time response for the pseudo-step input is reduced using the modified method. However, notice the delay in the modified command

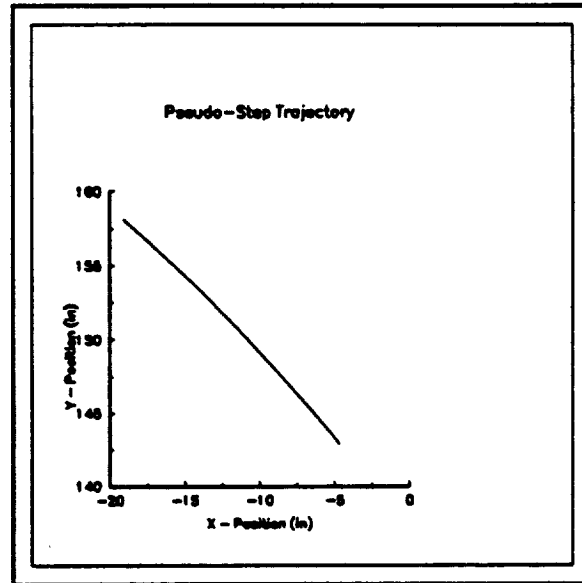


Figure 5.16 Pseudo-Step Trajectory

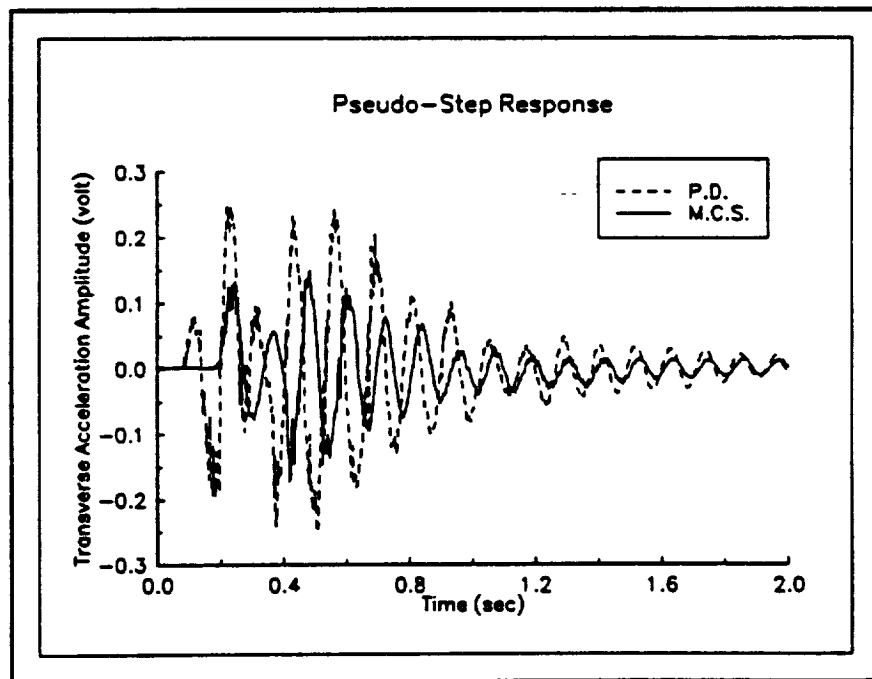


Figure 5.17 Pseudo-Step Response of RALF  
P.D. vs. Modified Command Shaping



shaping method's pseudo-step response. This delay is present because the pseudo-step trajectory holds the robot in the starting joint configuration for ten clock cycles. Since the sampling rate is 50 Hz, this time delay is 0.2 seconds. Although the robot is supposed to remain stationary during the hold time, a slight error signal is developed in the control algorithm which causes the robot to move. This tip motion is large enough for the amplitude of the transverse acceleration to trigger the analyzer. This slight tip motion is verified in the Figure 5.18. When the modified command shaping method is implemented, the amplitude of the small error signal is reduced so that the transverse acceleration is not large enough to trigger the analyzer. Therefore, the delay experienced by the modified command shaping method is actually the hold time of the pseudo-step trajectory.

Figures 5.18 and 5.19 show the pseudo-step responses for each of the control schemes. The slight tip motion during the hold portion of the trajectory is very evident and is even more pronounced in the modified command shaping technique case. The reduction in vibration of the modified command shaping method is apparent from the smoothness of the trajectory. However, the tip position overshoots the desired final position. The feedback nature of the control structure together with an underdamped system is believed to generate this undesirable overshoot. Had the method been implemented in a feedforward manner as Singer did, this overshoot might be eliminated.

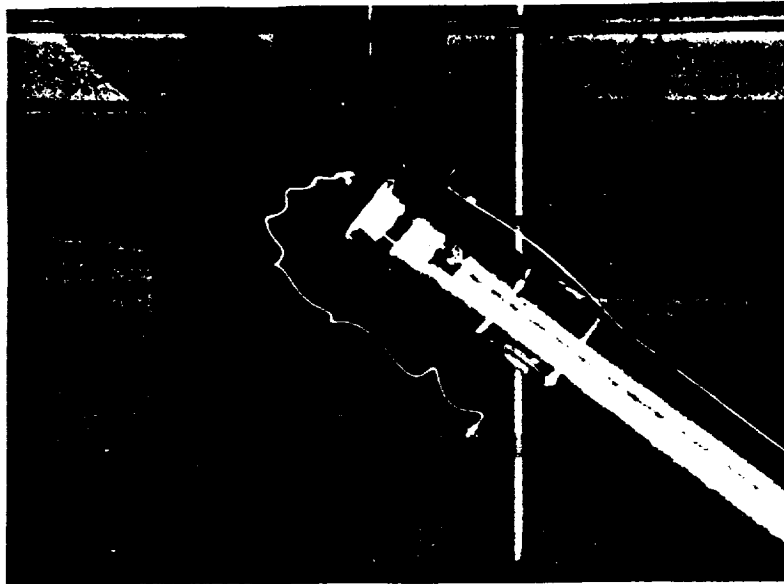


Figure 5.18 Picture of Tip Motion Using P.D. Control Pseudo-Step Input

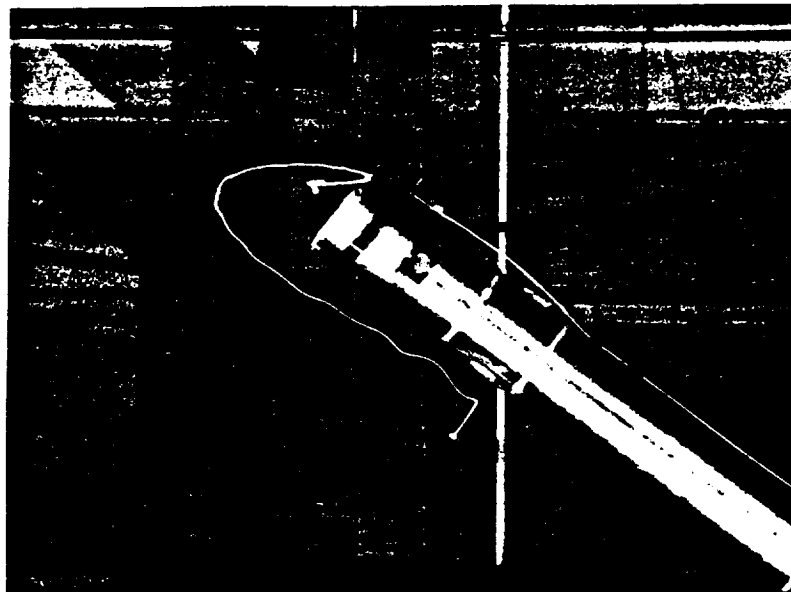


Figure 5.19 Picture of Tip Motion Using Modified Command Shaping - Pseudo-Step Input

## **CHAPTER VI**

### **CONCLUSIONS**

#### **6.1 Summary**

Singer's original input shaping idea was introduced and explained using the equation of motion for a simple second-order system. The constraint equations needed to yield a vibrationless system were discussed and then multiple impulse amplitudes were derived for several constraint conditions. A vibration error expression was derived based on the ratio of the multiple impulse response to the impulse response of a second-order system. The residual vibration for each case was graphed to determine the effects of deviation in system parameters. The input shaping method was shown to actually increase the residual vibration in certain situations when the system parameters are not accurately specified.

The main intention of this research was to reduce end-point vibration in a teleoperated system while preserving the usefulness of the system motion. Results verified that the input shaping method can actually induce vibration in systems that have varying parameters. Therefore, a modified command shaping technique was developed to alleviate this problem. By varying input perturbations to trajectories in a range of possible user inputs, the modified command shaping technique proved to reduce vibration at the system's first natural frequency. The reduction in amplitude varied from 87.4%

for the high frequency perturbation to 99.94% for a perturbation frequency near the system resonance. The acceleration response of the command shaping to a pseudo-step input was smaller in amplitude than the regular P.D. control. However, the pseudo-step response of command shaping displayed overshoot which may be undesirable in many end-point positioning tasks.

## **6.2 Contributions**

The major contributions of this research are the implementation of teleoperation on RALF, the new perspective of residual vibration, the visualization of tip motion and the derivation of a modified command shaping technique.

The implementation of teleoperation on RALF allows users to specify any end-point trajectory within the workspace. The ability to perform teleoperated experiments such as cutting and end-point bracing are now possible.

The new definition for residual vibration gives a clearer representation of the input shaping method. It demonstrates that the input shaping method may not be effective in reducing residual vibration in all cases.

The visualization method for viewing tip motion using a LED permits easy evaluation of tip vibration. The method can also estimate the ability of a system to follow desired tip trajectories.

Finally, the modified command shaping technique expands the use of the original input shaping idea to systems with varying parameters. The induced vibration caused when the input shaping method is applied to a variable frequency system is eliminated

by the command shaping method. By realizing a change in the discrete-time period, the impulse input is modified to eliminate the possibility of producing the vibration.

### **6.3 Future Work**

The main concern to be addressed in future research is the elimination of overshoot in the step response of RALF. To have an effective teleoperated system, the end-point must be positioned without overshoot. This could be accomplished using the modified command shaping technique in a feedforward arrangement that is combined with a feedback control scheme. Another possibility is the implementation of inverse dynamics with the modified method to accurately position the end-point of RALF.

The second goal is to implement the modified method to eliminate the second natural frequency of RALF. This would require a faster control system than the MicroVAX can provide. By using a PC, faster computation and A/D rates are possible and the elimination of the first two natural frequencies could be achieved.

Finally, the effects of the modified command shaping technique on the stability of the overall control structure will be investigated. The time delays produced by this shaping method must be better understood to develop a control scheme that has accurate end-point tracking capabilities without overshoot.

## **APPENDIX A**

### **RIGID BODY TRANSFORMATIONS FOR RALF**

Forward kinematics of rigid bodies is used to determine the position and orientation of the end-effector on a manipulator. Inverse kinematics, on the other hand, deals with the problem of finding all the possible joint configurations given the end-effector position and orientation. Questions often arise with the uniqueness of a given solution, or even if one exists, with the inverse case.

By using matrix transformations, kinematic equations relating the end-point of a manipulator to its base can be derived. The process involves representing each degree of freedom of a manipulator with an individual coordinate system. Each matrix transformation relates one coordinate system to the previous one. The overall matrix transformation from the end-point to the base of a robot is obtained by multiplying all of the matrix transformations in the proper order. Most robotic texts give a thorough discussion of matrix transformations [11,44].

Although RALF is not a rigid body, the forward and inverse kinematics can be derived to give an approximate solution for the end-point location and orientation or the joint configurations. Consider Figure A.1 which shows the rigid body coordinate systems used for RALF.

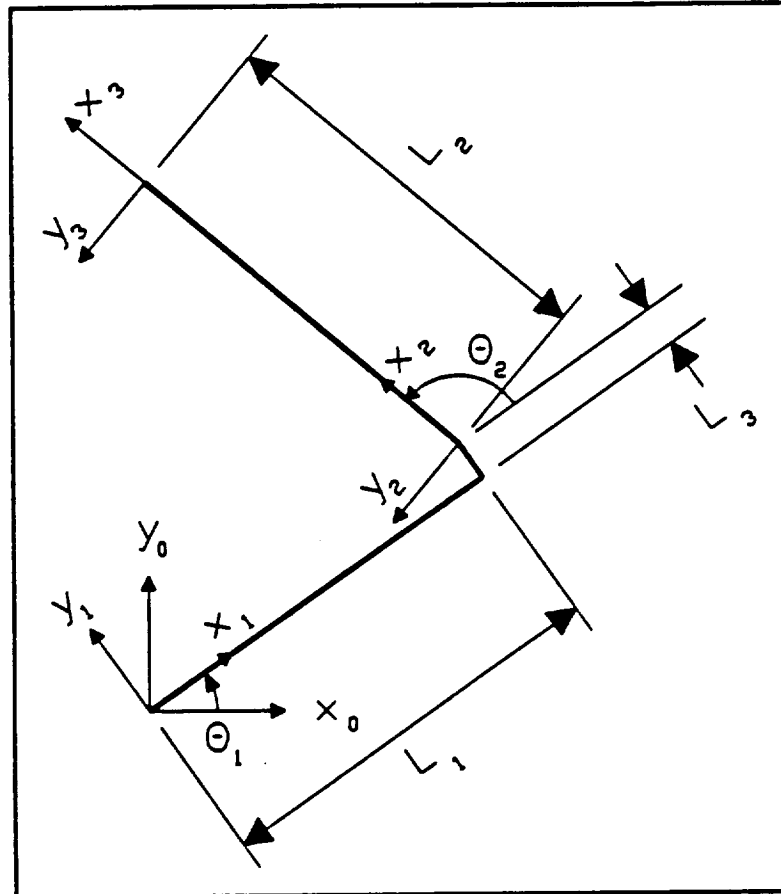


Figure A.1 Rigid Body Coordinate Systems for RALF

The matrix transformations relating each frame are

$${}^0_1T = \begin{bmatrix} \cos(\theta_1) & -\sin(\theta_1) & 0 & 0 \\ \sin(\theta_1) & \cos(\theta_1) & 0 & 0 \\ 0 & 0 & 1 & 0 \\ 0 & 0 & 0 & 1 \end{bmatrix} \quad (A.1)$$

$${}^1_2T = \begin{bmatrix} \cos(\theta_2) & -\sin(\theta_2) & 0 & L_1 \\ \sin(\theta_2) & \cos(\theta_2) & 0 & L_3 \\ 0 & 0 & 1 & 0 \\ 0 & 0 & 0 & 1 \end{bmatrix} \quad (\text{A.2})$$

$${}^2_3T = \begin{bmatrix} 1 & 0 & 0 & L_2 \\ 0 & 1 & 0 & 0 \\ 0 & 0 & 1 & 0 \\ 0 & 0 & 0 & 1 \end{bmatrix}. \quad (\text{A.3})$$

The overall matrix transformation from the end-point to the base of RALF is found by multiplying the individual transformations as follows

$${}^0_3T = {}^0_1T {}^1_2T {}^2_3T. \quad (\text{A.4})$$

The resulting overall matrix transformation is

$${}^0_3T = \begin{bmatrix} \cos(\theta_1+\theta_2) & -\sin(\theta_1+\theta_2) & 0 & L_2 \cos(\theta_1+\theta_2) + L_1 \cos(\theta_1) - L_3 \sin(\theta_1) \\ \sin(\theta_1+\theta_2) & \cos(\theta_1+\theta_2) & 0 & L_2 \sin(\theta_1+\theta_2) + L_1 \sin(\theta_1) + L_3 \cos(\theta_1) \\ 0 & 0 & 1 & 0 \\ 0 & 0 & 0 & 1 \end{bmatrix}. \quad (\text{A.5})$$



Recall that the fourth column of the overall matrix transformation is the position vector.

Therefore, the (x,y) coordinates of the end-point are given in base coordinates by

$$x = L_2 \cos(\theta_1 + \theta_2) + L_1 \cos(\theta_1) - L_3 \sin(\theta_1) \quad (\text{A.6})$$

$$y = L_2 \sin(\theta_1 + \theta_2) + L_1 \sin(\theta_1) + L_3 \cos(\theta_1). \quad (\text{A.7})$$

Given the two joint angles, the (x,y) coordinates of the end-point can be calculated using Equations (A.6) and (A.7).

Now consider the inverse problem. Taking the sum of the squares of Equations (A.6) and (A.7) yields

$$x^2 + y^2 = L_1^2 + L_2^2 + L_3^2 + 2L_1L_2 \cos(\theta_2) + 2L_2L_3 \sin(\theta_2). \quad (\text{A.8})$$

Define K by

$$K = x^2 + y^2 - L_1^2 - L_2^2 - L_3^2 \quad (\text{A.9})$$

so that Equation (A.8) becomes

$$K = 2L_1L_2 \cos(\theta_2) + 2L_2L_3 \sin(\theta_2). \quad (\text{A.10})$$

Solving for  $\cos(\theta_2)$  from Equation (A.10) yields

$$\cos(\theta_2) = \frac{K - 2L_2L_3\sin(\theta_2)}{2L_1L_2}. \quad (\text{A.11})$$

Notice that Equation (A.11) can not be explicitly solved for  $\theta_2$ . But recall the trigonometric identity

$$\sin^2(\theta_2) + \cos^2(\theta_2) = 1. \quad (\text{A.12})$$

Squaring Equation (A.11)

$$\cos^2(\theta_2) = \frac{K^2 - 4KL_2L_3\sin(\theta_2) + 4L_2^2L_3^2\sin^2(\theta_2)}{4L_1^2L_2^2} \quad (\text{A.13})$$

and substituting into Equation (A.12) yields

$$\sin^2(\theta_2) = \frac{4L_1^2L_2^2 - K^2 + 4KL_2L_3\sin(\theta_2) - 4L_2^2L_3^2\sin^2(\theta_2)}{4L_1^2L_2^2}. \quad (\text{A.14})$$

Equation (A.14) can be simplified to

$$\sin(\theta_2) = \frac{KL_3 \pm L_1\sqrt{4L_2^2(L_1^2 + L_3^2) - K^2}}{2L_2(L_1^2 + L_3^2)}. \quad (\text{A.15})$$

Since  $\theta_2$  can not be less than zero, Equation (A.15) becomes

$$\sin(\theta_2) = \frac{KL_3 + L_1 \sqrt{4L_2^2(L_1^2 + L_3^2) - K^2}}{2L_2(L_1^2 + L_3^2)}. \quad (\text{A.16})$$

Substituting Equation (A.16) into Equation (A.11) produces

$$\cos(\theta_2) = \frac{KL_1 - L_3 \sqrt{4L_2^2(L_1^2 + L_3^2) - K^2}}{2L_2(L_1^2 + L_3^2)}. \quad (\text{A.17})$$

Using Equations (A.16) and (A.17), the solution for  $\theta_2$  becomes

$$\theta_2 = \text{atan2} \left( \frac{KL_3 + L_1 \sqrt{4L_2^2(L_1^2 + L_3^2) - K^2}}{KL_1 - L_3 \sqrt{4L_2^2(L_1^2 + L_3^2) - K^2}} \right). \quad (\text{A.18})$$

To solve for  $\theta_1$ , Equations (A.6) and (A.7) are expanded to produce

$$x = (L_2 \cos(\theta_2) + L_1) \cos(\theta_1) - (L_2 \sin(\theta_2) + L_3) \sin(\theta_1) \quad (\text{A.19})$$

$$y = (L_2 \sin(\theta_2) + L_3) \cos(\theta_1) + (L_2 \cos(\theta_2) + L_1) \sin(\theta_1). \quad (\text{A.20})$$

Equations (A.19) and (A.20) are solved for  $\sin(\theta_1)$  and  $\cos(\theta_1)$ , which are

$$\sin(\theta_1) = \frac{-x(L_2 \sin(\theta_2) + L_3) + y(L_2 \cos(\theta_2) + L_1)}{L_1^2 + L_2^2 + L_3^2 + 2L_2(L_1 \cos(\theta_2) + L_3 \sin(\theta_2))} \quad (\text{A.21})$$

$$\cos(\theta_1) = \frac{x(L_2 \cos(\theta_2) + L_1) + y(L_2 \sin(\theta_2) + L_3)}{L_1^2 + L_2^2 + L_3^2 + 2L_2(L_1 \cos(\theta_2) + L_3 \sin(\theta_2))}. \quad (\text{A.22})$$

Using Equations (A.21) and (A.22), the solution for  $\theta_1$  becomes

$$\theta_1 = \text{atan2} \left( \frac{-x(L_2 \sin(\theta_2) + L_3) + y(L_2 \cos(\theta_2) + L_1)}{x(L_2 \cos(\theta_2) + L_1) + y(L_2 \sin(\theta_2) + L_3)} \right). \quad (\text{A.23})$$

So, knowing the (x,y) position of the end-point of RALF, the joint coordinates can be computed using the following three equations:

$$K = x^2 + y^2 - L_1^2 - L_2^2 - L_3^2 \quad (\text{A.24})$$

$$\theta_2 = \text{atan2} \left( \frac{KL_3 + L_1 \sqrt{4L_2^2(L_1^2 + L_3^2) - K^2}}{KL_1 - L_3 \sqrt{4L_2^2(L_1^2 + L_3^2) - K^2}} \right) \quad (\text{A.25})$$

$$\theta_1 = \text{atan2} \left( \frac{-x(L_2 \sin(\theta_2) + L_3) + y(L_2 \cos(\theta_2) + L_1)}{x(L_2 \cos(\theta_2) + L_1) + y(L_2 \sin(\theta_2) + L_3)} \right). \quad (\text{A.26})$$

## **APPENDIX B**

### **DIMENSIONS OF MASTER ARM**

Figure B.1 shows the dimensions of the master arm used by the operator to input desired joint commands. Potentiometers, listed in Appendix C, are placed at each joint of the master arm to translate the joint commands input by the user into actual joint motions of RALF.

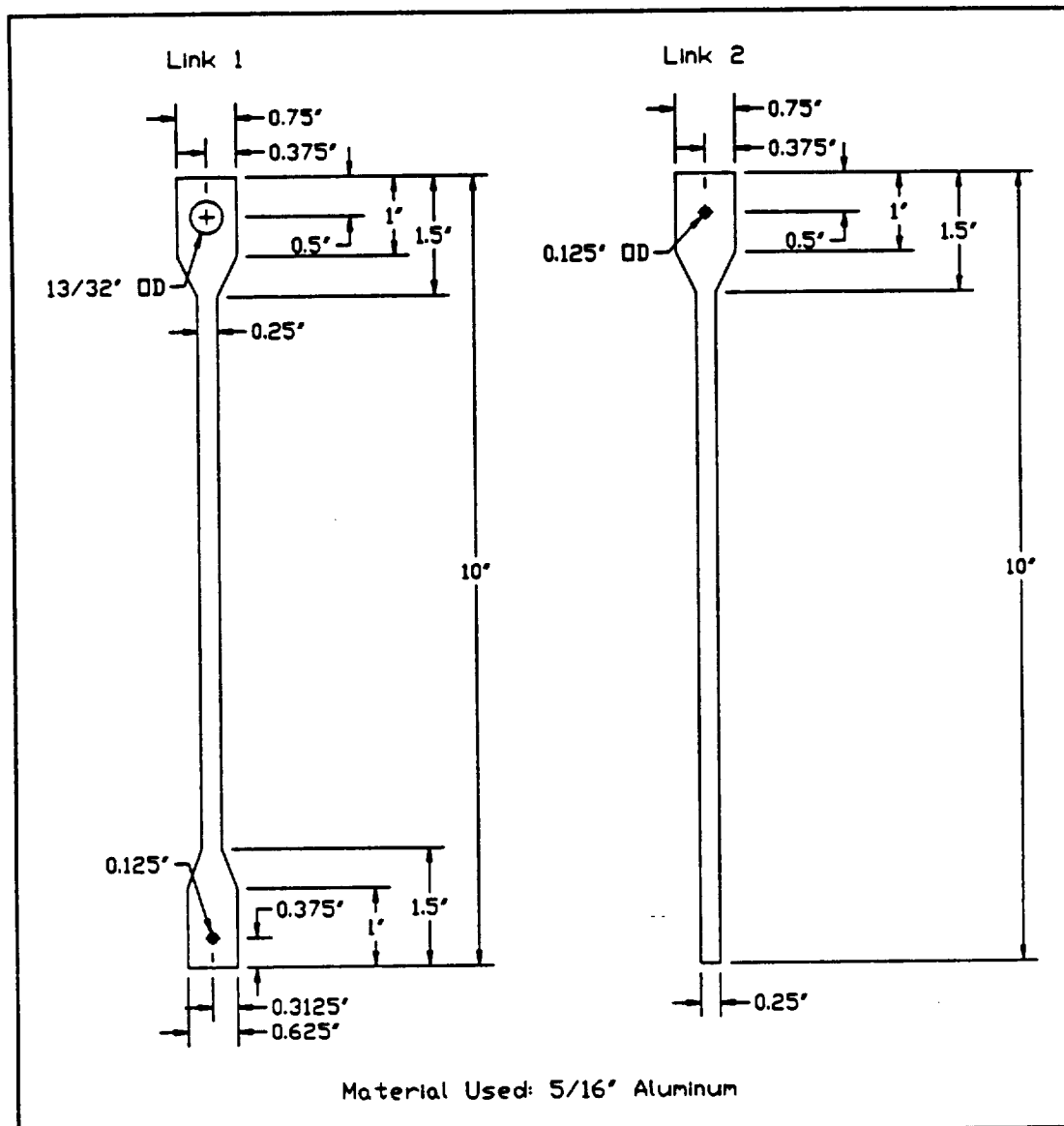


Figure B.1 Dimensions of Master Arm

## **APPENDIX C**

### **EQUIPMENT LIST**

#### **ELECTRONIC COMPONENTS**

Device: MicroVax II  
Model No.: VS21W-A2  
Serial No.: WF61305805  
Company: Digital Equipment Co.

Device: Real-Time Clock  
Model No.: DT2769  
Serial No.: 187824-C453  
Company: Data Translation

Device: Analog I/O System  
Model No.: DT2785  
Serial No.: 188872-C496  
Company: Data Translation

Device: Dynamic Signal Analyzer  
Model No.: HP3562A  
Serial No.: 2502A00718  
Company: Hewlett-Packard Co.

Device: Disk Storage Unit  
Model No.: HP9122D  
Serial No.: 2518A44227  
Company: Hewlett-Packard Co.

Device: Supply/Amplifier - Joint one of RALF  
Model No.: BOP36-1.5M  
Serial No.: F79808  
Company: KEPCO



Device: Supply/Amplifier - Joint two of RALF  
Model No.: BOP36-5M  
Serial No.: F105062  
Company: KEPCO

Device: Potentiometer - Joint one of Master  
Model No.: 6637  
Company: Bourns

Device: Potentiometer - Joint two of Master  
Model No.: 6637  
Company: Bourns

## **SENSORY COMPONENTS**

Device: LDT Position Sensing System - Joint one of RALF  
Model No.: 011020050100  
Serial No.: 20658-02-002P  
Company: MTS Systems Corp.

Device: LDT Position Sensing System - Joint two of RALF  
Model No.: 011020050100  
Serial No.: 20658-02-001P  
Company: MTS Systems Corp.

Device: Analog Output Module - Joint one of RALF  
Model No.: 0110200503105001  
Serial No.: 20658-05-001P  
Company: MTS Systems Corp.

Device: Analog Output Module - Joint two of RALF  
Model No.: 0110200503105001  
Serial No.: 20658-04-001P  
Company: MTS Systems Corp.

Device: ICP Accelerometer  
Model No.: 308B  
Serial No.: 10430  
Company: PCB Piezotronics

Device: Power Unit  
Model No.: 480D06  
Serial No.: 5163  
Company: PCB Piezotronics

## HYDRAULIC COMPONENTS

Device: A.C. Motor  
Model No.: 2U2100  
Serial No.: D-75  
Company: Delco

Device: Vickers Variable Volume Piston Pump  
Model No.: F3-PVB20-FRS-20-C-11  
Company: Sperry Rand Corp.

Device: Hydraulic Valve - Joint one of RALF  
Model No.: 73-102A  
Serial No.: 144  
Company: Moog, Inc.

Device: Hydraulic Valve - Joint two of RALF  
Model No.: 73-102A  
Serial No.: 147  
Company: Moog, Inc.

Device: Hydraulic Cylinder - Joint one of RALF  
Model No.: H-PB-2  
Serial No.: 37781-J  
Company: Atlas Cylinder Corp.

Device: Hydraulic Cylinder - Joint two of RALF  
Model No.: N2C-3.25x40  
Serial No.: 5C8205-065-1B  
Company: Hydro-Line Mfg. Co.

## APPENDIX D

### IMPULSE RESPONSE OF A SECOND-ORDER SYSTEM

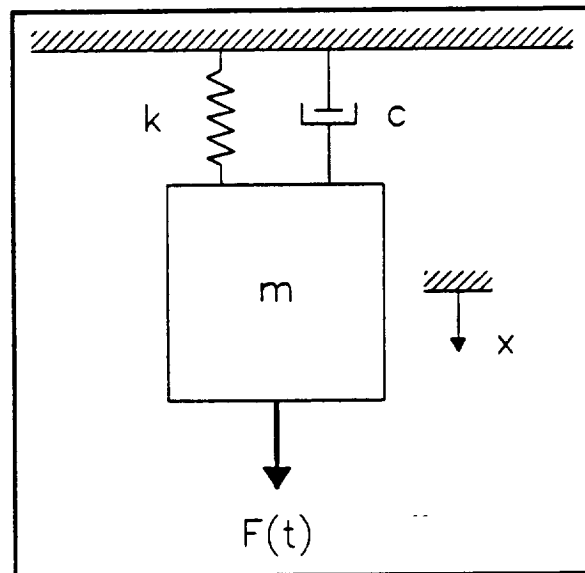


Figure D.1 Spring-Mass-Damper System

Recall that Newton's second law is

$$\sum \vec{F} = m\vec{a}. \quad (\text{D.1})$$

Newton's second law applied to the simple system shown in Figure D.1 yields

$$F(t) - kx - c \frac{dx}{dt} = m \frac{d^2x}{dt^2} \quad (\text{D.2})$$

which can be rearranged to get

$$m \frac{d^2x}{dt^2} + c \frac{dx}{dt} + kx = F(t). \quad (\text{D.3})$$

Dividing through by the mass, the system equation becomes

$$\frac{d^2x}{dt^2} + \frac{c}{m} \frac{dx}{dt} + \frac{k}{m} x = \frac{F(t)}{m}. \quad (\text{D.4})$$

By definition, the natural frequency of a second-order system is

$$\omega_n = \sqrt{\frac{k}{m}} \quad (\text{D.5})$$

and the damping ratio is

$$\zeta = \frac{c}{2\sqrt{km}}. \quad (\text{D.6})$$

Substituting into the system equation,

$$\frac{d^2x}{dt^2} + 2\zeta\omega_n\frac{dx}{dt} + \omega_n^2x = \frac{\omega_n^2}{c}F(t). \quad (D.7)$$

By defining an impulse force as

$$f(t) = \frac{F(t)}{c} \quad (D.8)$$

the system equation becomes

$$\frac{d^2x}{dt^2} + 2\zeta\omega_n\frac{dx}{dt} + \omega_n^2x = \omega_n^2f(t). \quad (D.9)$$

Let the impulse force have the form

$$f(t) = A\delta(t - t_0) \quad (D.10)$$

where  $A$  is an amplitude and  $\delta(t)$  is the Dirac delta function. A Dirac delta function is defined mathematically in Equation (D.11) and is displayed in Figure D.2 on the following page.

$$\int_{-\infty}^{\infty} \delta(t - t_0) dt = 1 \quad (D.11)$$

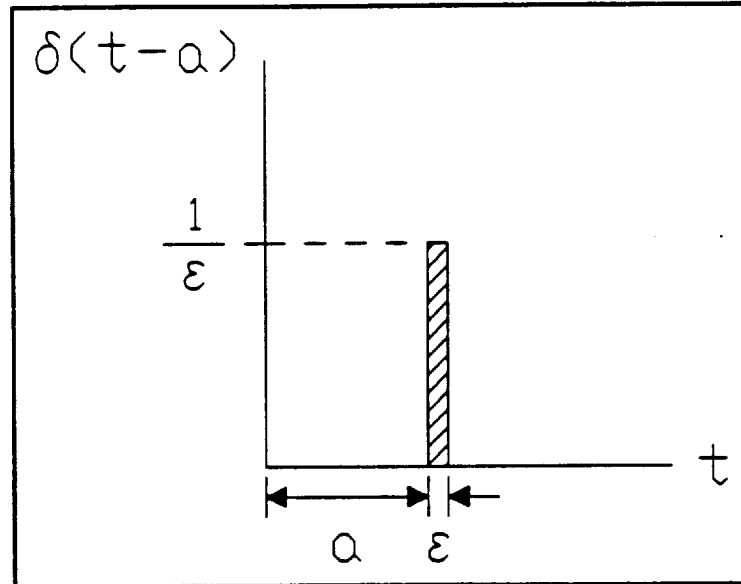


Figure D.2 Dirac Delta Function

From Figure D.2, it is apparent that the Dirac delta function has an amplitude of  $1/(\text{time})$ . The impulse function  $f(t)$ , given in Equation (D.10), must have units of length. This results in the amplitude  $A$  having units of  $(\text{length} \cdot \text{time})$ . It is sometimes very helpful to conduct unit analysis of this type to better understand the physics of the problem.

The new system equation becomes

$$\frac{d^2x}{dt^2} + 2\zeta\omega_n \frac{dx}{dt} + \omega_n^2 x = \omega_n^2 A \delta(t-t_0). \quad (\text{D.12})$$

Recall the definition of the Laplace Transform

$$F(s) = \int_0^\infty f(t) e^{-st} dt. \quad (\text{D.13})$$

Taking the Laplace Transform of the system equation assuming zero initial conditions yields

$$s^2 X(s) + 2\zeta \omega_n s X(s) + \omega_n^2 X(s) = A \omega_n^2 e^{-st_0} \quad (\text{D.14})$$

which can be rearranged to get

$$X(s) = \frac{A \omega_n^2 e^{-st_0}}{s^2 + 2\zeta \omega_n s + \omega_n^2} \quad (\text{D.15})$$

Partial fraction expansion of the equation yields

$$X(s) = \frac{jA \omega_n e^{-st_0}}{2\sqrt{1-\zeta^2}} \left( \frac{1}{s + \zeta \omega_n + j\omega_n \sqrt{1-\zeta^2}} - \frac{1}{s + \zeta \omega_n - j\omega_n \sqrt{1-\zeta^2}} \right) \quad (\text{D.16})$$

The inverse Laplace Transform of this expression is

$$x(t) = \frac{jA \omega_n}{2\sqrt{1-\zeta^2}} \left( e^{-(\zeta \omega_n + j\omega_n \sqrt{1-\zeta^2})(t-t_0)} - e^{-(\zeta \omega_n - j\omega_n \sqrt{1-\zeta^2})(t-t_0)} \right) \quad (\text{D.17})$$

which is just

$$x(t) = \frac{A \omega_n e^{-\zeta \omega_n (t-t_0)}}{\sqrt{1-\zeta^2}} \left( \frac{e^{j\omega_n \sqrt{1-\zeta^2} (t-t_0)} - e^{-j\omega_n \sqrt{1-\zeta^2} (t-t_0)}}{2j} \right). \quad (\text{D.18})$$

Recalling the Euler representation for sine is

$$\sin(\alpha) = \frac{e^{j\alpha} - e^{-j\alpha}}{2j}, \quad (\text{D.19})$$

the second-order system response to an impulse force becomes

$$x(t) = \frac{A \omega_n e^{-\zeta \omega_n (t-t_0)}}{\sqrt{1-\zeta^2}} \sin(\omega_n \sqrt{1-\zeta^2} (t-t_0)). \quad (\text{D.20})$$



## APPENDIX E

### SUMMATION OF TWO SINUSOIDS

The following two sinusoidal responses,

$$x_1(t) = B_1 \sin(\alpha t + \phi_1) \quad (\text{E.1})$$

$$x_2(t) = B_2 \sin(\alpha t + \phi_2) \quad (\text{E.2})$$

can be linearly combined to form a total response,  $x(t)$ , where

$$x(t) = B_1 \sin(\alpha t + \phi_1) + B_2 \sin(\alpha t + \phi_2) . \quad (\text{E.3})$$

Recall that

$$\sin(a + b) = \sin(a) \cos(b) + \sin(b) \cos(a) . \quad (\text{E.4})$$

So the total response becomes

$$x(t) = B_1 [\sin(\alpha t) \cos(\phi_1) + \sin(\phi_1) \cos(\alpha t)] + B_2 [\sin(\alpha t) \cos(\phi_2) + \sin(\phi_2) \cos(\alpha t)] \quad (\text{E.5})$$

which is just

$$x(t) = [B_1 \cos(\phi_1) + B_2 \cos(\phi_2)] \sin(\alpha t) + [B_1 \sin(\phi_1) + B_2 \sin(\phi_2)] \cos(\alpha t). \quad (\text{E.6})$$

Recall that the Euler representations for sine and cosine are

$$\sin(\omega) = \frac{e^{j\omega} - e^{-j\omega}}{2j} \quad (\text{E.7}) \quad \cos(\omega) = \frac{e^{j\omega} + e^{-j\omega}}{2}. \quad (\text{E.8})$$

Substituting,

$$x(t) = [B_1 \cos(\phi_1) + B_2 \cos(\phi_2)] \left[ \frac{e^{j\alpha t} - e^{-j\alpha t}}{2j} \right] + [B_1 \sin(\phi_1) + B_2 \sin(\phi_2)] \left[ \frac{e^{j\alpha t} + e^{-j\alpha t}}{2} \right] \quad (\text{E.9})$$

Rearranging the coefficients of the exponential terms,

$$\begin{aligned} x(t) = & [(B_1 \cos(\phi_1) + B_2 \cos(\phi_2)) + j(B_1 \sin(\phi_1) + B_2 \sin(\phi_2))] \frac{e^{j\alpha t}}{2j} \\ & - [(B_1 \cos(\phi_1) + B_2 \cos(\phi_2)) - j(B_1 \sin(\phi_1) + B_2 \sin(\phi_2))] \frac{e^{-j\alpha t}}{2j}. \end{aligned} \quad (\text{E.10})$$

Recall that any complex number can be written in the form

$$z = r e^{j\theta} \quad (\text{E.11})$$

where  $r$  is the magnitude and  $\theta$  is the phase.

Using this idea,  $x(t)$  can be expanded as follows

$$\begin{aligned}
 x(t) = & \left[ \sqrt{[B_1 \cos(\phi_1) + B_2 \cos(\phi_2)]^2 + [B_1 \sin(\phi_1) + B_2 \sin(\phi_2)]^2} e^{j \tan^{-1} \left( \frac{B_1 \sin(\phi_1) + B_2 \sin(\phi_2)}{B_1 \cos(\phi_1) + B_2 \cos(\phi_2)} \right)} \right] \frac{e^{j\alpha t}}{2j} \\
 & - \left[ \sqrt{[B_1 \cos(\phi_1) + B_2 \cos(\phi_2)]^2 + [B_1 \sin(\phi_1) + B_2 \sin(\phi_2)]^2} e^{-j \tan^{-1} \left( \frac{B_1 \sin(\phi_1) + B_2 \sin(\phi_2)}{B_1 \cos(\phi_1) + B_2 \cos(\phi_2)} \right)} \right] \frac{e^{-j\alpha t}}{2j}
 \end{aligned}
 \tag{E.12}$$

and simplifying,

$$\begin{aligned}
 x(t) = & \left[ \sqrt{[B_1 \cos(\phi_1) + B_2 \cos(\phi_2)]^2 + [B_1 \sin(\phi_1) + B_2 \sin(\phi_2)]^2} \right] \\
 & * \left[ \frac{e^{j \left( \alpha t + \tan^{-1} \left( \frac{B_1 \sin(\phi_1) + B_2 \sin(\phi_2)}{B_1 \cos(\phi_1) + B_2 \cos(\phi_2)} \right) \right)} - e^{-j \left( \alpha t + \tan^{-1} \left( \frac{B_1 \sin(\phi_1) + B_2 \sin(\phi_2)}{B_1 \cos(\phi_1) + B_2 \cos(\phi_2)} \right) \right)}}{2j} \right]
 \end{aligned}
 \tag{E.13}$$

and recalling the Euler representation for sine,

$$\begin{aligned}
 x(t) = & \left[ \sqrt{[B_1 \cos(\phi_1) + B_2 \cos(\phi_2)]^2 + [B_1 \sin(\phi_1) + B_2 \sin(\phi_2)]^2} \right] \\
 & * \sin \left[ \alpha t + \tan^{-1} \left( \frac{B_1 \sin(\phi_1) + B_2 \sin(\phi_2)}{B_1 \cos(\phi_1) + B_2 \cos(\phi_2)} \right) \right].
 \end{aligned}
 \tag{E.14}$$

This result can be rewritten as

$$x(t) = B_{amp} \sin(\alpha t + \psi) \quad (\text{E.15})$$

where

$$B_{amp} = \sqrt{[B_1 \cos(\phi_1) + B_2 \cos(\phi_2)]^2 + [B_1 \sin(\phi_1) + B_2 \sin(\phi_2)]^2} \quad (\text{E.16})$$

$$\psi = \tan^{-1} \left( \frac{B_1 \sin(\phi_1) + B_2 \sin(\phi_2)}{B_1 \cos(\phi_1) + B_2 \cos(\phi_2)} \right). \quad (\text{E.17})$$

This result can now be generalized. The total response,  $x(t)$ , which is the linear combination of  $N$  sinusoidal responses can be written as

$$x(t) = B_{amp} \sin(\alpha t + \psi) \quad (\text{E.18})$$

where

$$B_{amp} = \sqrt{\left[ \sum_{k=1}^N B_k \cos(\phi_k) \right]^2 + \left[ \sum_{k=1}^N B_k \sin(\phi_k) \right]^2} \quad (\text{E.19})$$

$$\psi = \tan^{-1} \left( \frac{\sum_{k=1}^N B_k \sin(\phi_k)}{\sum_{k=1}^N B_k \cos(\phi_k)} \right). \quad (\text{E.20})$$

## APPENDIX F

### CALCULATIONS FOR TWO IMPULSES

The constraint equations that must be satisfied are

$$B_1 \cos(\phi_1) + B_2 \cos(\phi_2) = 0 \quad (\text{F.1})$$

$$B_1 \sin(\phi_1) + B_2 \sin(\phi_2) = 0 \quad (\text{F.2})$$

where

$$B_k = \frac{A_k \omega_n}{\sqrt{1 - \zeta^2}} e^{-\zeta \omega_n (t - t_{0k})} \quad (\text{F.3})$$

and

$$\phi_k = -\omega_n t_{0k} \sqrt{1 - \zeta^2}. \quad (\text{F.4})$$

Notice that there are four unknowns ( $A_1$ ,  $A_2$ ,  $t_{01}$  and  $t_{02}$ ) and only two constraint equations. The other two constraints are the starting time of the first impulse and the normalization of the amplitudes.

Pick  $t_{01} = 0$  so that Equations (F.1) and (F.2) become

$$B_1 + B_2 \cos(\phi_2) = 0 \quad (\text{F.5})$$

$$B_2 \sin(\phi_2) = 0. \quad (\text{F.6})$$

The two solutions that exist for Equation (F.6) are either  $B_2 = 0$  or

$$\phi_2 = n\pi \quad (\text{F.7})$$

where  $n = \pm 0, 1, 2, 3, \dots$ . Avoiding the trivial solution, pick  $n = -1$  so that

$$\phi_2 = -\pi. \quad (\text{F.8})$$

From Equation (F.4), the second impulse occurs in time at

$$t_{02} = \frac{\pi}{\omega_n \sqrt{1 - \zeta^2}}. \quad (\text{F.9})$$

Substituting Equation (F.8) into Equation (F.5) yields

$$B_1 = B_2. \quad (\text{F.10})$$

At  $t = t_{02}$ , Equation (F.10) produces

$$\frac{A_1 \omega_n}{\sqrt{1 - \zeta^2}} e^{-\zeta \omega_n (t_{02} - t_{01})} = \frac{A_2 \omega_n}{\sqrt{1 - \zeta^2}} e^{-\zeta \omega_n (t_{02} - t_{02})} \quad (\text{F.11})$$

or

$$A_2 = A_1 e^{-\frac{\zeta \pi}{\sqrt{1 - \zeta^2}}} \quad (\text{F.12})$$

If the amplitudes are normalized so that

$$\sum_{i=1}^2 A_i = 1 \quad (\text{F.13})$$

and let

$$M = e^{-\frac{\zeta \pi}{\sqrt{1 - \zeta^2}}}, \quad (\text{F.14})$$



then the amplitudes of the two impulses and the times at which they occur are

$$A_1 = \frac{1}{1+M} \quad (\text{F.15})$$

$$t_{01} = 0 \quad (\text{F.16})$$

$$A_2 = \frac{M}{1+M} \quad (\text{F.17})$$

$$t_{02} = \frac{\pi}{\omega_n \sqrt{1-\zeta^2}}. \quad (\text{F.18})$$

Now that the amplitudes and times of the impulses are known, the theoretical impulse response of a second-order system can be found using the results from Appendix D.

## APPENDIX G

### CALCULATIONS FOR THREE IMPULSES

The constraint equations that must be satisfied are

$$B_1 \cos(\phi_1) + B_2 \cos(\phi_2) + B_3 \cos(\phi_3) = 0 \quad (\text{G.1})$$

$$B_1 \sin(\phi_1) + B_2 \sin(\phi_2) + B_3 \sin(\phi_3) = 0 \quad (\text{G.2})$$

$$B_1 t_{01} \cos(\phi_1) + B_2 t_{02} \cos(\phi_2) + B_3 t_{03} \cos(\phi_3) = 0 \quad (\text{G.3})$$

$$B_1 t_{01} \sin(\phi_1) + B_2 t_{02} \sin(\phi_2) + B_3 t_{03} \sin(\phi_3) = 0 \quad (\text{G.4})$$

where

$$B_k = \frac{A_k \omega_n}{\sqrt{1 - \zeta^2}} e^{-\zeta \omega_n (t - t_{0k})} \quad (\text{G.5})$$

and

$$\phi_k = -\omega_n t_{0k} \sqrt{1 - \zeta^2}. \quad (\text{G.6})$$

Notice that there are six unknowns ( $A_1, A_2, A_3, t_{01}, t_{02}$  and  $t_{03}$ ) and only four constraint equations. The other two constraints are the starting time of the first impulse and the normalization of the amplitudes.

Pick  $t_{01} = 0$  so that Equations (G.1) through (G.4) become

$$B_1 + B_2 \cos(\phi_2) + B_3 \cos(\phi_3) = 0 \quad (\text{G.7})$$

$$B_2 \sin(\phi_2) + B_3 \sin(\phi_3) = 0 \quad (\text{G.8})$$

$$B_2 t_{02} \cos(\phi_2) + B_3 t_{03} \cos(\phi_3) = 0 \quad (\text{G.9})$$

$$B_2 t_{02} \sin(\phi_2) + B_3 t_{03} \sin(\phi_3) = 0. \quad (\text{G.10})$$

From Equation (G.8),

$$B_2 \sin(\phi_2) = -B_3 \sin(\phi_3) \quad (\text{G.11})$$

which is substituted into Equation (G.10) to produce

$$B_3(t_{03} - t_{02})\sin(\phi_3) = 0. \quad (\text{G.12})$$

The three solutions that exist for Equation (G.12) are

$$B_3 = 0 \quad (\text{G.13})$$

$$t_{03} - t_{02} = 0 \quad (\text{G.14})$$

$$\phi_3 = n\pi \quad (\text{G.15})$$

where  $n = \pm 0, 1, 2, 3, \dots$ . Avoiding the trivial solutions, pick  $n = -2$  so that

$$\phi_3 = -2\pi. \quad (\text{G.16})$$

From Equation (G.6), the third impulse occurs in time at

$$t_{03} = \frac{2\pi}{\omega_n \sqrt{1 - \zeta^2}}. \quad (\text{G.17})$$

Substituting Equation (G.16) into Equation (G.8) yields

$$B_2 \sin(\phi_2) = 0. \quad (G.18)$$

The two solutions that exist for Equation (G.18) are

$$B_2 = 0 \quad (G.19)$$

$$\phi_2 = n \pi \quad (G.20)$$

where  $n = \pm 0, 1, 2, 3, \dots$ . Avoiding the trivial solution, pick  $n = -1$  so that

$$\phi_2 = -\pi. \quad (G.21)$$

From Equation (G.6), the second impulse occurs in time at

$$t_{02} = \frac{\pi}{\omega_n \sqrt{1 - \zeta^2}}. \quad (G.22)$$

Now that the times at which the impulses occur is known, the amplitudes of the three impulses can be found. Substituting Equations (G.16) and (G.21) into Equations (G.7) and (G.9) produces

$$B_1 - B_2 + B_3 = 0 \quad (G.23)$$

$$-B_2 t_{02} + B_3 t_{03} = 0. \quad (\text{G.24})$$

From Equations (G.17) and (G.22), the relationship between the times is

$$t_{03} = 2 t_{02}. \quad (\text{G.25})$$

Substituting this time relationship into Equation (G.24) yields

$$B_2 = 2 B_1 \quad (\text{G.26})$$

$$B_3 = B_1. \quad (\text{G.27})$$

At  $t = t_{02}$ , Equation (G.26) produces

$$\frac{A_2 \omega_n}{\sqrt{1-\zeta^2}} e^{-\zeta \omega_n (t_{02} - t_{02})} = \frac{2 A_1 \omega_n}{\sqrt{1-\zeta^2}} e^{-\zeta \omega_n (t_{02} - t_{01})} \quad (\text{G.28})$$

or

$$A_2 = 2 A_1 e^{-\frac{\zeta \pi}{\sqrt{1-\zeta^2}}}. \quad (\text{G.29})$$

At  $t = t_{03}$ , Equation (G.27) produces

$$\frac{A_3 \omega_n}{\sqrt{1 - \zeta^2}} e^{-\zeta \omega_n (t_{03} - t_{03})} = \frac{A_1 \omega_n}{\sqrt{1 - \zeta^2}} e^{-\zeta \omega_n (t_{03} - t_{01})} \quad (\text{G.30})$$

or

$$A_3 = A_1 e^{-\frac{2\zeta\pi}{\sqrt{1 - \zeta^2}}} \quad (\text{G.31})$$

If the amplitudes are normalized so that

$$\sum_{i=1}^3 A_i = 1 \quad (\text{G.32})$$

and let

$$M = e^{-\frac{\zeta\pi}{\sqrt{1 - \zeta^2}}} \quad (\text{G.33})$$

then the amplitudes of the three impulses and the times at which they occur are

$$A_1 = \frac{1}{1 + 2M + M^2} \quad (\text{G.34})$$

$$t_{01} = 0 \quad (\text{G.35})$$

$$A_2 = \frac{2M}{1 + 2M + M^2} \quad (\text{G.36})$$

$$t_{02} = \frac{\pi}{\omega_n \sqrt{1 - \zeta^2}} \quad (\text{G.37})$$

$$A_3 = \frac{M^2}{1 + 2M + M^2} \quad (\text{G.38})$$

$$t_{03} = \frac{2\pi}{\omega_n \sqrt{1 - \zeta^2}} \quad (\text{G.39})$$

Now that the amplitudes and times of the impulses are known, the theoretical impulse response of a second-order system can be found using the results from Appendix D.



## APPENDIX H

### CALCULATIONS FOR FOUR IMPULSES

The constraint equations that must be satisfied are

$$B_1 \cos(\phi_1) + B_2 \cos(\phi_2) + B_3 \cos(\phi_3) + B_4 \cos(\phi_4) = 0 \quad (\text{H.1})$$

$$B_1 \sin(\phi_1) + B_2 \sin(\phi_2) + B_3 \sin(\phi_3) + B_4 \sin(\phi_4) = 0 \quad (\text{H.2})$$

$$B_1 t_{01} \cos(\phi_1) + B_2 t_{02} \cos(\phi_2) + B_3 t_{03} \cos(\phi_3) + B_4 t_{04} \cos(\phi_4) = 0 \quad (\text{H.3})$$

$$B_1 t_{01} \sin(\phi_1) + B_2 t_{02} \sin(\phi_2) + B_3 t_{03} \sin(\phi_3) + B_4 t_{04} \sin(\phi_4) = 0 \quad (\text{H.4})$$

$$B_1 t_{01}^2 \cos(\phi_1) + B_2 t_{02}^2 \cos(\phi_2) + B_3 t_{03}^2 \cos(\phi_3) + B_4 t_{04}^2 \cos(\phi_4) = 0 \quad (\text{H.5})$$

$$B_1 t_{01}^2 \sin(\phi_1) + B_2 t_{02}^2 \sin(\phi_2) + B_3 t_{03}^2 \sin(\phi_3) + B_4 t_{04}^2 \sin(\phi_4) = 0 \quad (\text{H.6})$$

where

$$B_k = \frac{A_k \omega_n}{\sqrt{1 - \zeta^2}} e^{-\zeta \omega_n (t - t_{0k})} \quad (\text{H.7})$$

and

$$\phi_k = -\omega_n t_{0k} \sqrt{1 - \zeta^2}. \quad (\text{H.8})$$

Notice that there are eight unknowns ( $A_1, A_2, A_3, A_4, t_{01}, t_{02}, t_{03}$  and  $t_{04}$ ) and only six constraint equations. The other two constraints are the starting time of the first impulse and the normalization of the amplitudes.

Pick  $t_{01} = 0$  so that Equations (H.1) through (H.6) become

$$B_1 + B_2 \cos(\phi_2) + B_3 \cos(\phi_3) + B_4 \cos(\phi_4) = 0 \quad (\text{H.9})$$

$$B_2 \sin(\phi_2) + B_3 \sin(\phi_3) + B_4 \sin(\phi_4) = 0 \quad (\text{H.10})$$

$$B_2 t_{02} \cos(\phi_2) + B_3 t_{03} \cos(\phi_3) + B_4 t_{04} \cos(\phi_4) = 0 \quad (\text{H.11})$$

$$B_2 t_{02} \sin(\phi_2) + B_3 t_{03} \sin(\phi_3) + B_4 t_{04} \sin(\phi_4) = 0 \quad (\text{H.12})$$

$$B_2 t_{02}^2 \cos(\phi_2) + B_3 t_{03}^2 \cos(\phi_3) + B_4 t_{04}^2 \cos(\phi_4) = 0 \quad (\text{H.13})$$

$$B_2 t_{02}^2 \sin(\phi_2) + B_3 t_{03}^2 \sin(\phi_3) + B_4 t_{04}^2 \sin(\phi_4) = 0. \quad (\text{H.14})$$

From Equation (H.10),

$$B_2 \sin(\phi_2) = -[B_3 \sin(\phi_3) + B_4 \sin(\phi_4)] \quad (\text{H.15})$$

which is substituted into Equations (H.12) and (H.14) to produce

$$B_3(t_{03} - t_{02})\sin(\phi_3) + B_4(t_{04} - t_{02})\sin(\phi_4) = 0 \quad (\text{H.16})$$

$$B_3(t_{03}^2 - t_{02}^2)\sin(\phi_3) + B_4(t_{04}^2 - t_{02}^2)\sin(\phi_4) = 0. \quad (\text{H.17})$$

Solving for  $B_3$  from Equation (H.16) and substituting into Equation (H.17) yields

$$B_4(t_{04} - t_{03})\sin(\phi_4) = 0. \quad (\text{H.18})$$

The three solutions that exist for Equation (H.18) are

$$B_4 = 0 \quad (\text{H.19})$$

$$t_{04} - t_{03} = 0 \quad (\text{H.20})$$

$$\phi_4 = n \pi \quad (\text{H.21})$$

where  $n = \pm 0, 1, 2, 3, \dots$ . Avoiding the trivial solutions, pick  $n = -3$  so that

$$\phi_4 = -3 \pi. \quad (\text{H.22})$$

From Equation (H.8), the fourth impulse occurs in time at

$$t_{04} = \frac{3 \pi}{\omega_n \sqrt{1 - \zeta^2}}. \quad (\text{H.23})$$

Substituting Equation (H.22) into Equation (H.16) yields

$$B_3(t_{03} - t_{02})\sin(\phi_3) = 0. \quad (\text{H.24})$$

The three solutions that exist for Equation (H.24) are

$$B_3 = 0 \quad (\text{H.25})$$

$$t_{03} - t_{02} = 0 \quad (\text{H.26})$$

$$\phi_3 = n \pi \quad (\text{H.27})$$

where  $n = \pm 0, 1, 2, 3, \dots$ . Avoiding the trivial solutions, pick  $n = -2$  so that

$$\phi_3 = -2 \pi. \quad (\text{H.28})$$

From Equation (H.8), the third impulse occurs in time at

$$t_{03} = \frac{2 \pi}{\omega_n \sqrt{1 - \zeta^2}}. \quad (\text{H.29})$$

Substituting Equations (H.22) and (H.28) into Equation (H.10) yields

$$B_2 \sin(\phi_2) = 0. \quad (\text{H.30})$$

The two solutions that exist for Equation (H.30) are

$$B_2 = 0 \quad (\text{H.31})$$

$$\phi_2 = n \pi \quad (\text{H.32})$$

where  $n = \pm 0, 1, 2, 3, \dots$ . Avoiding the trivial solution, pick  $n = -1$  so that

$$\phi_2 = -\pi. \quad (\text{H.33})$$

From Equation (H.8), the second impulse occurs in time at

$$t_{02} = \frac{\pi}{\omega_n \sqrt{1 - \zeta^2}}. \quad (\text{H.34})$$

Now that the times at which the impulses occur is known, the amplitudes of the four impulses can be found. Substituting Equations (H.22), (H.28) and (H.33) into Equations (H.9), (H.11) and (H.13) produces

$$B_1 - B_2 + B_3 - B_4 = 0 \quad (\text{H.35})$$

$$-B_2 t_{02} + B_3 t_{03} - B_4 t_{04} = 0 \quad (\text{H.36})$$

$$-B_2 t_{02}^2 + B_3 t_{03}^2 - B_4 t_{04}^2 = 0. \quad (\text{H.37})$$

From Equations (H.23), (H.29) and (H.34), the relationships between the times are

$$t_{03} = 2 t_{02} \quad (\text{H.38})$$

$$t_{04} = 3 t_{02} \quad (\text{H.39})$$

Substituting these time relationships into Equations (H.36) and (H.37) yields

$$B_2 = 3 B_1 \quad (\text{H.40})$$

$$B_3 = 3 B_1 \quad (\text{H.41})$$

$$B_4 = B_1 \quad (\text{H.42})$$

At  $t = t_{02}$ , Equation (H.40) produces

$$\frac{A_2 \omega_n}{\sqrt{1 - \zeta^2}} e^{-\zeta \omega_n (t_{02} - t_{02})} = \frac{3 A_1 \omega_n}{\sqrt{1 - \zeta^2}} e^{-\zeta \omega_n (t_{02} - t_{01})} \quad (\text{H.43})$$

or

$$A_2 = 3A_1 e^{-\frac{\zeta \pi}{\sqrt{1-\zeta^2}}}. \quad (\text{H.44})$$

At  $t = t_{03}$ , Equation (H.41) produces

$$\frac{A_3 \omega_n}{\sqrt{1-\zeta^2}} e^{-\zeta \omega_n (t_{03} - t_{03})} = \frac{3A_1 \omega_n}{\sqrt{1-\zeta^2}} e^{-\zeta \omega_n (t_{03} - t_{01})} \quad (\text{H.45})$$

or

$$A_3 = 3A_1 e^{-\frac{2\zeta \pi}{\sqrt{1-\zeta^2}}}. \quad (\text{H.46})$$

At  $t = t_{04}$ , Equation (H.42) produces

$$\frac{A_4 \omega_n}{\sqrt{1-\zeta^2}} e^{-\zeta \omega_n (t_{04} - t_{04})} = \frac{A_1 \omega_n}{\sqrt{1-\zeta^2}} e^{-\zeta \omega_n (t_{04} - t_{01})} \quad (\text{H.47})$$

or

$$A_4 = A_1 e^{-\frac{3\zeta \pi}{\sqrt{1-\zeta^2}}}. \quad (\text{H.48})$$



If the amplitudes are normalized so that

$$\sum_{i=1}^4 A_i = 1 \quad (\text{H.49})$$

and let

$$M = e^{-\frac{\zeta \pi}{\sqrt{1-\zeta^2}}}, \quad (\text{H.50})$$

then the amplitudes of the four impulses and the times at which they occur are

$$A_1 = \frac{1}{1 + 3M + 3M^2 + M^3} \quad (\text{H.51})$$

$$t_{01} = 0 \quad (\text{H.52})$$

$$A_2 = \frac{3M}{1 + 3M + 3M^2 + M^3} \quad (\text{H.53})$$

$$t_{02} = \frac{\pi}{\omega_n \sqrt{1-\zeta^2}} \quad (\text{H.54})$$

$$A_3 = \frac{3M^2}{1 + 3M + 3M^2 + M^3} \quad (\text{H.55})$$

$$t_{03} = \frac{2\pi}{\omega_n \sqrt{1-\zeta^2}} \quad (\text{H.56})$$

$$A_4 = \frac{M^3}{1 + 3M + 3M^2 + M^3} \quad (\text{H.57})$$

$$t_{04} = \frac{3\pi}{\omega_n \sqrt{1-\zeta^2}} \quad (\text{H.58})$$

Now that the amplitudes and times of the impulses are known, the theoretical impulse response of a second-order system can be found using the results from Appendix D.

## APPENDIX I

### CALCULATIONS FOR DEVIATIONS IN NATURAL FREQUENCY

This appendix evaluates the residual vibration of the input shaping technique when the actual natural frequency,  $\omega_a$ , deviates from the design natural frequency,  $\omega_n$ . The magnitude of the residual vibration is important since the impulse characteristics, used for input shaping, are based on the design natural frequency values.

Using the results derived in Appendix D, the actual response of a second-order system to an impulse of unity gain is

$$x_a(t) = \frac{\omega_a}{\sqrt{1 - \zeta^2}} e^{-\zeta \omega_a t} \sin(\omega_a \sqrt{1 - \zeta^2} t). \quad (I.1)$$

If the single impulse is divided into two impulses with characteristics derived in Appendix F, the actual response for  $t \geq t_{02}$  becomes

$$x_{2a}(t) = x_1(t) + x_2(t) \quad (I.2)$$

where

$$x_1(t) = \frac{1}{M+1} \frac{\omega_a}{\sqrt{1-\zeta^2}} e^{-\zeta \omega_a t} \sin(\omega_a \sqrt{1-\zeta^2} t) \quad (I.3)$$

$$x_2(t) = \frac{M}{M+1} \frac{\omega_a}{\sqrt{1-\zeta^2}} e^{-\zeta \omega_a (t-t_{02})} \sin(\omega_a \sqrt{1-\zeta^2} (t-t_{02})). \quad (I.4)$$

Using the results derived in Appendix E, the actual system response to the two impulse input for  $t \geq t_{02}$  can be expressed as

$$x_{2a}(t) = B_{2a} \sin(\alpha t + \psi_{2a}) \quad (I.5)$$

where

$$B_{2a} = \frac{1}{M+1} \frac{\omega_a}{\sqrt{1-\zeta^2}} e^{-\zeta \omega_a t} \sqrt{1 + 2M^{1-\frac{\omega_a}{\omega_n}} \cos\left(\frac{\omega_a}{\omega_n} \pi\right) + M^{2\left(1-\frac{\omega_a}{\omega_n}\right)}} \quad (I.6)$$

$$\psi_{2a} = -\tan^{-1} \left( \frac{M \left(1 - \frac{\omega_a}{\omega_n}\right) \sin\left(\frac{\omega_a}{\omega_n} \pi\right)}{1 + M \left(1 - \frac{\omega_a}{\omega_n}\right) \cos\left(\frac{\omega_a}{\omega_n} \pi\right)} \right). \quad (I.7)$$

To determine the amount of residual vibration, a vibration error expression must be defined. The error, denoted *err*, can be expressed as the ratio of the actual multiple impulse response magnitude to the actual impulse response magnitude of a second-order system. The error expression is defined only for time after the multiple impulse input has occurred to ensure that the system has received identical amplitude inputs. Mathematically, this is written as

$$err = \frac{|x_{ka}(t)|}{|x_a(t)|}, \quad \text{for } t \geq t_{0k} \quad (I.8)$$

where *k* is the number of impulses. The residual vibration is the vibration error expressed as a percentage. Using Equations (I.1) and (I.5), the vibration error for the two impulse input becomes

$$\frac{|x_{2a}(t)|}{|x_a(t)|} = \left| \frac{1}{M+1} \sqrt{1 + 2M \left(1 - \frac{\omega_a}{\omega_n}\right) \cos\left(\frac{\omega_a}{\omega_n} \pi\right) + M^2 \left(1 - \frac{\omega_a}{\omega_n}\right)^2} \right|. \quad (I.9)$$

If the single impulse is divided into three impulses with characteristics derived in Appendix G, the actual response for  $t \geq t_{03}$  becomes

$$x_{3a}(t) = x_1(t) + x_2(t) + x_3(t) \quad (\text{I.10})$$

where

$$x_1(t) = \frac{1}{1 + 2M + M^2} \frac{\omega_a}{\sqrt{1 - \zeta^2}} e^{-\zeta \omega_a t} \sin(\omega_a \sqrt{1 - \zeta^2} t) \quad (\text{I.11})$$

$$x_2(t) = \frac{2M}{1 + 2M + M^2} \frac{\omega_a}{\sqrt{1 - \zeta^2}} e^{-\zeta \omega_a (t - t_{02})} \sin(\omega_a \sqrt{1 - \zeta^2} (t - t_{02})) \quad (\text{I.12})$$

$$x_3(t) = \frac{M^2}{1 + 2M + M^2} \frac{\omega_a}{\sqrt{1 - \zeta^2}} e^{-\zeta \omega_a (t - t_{03})} \sin(\omega_a \sqrt{1 - \zeta^2} (t - t_{03})). \quad (\text{I.13})$$

Using the results derived in Appendix E, the actual system response to the three impulse input for  $t \geq t_{03}$  can be expressed as

$$x_{3a}(t) = B_{3a} \sin(\alpha t + \psi_{3a}) \quad (\text{I.14})$$

where

$$B_{3a} = \frac{1}{1 + 2M + M^2} \omega_a e^{-\zeta \omega_a t} \sqrt{(\text{den}_{3a})^2 + (\text{num}_{3a})^2} \quad (\text{I.15})$$

$$\psi_{3a} = -\tan^{-1} \left( \frac{\text{num}_{3a}}{\text{den}_{3a}} \right) \quad (\text{I.16})$$

with

$$\text{num}_{3a} = 2M^{1-\frac{\omega_a}{\omega_n}} \sin\left(\frac{\omega_a}{\omega_n} \pi\right) + M^{2\left(1-\frac{\omega_a}{\omega_n}\right)} \sin\left(2 \frac{\omega_a}{\omega_n} \pi\right) \quad (\text{I.17})$$

$$\text{den}_{3a} = 1 + 2M^{1-\frac{\omega_a}{\omega_n}} \cos\left(\frac{\omega_a}{\omega_n} \pi\right) + M^{2\left(1-\frac{\omega_a}{\omega_n}\right)} \cos\left(2 \frac{\omega_a}{\omega_n} \pi\right). \quad (\text{I.18})$$

Substituting Equations (I.1) and (I.14) into Equation (I.8), the vibration error for the three impulse input becomes

$$\frac{|x_{3a}(t)|}{|x_a(t)|} = \left| \frac{1}{1 + 2M + M^2} \sqrt{(\text{den}_{3a})^2 + (\text{num}_{3a})^2} \right|. \quad (\text{I.19})$$

If the single impulse is divided into four impulses with characteristics derived in Appendix H, the actual response for  $t \geq t_{04}$  becomes

$$x_{4a}(t) = x_1(t) + x_2(t) + x_3(t) + x_4(t) \quad (I.20)$$

where

$$x_1(t) = \frac{\frac{1}{1 + 3M + 3M^2 + M^3} \omega_a}{\sqrt{1 - \zeta^2}} e^{-\zeta \omega_a t} \sin(\omega_a \sqrt{1 - \zeta^2} t) \quad (I.21)$$

$$x_2(t) = \frac{\frac{3M}{1 + 3M + 3M^2 + M^3} \omega_a}{\sqrt{1 - \zeta^2}} e^{-\zeta \omega_a (t - t_{02})} \sin(\omega_a \sqrt{1 - \zeta^2} (t - t_{02})) \quad (I.22)$$

$$x_3(t) = \frac{\frac{3M^2}{1 + 3M + 3M^2 + M^3} \omega_a}{\sqrt{1 - \zeta^2}} e^{-\zeta \omega_a (t - t_{03})} \sin(\omega_a \sqrt{1 - \zeta^2} (t - t_{03})) \quad (I.23)$$

$$x_4(t) = \frac{\frac{M^3}{1 + 3M + 3M^2 + M^3} \omega_a}{\sqrt{1 - \zeta^2}} e^{-\zeta \omega_a (t - t_{04})} \sin(\omega_a \sqrt{1 - \zeta^2} (t - t_{04})). \quad (I.24)$$



Using the results derived in Appendix E, the actual system response to the four impulse input for  $t \geq t_{04}$  can be expressed as

$$x_{4a}(t) = B_{4a} \sin(\alpha t + \psi_{4a}) \quad (I.25)$$

where

$$B_{4a} = \frac{1}{\sqrt{1 - \zeta^2}} \frac{\omega_a}{1 + 3M + 3M^2 + M^3} e^{-\zeta \omega_a t} \sqrt{(den_{4a})^2 + (num_{4a})^2} \quad (I.26)$$

$$\psi_{4a} = -\tan^{-1} \left( \frac{num_{4a}}{den_{4a}} \right) \quad (I.27)$$

with

$$num_{4a} = 3M^{1-\frac{\omega_a}{\omega_n}} \sin\left(\frac{\omega_a}{\omega_n} \pi\right) + 3M^{2\left(1-\frac{\omega_a}{\omega_n}\right)} \sin\left(2\frac{\omega_a}{\omega_n} \pi\right) + M^{3\left(1-\frac{\omega_a}{\omega_n}\right)} \sin\left(3\frac{\omega_a}{\omega_n} \pi\right) \quad (I.28)$$

$$den_{4a} = 1 + 3M^{1-\frac{\omega_a}{\omega_n}} \cos\left(\frac{\omega_a}{\omega_n} \pi\right) + 3M^{2\left(1-\frac{\omega_a}{\omega_n}\right)} \cos\left(2\frac{\omega_a}{\omega_n} \pi\right) + M^{3\left(1-\frac{\omega_a}{\omega_n}\right)} \cos\left(3\frac{\omega_a}{\omega_n} \pi\right). \quad (I.29)$$

Substituting Equations (I.1) and (I.25) into Equation (I.8), the vibration error for the four impulse input becomes

$$\frac{|x_{4a}(t)|}{|x_a(t)|} = \left| \frac{1}{1 + 3M + 3M^2 + M^3} \sqrt{(\text{den}_{4a})^2 + (\text{num}_{4a})^2} \right|. \quad (\text{I.30})$$

## APPENDIX J

### CALCULATIONS FOR DEVIATIONS IN DAMPING RATIO

This appendix evaluates the residual vibration of the input shaping technique when the actual damping ratio,  $\zeta_a$ , deviates from the design damping ratio,  $\zeta$ . The magnitude of the residual vibration is important since the impulse characteristics, used for input shaping, are based on the design damping ratio values.

Using the results derived in Appendix D, the actual response of a second-order system to an impulse of unity gain is

$$x_a(t) = \frac{\omega_n}{\sqrt{1 - \zeta_a^2}} e^{-\zeta_a \omega_n t} \sin\left(\omega_n \sqrt{1 - \zeta_a^2} t\right). \quad (J.1)$$

If the single impulse is divided into two impulses with characteristics derived in Appendix F, the actual response for  $t \geq t_{02}$  becomes

$$x_{2a}(t) = x_1(t) + x_2(t) \quad (J.2)$$

where

$$x_1(t) = \frac{1}{M+1} \frac{\omega_n}{\sqrt{1-\zeta_a^2}} e^{-\zeta_a \omega_n t} \sin(\omega_n \sqrt{1-\zeta_a^2} t) \quad (J.3)$$

$$x_2(t) = \frac{M}{M+1} \frac{\omega_n}{\sqrt{1-\zeta_a^2}} e^{-\zeta_a \omega_n (t-t_{02})} \sin(\omega_n \sqrt{1-\zeta_a^2} (t-t_{02})). \quad (J.4)$$

Using the results derived in Appendix E, the actual system response to the two impulse input for  $t \geq t_{02}$  can be expressed as

$$x_{2a}(t) = B_{2a} \sin(\alpha t + \psi_{2a}) \quad (J.5)$$

where

$$B_{2a} = \frac{1}{M+1} \frac{\omega_n}{\sqrt{1-\zeta_a^2}} e^{-\zeta_a \omega_n t} \sqrt{1 + 2M^{(1-\frac{\zeta_a}{\zeta})} \cos\left(\pi \sqrt{\frac{1-\zeta_a^2}{1-\zeta^2}}\right) + M^{2(1-\frac{\zeta_a}{\zeta})}} \quad (J.6)$$

$$\psi_{2a} = -\tan^{-1} \left( \frac{M^{1-\frac{\zeta_a}{\zeta}} \sin \left( \pi \sqrt{\frac{1-\zeta_a^2}{1-\zeta^2}} \right)}{1 + M^{1-\frac{\zeta_a}{\zeta}} \cos \left( \pi \sqrt{\frac{1-\zeta_a^2}{1-\zeta^2}} \right)} \right). \quad (J.7)$$

To determine the amount of residual vibration, a vibration error expression must be defined. The error, denoted *err*, can be expressed as the ratio of the actual multiple impulse response magnitude to the actual impulse response magnitude of a second-order system. The error expression is defined only for time after the multiple impulse input has occurred to ensure that the system has received identical amplitude inputs. Mathematically, this is written as

$$err = \frac{|x_{ka}(t)|}{|x_a(t)|}, \text{ for } t \geq t_{0k} \quad (J.8)$$

where *k* is the number of impulses. The residual vibration is the vibration error expressed as a percentage. Using Equations (J.1) and (J.5), the vibration error for the two impulse input becomes

$$\frac{|x_{2a}(t)|}{|x_a(t)|} = \left| \frac{1}{M+1} \sqrt{1 + 2M^{1-\frac{\zeta_a}{\zeta}} \cos \left( \pi \sqrt{\frac{1-\zeta_a^2}{1-\zeta^2}} \right) + M^{2\left(1-\frac{\zeta_a}{\zeta}\right)}} \right|. \quad (J.9)$$

If the single impulse is divided into three impulses with characteristics derived in Appendix G, the actual response for  $t \geq t_{03}$  becomes

$$x_{3a}(t) = x_1(t) + x_2(t) + x_3(t) \quad (J.10)$$

where

$$x_1(t) = \frac{1}{1 + 2M + M^2} \frac{\omega_n}{\sqrt{1 - \zeta_a^2}} e^{-\zeta_a \omega_n t} \sin(\omega_n \sqrt{1 - \zeta_a^2} t) \quad (J.11)$$

$$x_2(t) = \frac{2M}{1 + 2M + M^2} \frac{\omega_n}{\sqrt{1 - \zeta_a^2}} e^{-\zeta_a \omega_n (t - t_{02})} \sin(\omega_n \sqrt{1 - \zeta_a^2} (t - t_{02})) \quad (J.12)$$

$$x_3(t) = \frac{M^2}{1 + 2M + M^2} \frac{\omega_n}{\sqrt{1 - \zeta_a^2}} e^{-\zeta_a \omega_n (t - t_{03})} \sin(\omega_n \sqrt{1 - \zeta_a^2} (t - t_{03})). \quad (J.13)$$

Using the results derived in Appendix E, the actual system response to the three impulse input for  $t \geq t_{03}$  can be expressed as

$$x_{3a}(t) = B_{3a} \sin(\alpha t + \psi_{3a}) \quad (J.14)$$

where

$$B_{3a} = \frac{1}{1 + 2M + M^2} \omega_n e^{-\zeta_a \omega_n t} \sqrt{(den_{3a})^2 + (num_{3a})^2} \quad (J.15)$$

$$\psi_{3a} = -\tan^{-1} \left( \frac{num_{3a}}{den_{3a}} \right) \quad (J.16)$$

with

$$num_{3a} = 2M^{1-\frac{\zeta_a}{\zeta}} \sin \left( \pi \sqrt{\frac{1-\zeta_a^2}{1-\zeta^2}} \right) + M^{2\left(1-\frac{\zeta_a}{\zeta}\right)} \sin \left( 2\pi \sqrt{\frac{1-\zeta_a^2}{1-\zeta^2}} \right) \quad (J.17)$$

$$den_{3a} = 1 + 2M^{1-\frac{\zeta_a}{\zeta}} \cos \left( \pi \sqrt{\frac{1-\zeta_a^2}{1-\zeta^2}} \right) + M^{2\left(1-\frac{\zeta_a}{\zeta}\right)} \cos \left( 2\pi \sqrt{\frac{1-\zeta_a^2}{1-\zeta^2}} \right). \quad (J.18)$$

Substituting Equations (J.1) and (J.14) into Equation (J.8), the vibration error for the three impulse input becomes

$$\frac{|x_{3a}(t)|}{|x_a(t)|} = \left| \frac{1}{1 + 2M + M^2} \sqrt{(den_{3a})^2 + (num_{3a})^2} \right|. \quad (J.19)$$

If the single impulse is divided into four impulses with characteristics derived in Appendix H, the actual response for  $t \geq t_{04}$  becomes

$$x_{4a}(t) = x_1(t) + x_2(t) + x_3(t) + x_4(t) \quad (J.20)$$

where

$$x_1(t) = \frac{\frac{1}{1+3M+3M^2+M^3} \omega_n}{\sqrt{1-\zeta_a^2}} e^{-\zeta_a \omega_n t} \sin\left(\omega_n \sqrt{1-\zeta_a^2} t\right) \quad (J.21)$$

$$x_2(t) = \frac{\frac{3M}{1+3M+3M^2+M^3} \omega_n}{\sqrt{1-\zeta_a^2}} e^{-\zeta_a \omega_n (t-t_{02})} \sin\left(\omega_n \sqrt{1-\zeta_a^2} (t-t_{02})\right) \quad (J.22)$$

$$x_3(t) = \frac{\frac{3M^2}{1+3M+3M^2+M^3} \omega_n}{\sqrt{1-\zeta_a^2}} e^{-\zeta_a \omega_n (t-t_{03})} \sin\left(\omega_n \sqrt{1-\zeta_a^2} (t-t_{03})\right) \quad (J.23)$$

$$x_4(t) = \frac{\frac{M^3}{1+3M+3M^2+M^3} \omega_n}{\sqrt{1-\zeta_a^2}} e^{-\zeta_a \omega_n (t-t_{04})} \sin\left(\omega_n \sqrt{1-\zeta_a^2} (t-t_{04})\right). \quad (J.24)$$



Using the results derived in Appendix E, the actual system response to the four impulse input for  $t \geq t_{0a}$  can be expressed as

$$x_{4a}(t) = B_{4a} \sin(\alpha t + \psi_{4a}) \quad (\text{J.25})$$

where

$$B_{4a} = \frac{1}{\sqrt{1 - \zeta_a^2}} \frac{\omega_n}{1 + 3M + 3M^2 + M^3} e^{-\zeta_a \omega_n t} \sqrt{(\text{den}_{4a})^2 + (\text{num}_{4a})^2} \quad (\text{J.26})$$

$$\psi_{4a} = -\tan^{-1} \left( \frac{\text{num}_{4a}}{\text{den}_{4a}} \right) \quad (\text{J.27})$$

with

$$\begin{aligned} \text{num}_{4a} = & 3M^{\left(1 - \frac{\zeta_a}{\zeta}\right)} \sin \left( \pi \sqrt{\frac{1 - \zeta_a^2}{1 - \zeta^2}} \right) + 3M^{2\left(1 - \frac{\zeta_a}{\zeta}\right)} \sin \left( 2\pi \sqrt{\frac{1 - \zeta_a^2}{1 - \zeta^2}} \right) \\ & + M^{3\left(1 - \frac{\zeta_a}{\zeta}\right)} \sin \left( 3\pi \sqrt{\frac{1 - \zeta_a^2}{1 - \zeta^2}} \right) \end{aligned} \quad (\text{J.28})$$

$$\begin{aligned}
 den_{4a} = 1 + 3M^{\left(1-\frac{\zeta_a}{\zeta}\right)} \cos\left(\pi \sqrt{\frac{1-\zeta_a^2}{1-\zeta^2}}\right) + 3M^{2\left(1-\frac{\zeta_a}{\zeta}\right)} \cos\left(2\pi \sqrt{\frac{1-\zeta_a^2}{1-\zeta^2}}\right) \\
 + M^{3\left(1-\frac{\zeta_a}{\zeta}\right)} \cos\left(3\pi \sqrt{\frac{1-\zeta_a^2}{1-\zeta^2}}\right). \quad (J.29)
 \end{aligned}$$

Substituting Equations (J.1) and (J.25) into Equation (J.8), the vibration error for the four impulse input becomes

$$\frac{|x_{4a}(t)|}{|x_a(t)|} = \left| \frac{1}{1 + 3M + 3M^2 + M^3} \sqrt{(den_{4a})^2 + (num_{4a})^2} \right|. \quad (J.30)$$

## **APPENDIX K**

### **CIRCUIT FOR ACQUIRING FREQUENCY DATA**

The circuit shown in Figure K.1 was used to combine the control signal from the MicroVAX with a random noise signal from the HP Analyzer. This new signal was then input to the KEPCO amplifier that drives the hydraulic valve for joint one.

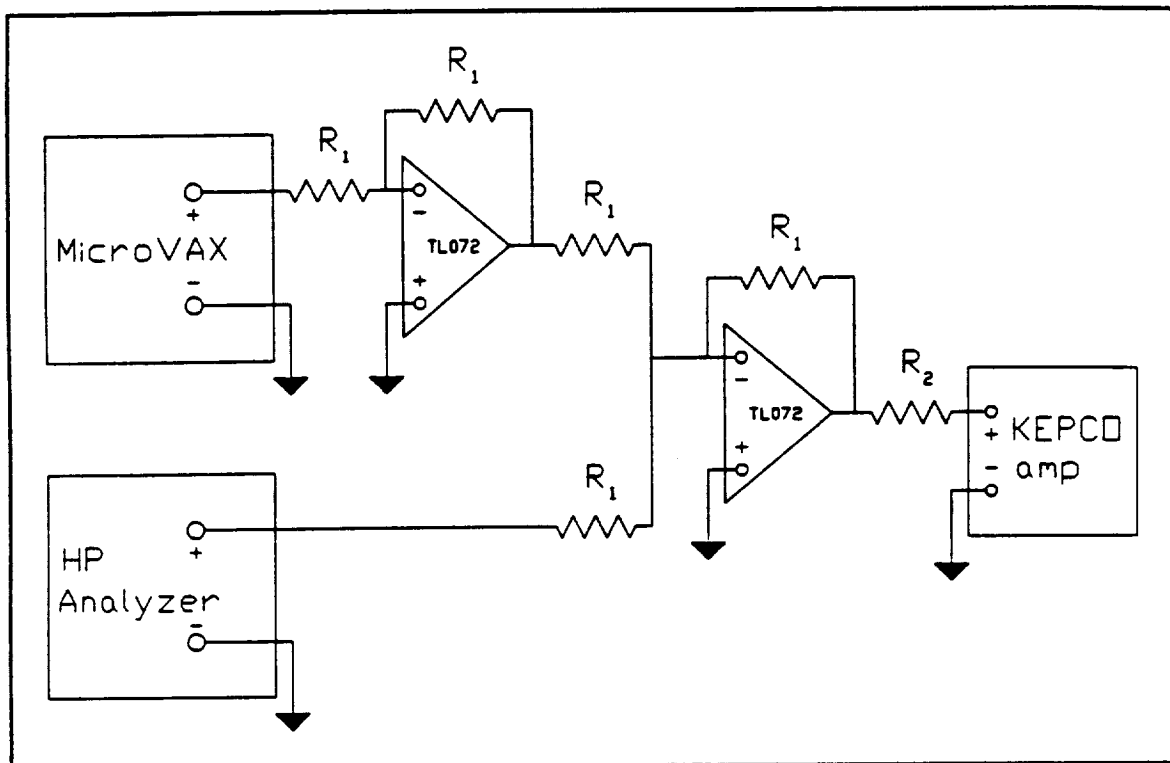


Figure K.1 Circuit Used to Combine Random Noise with Control Signal

The resistor values are chosen to insure proper impedance matching of the various system components. The resistor values used are

$$\begin{aligned} R_1 &= 10 \text{ k}\Omega \\ R_2 &= 0.1 - 10 \text{ k}\Omega. \end{aligned}$$

NOTE: The KEPCO amplifier requires its input device to have an impedance higher than the operational amplifier (op amp) can supply. Therefore,  $R_2$  must be used to increase the overall back impedance of the op amp.

## APPENDIX L

### LEAST-SQUARES REGRESSION OF EXPERIMENTAL DATA

This appendix shows how a least-squares curve fit was derived from the experimental data. A polynomial regression that is a function of  $\theta_1$  and  $\theta_2$  will be developed for the damped natural frequency,  $f_d$ , and the damping ratio,  $\zeta$ . A full discussion of linear regressions can be found in [10].

Consider the following 3<sup>rd</sup>-order polynomial

$$y = b_3\theta_2^3 + b_2\theta_2^2 + b_1\theta_2 + a_3\theta_1^3 + a_2\theta_1^2 + a_1\theta_1 + a_0. \quad (\text{L.1})$$

The sum of the squares of the residuals is

$$S_r = \sum_{i=1}^N (y_i - a_0 - a_1\theta_{1i} - a_2\theta_{1i}^2 - a_3\theta_{1i}^3 - b_1\theta_{2i} - b_2\theta_{2i}^2 - b_3\theta_{2i}^3)^2 \quad (\text{L.2})$$

where  $N$  is the number of data points. Take the derivative of Equation (L.2) with respect to each of the unknown coefficients of the polynomial to get

$$\frac{\partial S_r}{\partial a_0} = -2 \sum_{i=1}^N (y_i - a_0 - a_1\theta_{1i} - a_2\theta_{1i}^2 - a_3\theta_{1i}^3 - b_1\theta_{2i} - b_2\theta_{2i}^2 - b_3\theta_{2i}^3) \quad (\text{L.3})$$

$$\frac{\partial S_r}{\partial a_1} = -2 \sum_{i=1}^N \theta_{1i} (y_i - a_0 - a_1 \theta_{1i} - a_2 \theta_{1i}^2 - a_3 \theta_{1i}^3 - b_1 \theta_{2i} - b_2 \theta_{2i}^2 - b_3 \theta_{2i}^3) \quad (\text{L.4})$$

$$\frac{\partial S_r}{\partial a_2} = -2 \sum_{i=1}^N \theta_{1i}^2 (y_i - a_0 - a_1 \theta_{1i} - a_2 \theta_{1i}^2 - a_3 \theta_{1i}^3 - b_1 \theta_{2i} - b_2 \theta_{2i}^2 - b_3 \theta_{2i}^3) \quad (\text{L.5})$$

$$\frac{\partial S_r}{\partial a_3} = -2 \sum_{i=1}^N \theta_{1i}^3 (y_i - a_0 - a_1 \theta_{1i} - a_2 \theta_{1i}^2 - a_3 \theta_{1i}^3 - b_1 \theta_{2i} - b_2 \theta_{2i}^2 - b_3 \theta_{2i}^3) \quad (\text{L.6})$$

$$\frac{\partial S_r}{\partial b_1} = -2 \sum_{i=1}^N \theta_{2i} (y_i - a_0 - a_1 \theta_{1i} - a_2 \theta_{1i}^2 - a_3 \theta_{1i}^3 - b_1 \theta_{2i} - b_2 \theta_{2i}^2 - b_3 \theta_{2i}^3) \quad (\text{L.7})$$

$$\frac{\partial S_r}{\partial b_2} = -2 \sum_{i=1}^N \theta_{2i}^2 (y_i - a_0 - a_1 \theta_{1i} - a_2 \theta_{1i}^2 - a_3 \theta_{1i}^3 - b_1 \theta_{2i} - b_2 \theta_{2i}^2 - b_3 \theta_{2i}^3) \quad (\text{L.8})$$

$$\frac{\partial S_r}{\partial b_3} = -2 \sum_{i=1}^N \theta_{2i}^3 (y_i - a_0 - a_1 \theta_{1i} - a_2 \theta_{1i}^2 - a_3 \theta_{1i}^3 - b_1 \theta_{2i} - b_2 \theta_{2i}^2 - b_3 \theta_{2i}^3). \quad (\text{L.9})$$

Equations (L.3) through (L.9) can be set equal to zero to minimize  $S_r$ . Rearranging the previously mentioned equations yields a linear equation with respect to the unknown coefficients of the form

$$[A]\bar{x} = \bar{z} \quad (L.10)$$

where

$$[A] = \begin{bmatrix} N & \sum_{i=1}^N \theta_{1i} & \sum_{i=1}^N \theta_{1i}^2 & \sum_{i=1}^N \theta_{1i}^3 & \sum_{i=1}^N \theta_{2i} & \sum_{i=1}^N \theta_{2i}^2 & \sum_{i=1}^N \theta_{2i}^3 \\ \sum_{i=1}^N \theta_{1i} & \sum_{i=1}^N \theta_{1i}^2 & \sum_{i=1}^N \theta_{1i}^3 & \sum_{i=1}^N \theta_{1i}^4 & \sum_{i=1}^N \theta_{1i}\theta_{2i} & \sum_{i=1}^N \theta_{1i}\theta_{2i}^2 & \sum_{i=1}^N \theta_{1i}\theta_{2i}^3 \\ \sum_{i=1}^N \theta_{1i}^2 & \sum_{i=1}^N \theta_{1i}^3 & \sum_{i=1}^N \theta_{1i}^4 & \sum_{i=1}^N \theta_{1i}^5 & \sum_{i=1}^N \theta_{1i}^2\theta_{2i} & \sum_{i=1}^N \theta_{1i}^2\theta_{2i}^2 & \sum_{i=1}^N \theta_{1i}^2\theta_{2i}^3 \\ \sum_{i=1}^N \theta_{1i}^3 & \sum_{i=1}^N \theta_{1i}^4 & \sum_{i=1}^N \theta_{1i}^5 & \sum_{i=1}^N \theta_{1i}^6 & \sum_{i=1}^N \theta_{1i}^3\theta_{2i} & \sum_{i=1}^N \theta_{1i}^3\theta_{2i}^2 & \sum_{i=1}^N \theta_{1i}^3\theta_{2i}^3 \\ \sum_{i=1}^N \theta_{2i} & \sum_{i=1}^N \theta_{2i}\theta_{1i} & \sum_{i=1}^N \theta_{2i}\theta_{1i}^2 & \sum_{i=1}^N \theta_{2i}\theta_{1i}^3 & \sum_{i=1}^N \theta_{2i}^2 & \sum_{i=1}^N \theta_{2i}^3 & \sum_{i=1}^N \theta_{2i}^4 \\ \sum_{i=1}^N \theta_{2i}^2 & \sum_{i=1}^N \theta_{2i}^2\theta_{1i} & \sum_{i=1}^N \theta_{2i}^2\theta_{1i}^2 & \sum_{i=1}^N \theta_{2i}^2\theta_{1i}^3 & \sum_{i=1}^N \theta_{2i}^3 & \sum_{i=1}^N \theta_{2i}^4 & \sum_{i=1}^N \theta_{2i}^5 \\ \sum_{i=1}^N \theta_{2i}^3 & \sum_{i=1}^N \theta_{2i}^3\theta_{1i} & \sum_{i=1}^N \theta_{2i}^3\theta_{1i}^2 & \sum_{i=1}^N \theta_{2i}^3\theta_{1i}^3 & \sum_{i=1}^N \theta_{2i}^4 & \sum_{i=1}^N \theta_{2i}^5 & \sum_{i=1}^N \theta_{2i}^6 \end{bmatrix} \quad (L.11)$$

$$\vec{x} = \begin{bmatrix} a_0 \\ a_1 \\ a_2 \\ a_3 \\ b_1 \\ b_2 \\ b_3 \end{bmatrix} \quad (\text{L.12})$$

and

$$\vec{z} = \begin{bmatrix} \sum_{i=1}^N y_i \\ \sum_{i=1}^N \theta_{1i} y_i \\ \sum_{i=1}^N \theta_{1i}^2 y_i \\ \sum_{i=1}^N \theta_{1i}^3 y_i \\ \sum_{i=1}^N \theta_{2i} y_i \\ \sum_{i=1}^N \theta_{2i}^2 y_i \\ \sum_{i=1}^N \theta_{2i}^3 y_i \end{bmatrix} . \quad (\text{L.13})$$



The unknown coefficients can now be easily solved for by

$$\vec{x} = [A]^{-1} \vec{z}. \quad (L.14)$$

A MATLAB program was used to evaluate Equation (L.14) using the experimental data from Chapter IV. The resulting equations for the damped natural frequency and damping ratio are

$$\begin{aligned} f_d(\theta_1, \theta_2) = & -0.4212\theta_2^3 + 1.8086\theta_2^2 - 2.1441\theta_2 - 0.2229\theta_1^3 \\ & + 1.4540\theta_1^2 - 3.6392\theta_1 + 7.7830 \end{aligned} \quad (L.15)$$

and

$$\begin{aligned} \zeta(\theta_1, \theta_2) = & -0.4269\theta_2^3 + 1.8918\theta_2^2 - 2.7159\theta_2 - 0.0533\theta_1^3 \\ & + 0.3410\theta_1^2 - 0.6148\theta_1 + 1.6762. \end{aligned} \quad (L.16)$$

## BIBLIOGRAPHY

- [1] Alberts, T.E., Book, W.J. and Dickerson, S.L., "Experiments in Augmenting Active Control of a Flexible Structure with Passive Damping," AIAA Paper 86-0176, AIAA 24th Aerospace Sciences Meeting, Reno, NV, 1986.
- [2] Alberts, T.E., Hastings, G.G., Book, W.J. and Dickerson, S.L., "Experiments in Optimal Control of a Flexible Arm with Passive Damping," *Fifth VPI&SU/ALAA Symposium on Dynamics and Control of Large Structures*, Blacksburg, VA, 1985.
- [3] Application Note 243, *The Fundamentals of Signal Analysis*, Hewlett-Packard Company, Palo Alto, CA.
- [4] Application Note 243-1, *Dynamic Signal Analyzer Applications*, Hewlett-Packard Company, Palo Alto, CA.
- [5] Application Note 243-3, *The Fundamentals of Modal Analysis*, Hewlett-Packard Company, Palo Alto, CA.
- [6] Book, W.J., *Modeling, Design and Control of Flexible Manipulator Arms*, Ph.D. Thesis, Massachusetts Institute of Technology, April, 1974.
- [7] Book, W.J., "Recursive Lagrangian Dynamics of Flexible Manipulators," *The International Journal of Robotics Research*, 1984, pp.87-106.
- [8] Book, W.J., "Modeling, Design, and Control of Flexible Manipulator Arms: Status and Trends," NASA Conference on Space Telerobotics, Pasadena, CA, 1989, p.97.
- [9] Brooks, T.L., "Teleoperator System Response for Nuclear Telepresence," *Proceedings of the Fourth ANS Topical Meeting on Robotics and Remote Systems*, 1991, pp.547-556.
- [10] Chapra, S.C. and Canale, R.P., *Numerical Methods for Engineers*, McGraw-Hill, 1988.
- [11] Craig, J.J., *Introduction to Robotics*, Addison-Wesley Publishing Co., 1989.

- [12] Fiala, J.C., "Interfaces to Teleoperation Devices," *National Institute of Standards and Technology Technical Note 1254*, October, 1988.
- [13] Fischer, P., Daniel, R. and Siva, K.V., "Specification and Design of Input Devices for Teleoperation," *Proceedings of the 1990 IEEE International Conference on Robotics and Automation*, Cincinnati, OH, pp.540-545.
- [14] Ginsberg, J.H., *Advanced Engineering Dynamics*, Harper & Row, 1988.
- [15] Hannema, D.P. and Book, W.J., "Master-Slave Manipulator Performance for Various Dynamic Characteristics and Positioning Task Parameters," *IEEE Transactions on Systems, Man and Cybernetics*, November, 1980, pp.767-771.
- [16] Haroldsdottir, A., Kabamba, P.T. and Ulsoy, A.G., "Control of Linear Systems by Output Proportional Plus Derivative Feedback," *Journal of Dynamic Systems, Measurement and Control*, March, 1990, pp.27-35.
- [17] Hastings, G.G. and Book, W.J., "Experiments in the Optimal Control of a Flexible Manipulator," *Proceedings of the 1988 American Control Conference*, Boston, MA, pp.728-729.
- [18] Hillsley, K.L. and Yurkovich, S., "Vibration Control of a Two-Link Flexible Robot Arm," *Proceedings of the 1991 International Conference on Robotics and Automation*, Sacramento, CA, pp.2121-2126.
- [19] Huggins, J.D., *Experimental Verification of a Model of a Two-Link Flexible, Lightweight Manipulator*, Master's Thesis, Georgia Institute of Technology, June, 1988.
- [20] Huggins, J.D., Kwon, D.S., Lee, J.W. and Book, W.J., "Alternative Modeling and Verification Techniques for a Large Flexible Arm," *Proceedings of the Conference on Applied Motion Control*, Minneapolis, MN, 1987, pp.157-164.
- [21] Hyde, J.M. and Seering, W.P., "Using Input Command Pre-Shaping to Suppress Multiple Mode Vibration," *Proceedings of the 1991 IEEE International Conference on Robotics and Automation*, Sacramento, CA, pp.2604-2609.
- [22] Jansen, J.F., Burks, B.L., Bablock, S.M., Kress, R.L. and Hamel, W.R., "Long-Reach Manipulation for Waste Storage Tank Remediation," to appear in 1991 ASME Winter Annual Meeting, Atlanta, GA.

- [23] Knappe, B.P. and Berger, A., "Development of a Remote Tank Inspection (RTI) Robotic System," *Proceedings of the Fourth ANS Topical Meeting on Robotics and Remote Systems*, 1991, pp.471-481.
- [24] Kwon, D.S., *An Inverse Dynamic Tracking Control for Bracing a Flexible Manipulator*, Ph.D. Thesis, Georgia Institute of Technology, June, 1991.
- [25] Kwon, D.S. and Book, W.J., "An Inverse Dynamic Method Yielding Flexible Manipulator State Trajectories," *Proceedings of the 1990 American Control Conference*, San Diego, CA, pp.186-193.
- [26] Lee, J.W., *Dynamic Analysis and Control of Lightweight Manipulators with Flexible Parallel Link Mechanisms*, Ph.D. Thesis, Georgia Institute of Technology, June, 1990.
- [27] Lee, J.W., Huggins, J.D. and Book, W.J., "Experimental Verification of a Large Flexible Manipulator," *Proceedings of the 1988 American Control Conference*, Atlanta, GA, pp.1021-1028.
- [28] Lee, S.H. and Book, W.J., "Use of End-Effector Inertial Forces for Damping the Vibration of a Large Arm," *Proceedings of the 1989 American Control Conference*, Philadelphia, PA, pp.1377-1380.
- [29] Lee, S.H. and Book, W.J., "Robot Vibration Control Using Inertial Damping Forces," *VIII CISM-IFTOMM Symposium on the Theory and Practice of Robots and Manipulators*, Cracow, Poland, 1990.
- [30] Mabie, H.H. and Reinholtz, C.F., *Mechanisms and Dynamics of Machinery*, John Wiley & Sons, 1987.
- [31] Meirovitch, L., *Elements of Vibration Analysis*, McGraw-Hill, 1986.
- [32] Meirovitch, L., *Dynamics and Control of Structures*, John Wiley & Sons, 1990.
- [33] Montgomery, R.C., Ghosh, D. and Kenny, S., "Analytic and Simulation Studies on the Use of Torque-Wheel Actuators for the Control of Flexible Robotic Arms," to appear in the 1991 ASME Winter Annual Meeting, Atlanta, GA.
- [34] Niemeyer, G. and Slotine, J.J.E., "Stable Adaptive Teleoperation," *Proceedings of the 1990 American Control Conference*, San Diego, CA, pp.1186-1191.

- [35] Noakes, M.W. and Jansen, J.F., "Shaping Inputs to Reduce Vibration for Suspended Payloads," *Proceedings of the Fourth ANS Topical Meeting on Robotics and Remote Systems*, 1991, pp.141-150.
- [36] Ramsey, K.A., "Effective Measurements for Structural Dynamics Testing, Part I," *Sound and Vibration*, November, 1975, pp.24-35.
- [37] Ramsey, K.A., "Effective Measurements for Structural Dynamics Testing, Part II," *Sound and Vibration*, April, 1976, pp.18-30.
- [38] Singer, N.C., *Residual Vibration Reduction in Computer Controlled Machines*, Ph.D. Thesis, Massachusetts Institute of Technology, February, 1989.
- [39] Singer, N.C. and Seering, W.P., "Preshaping Command Inputs to Reduce System Vibration," AIM No. 1027, The Artificial Intelligence Laboratory, Massachusetts Institute of Technology, January, 1988.
- [40] Singer, N.C. and Seering, W.P., "Using Acausal Shaping Techniques to Reduce Robot Vibration," *Proceedings of the 1988 IEEE International Conference on Robotics and Automation*, Philadelphia, PA, pp.1434-1439.
- [41] Singer, N.C. and Seering, W.P., "Design and Comparison of Command Shaping Methods for Controlling Residual Vibration," *Proceedings of the 1989 IEEE International Conference on Robotics and Automation*, Scottsdale, AZ, pp.888-893.
- [42] Singer, N.C. and Seering, W.P., "Experimental Verification of Command Shaping Methods for Controlling Residual Vibration in Flexible Robots," *Proceedings of the 1990 American Control Conference*, San Diego, CA, pp.1738-1744.
- [43] Singhose, W.E., Seering, W.P. and Singer, N.C., "Shaping Inputs to Reduce Vibration: A Vector Diagram Approach," *Proceedings of the 1990 IEEE International Conference on Robotics and Automation*, Cincinnati, OH, pp.922-927.
- [44] Spong, M.W. and Vidyasagar, M., *Robot Dynamics and Control*, John Wiley & Sons, 1989.
- [45] Tewani, S.G., Walcott, B.L. and Rouch, K.E., "Active Optimal Vibration Control using Dynamic Absorber," *Proceedings of the 1991 International Conference on Robotics and Automation*, Sacramento, CA, pp.1182-1187.

- [46] Uebel, M., Ali, M.S. and Minis, I., "The Effect of Bandwidth on Telerobot System Performance," *NASA Technical Paper 3152*, 1991.
- [47] Wilson, T.R., *The Design and Construction of a Flexible Manipulator*, Master's Thesis, Georgia Institute of Technology, March, 1986.
- [48] Yemington, C., "Telerobotic Restoration of Explosives Waste Site," *Proceedings of the Fourth ANS Topical Meeting on Robotics and Remote Systems*, 1991, pp.451-460.
- [49] Yuan, B.S., *Adaptive Strategies for Controls of Flexible Arms*, Ph.D. Thesis, Georgia Institute of Technology, April, 1989.
- [50] Yuan, B.S. and Book, W.J., "Robust Schemes for Direct Adaptive Control of Flexible Arms," *Proceedings of the 1987 ASME Winter Annual Meeting*, Boston, MA, pp.261-268.



